NUMERICAL DETERMINATION OF THE LOCATION OF CRITICAL INCLINATIONS FOR LONG TERM HIGH ECCENTRICITY ORBITS ABOUT MARS

THESIS

Denis F. Durand
Captain, USAF

AFIT/GA/ENY/89J-2

DEPARTMENT OF THE AIR FORCE
AIR UNIVERSITY
AIR FORCE INSTITUTE OF TECHNOLOGY
Wright-Patterson Air Force Base, Ohio

AFIT/GA/ENY/89J-2

NUMERICAL DETERMINATION OF THE LOCATION OF CRITICAL INCLINATIONS FOR LONG TERM HIGH ECCENTRICITY ORBITS ABOUT MARS

THESIS

Denis F. Durand
Captain, USAF

AFIT/GA/ENY/89J-2

AFIT/GA/ENY/89J-2

NUMERICAL DETERMINATION OF THE LOCATION OF CRITICAL INCLINATIONS FOR LONG TERM HIGH ECCENTRICITY ORBITS ABOUT MARS

THESIS

Presented to the Faculty of the School of Engineering

of the Air Force Institute of Technology

Air University

In Partial Fulfillment of the

Requirements for the Degree of

Master of Science in Astronautical Engineering

Denis F. Durand, B.S.

Captain, USAF

June, 1989

Approved for public release; distribution unlimited

Acknowledgments

I would like to thank my advisor, Capt Rodney Bain, for all of his help and encouragement, and my wife and son, Margaret and Devon, for their patience and understanding.

Denis F. Durand

Table of Contents

List of Figures

List of Tables

List of Symbols

Abstract

The purpose of this study is to locate critical inclinations in long term high eccentricity orbits about Mars using numerical methods. A critical inclination is defined as the inclination at orbit insertion which produces a local maximum in the amplitude of the variation of eccentricity or inclination. The perturbation model consists of the first non-zero zonal harmonic (J_2) of the Mars gravity potential and the Sun as a point mass third body. The search range consists of inclinations from 0.25 to 90.0 degrees, eccentricities from 0.40 to 0.90, periapse radii from 4000 km to 7000 km, and orbit lifetimes of 10 Earth years.

The numerical search comprises the following procedure: (1) A time history of eccentricity and inclination is produced for each combination of orbit insertion initial conditions by numerically propagating Lagrange's Planetary Equations. (2) Each time history is fit, in the least squares sense, to a linear function. The standard deviation of the residuals for each fit is employed as the search parameter. (3) A three-dimensional surface plot of the standard deviation in eccentricity and the standard deviation in inclination versus eccentricity and inclination is produced for each value of periapse radius considered. The local maximums in these surfaces identifies the locations of the critical inclinations. (4) The three-dimensional surfaces are then reduced to two dimensions by plotting inclination versus eccentricity for the local maximums in standard deviation.

Six critical inclination curves for eccentricity are identified, three of which are curve fit and found to be linear in periapse radius and quadratic in eccentricity. The surface plots for inclination indicate the presence of large variations but the surface topography does not allow for the identification of distinct local maximum curves.

NUMERICAL DETERMINATION OF THE LOCATION OF CRITICAL INCLINATIONS FOR LONG TERM HIGH ECCENTRICITY ORBITS ABOUT MARS

I. Introduction

The task of placing satellites in long-term orbit about Mars will require extensive planning, but one of the first mission parameters to consider will be the orbit itself. Orbit design will be a function not only of the specific mission requirements, but also of mission costs, and in particular, the costs related to orbit insertion. Inserting a satellite into orbit about Mars requires a large velocity change between the Earth-to-Mars transfer trajectory and a closed orbit about Mars. The magnitude of the velocity change, and therefore the related costs, is inversely proportional to the energy of the Mars-centered orbit.

Consider a satellite mission which includes the need to make close observations of the Martian surface. This requirement may be met by simply inserting the satellite into a near circular orbit just above the atmosphere, but such an orbit possesses at least two disadvantages: 1) atmospheric drag, and 2) the fuel required to insert the satellite into such a low-energy orbit.

An approach to the solution of these problems is to utilize a high eccentricity orbit, which allows for close approach (at periapse) as well as reduced insertion fuel requirements (compared to the circular or near circular orbit). High eccentricity orbits, however, are not without difficulties. The combined effects of the gravity fields of Mars and of the Sun will produce resonance, causing large variations in the orbital elements. Such variations may result in violated mission constraints, and in severe cases, reentry and impact.

To illustrate this phenomenon, Figures 1 and 2 display the behavior of the eccentricity and inclination of a Martian orbit over a period of twenty Earth years (under the conditions for which large variations are not present). Figures 3 and 4 present the behavior of these parameters under the conditions for which large variations do exist.

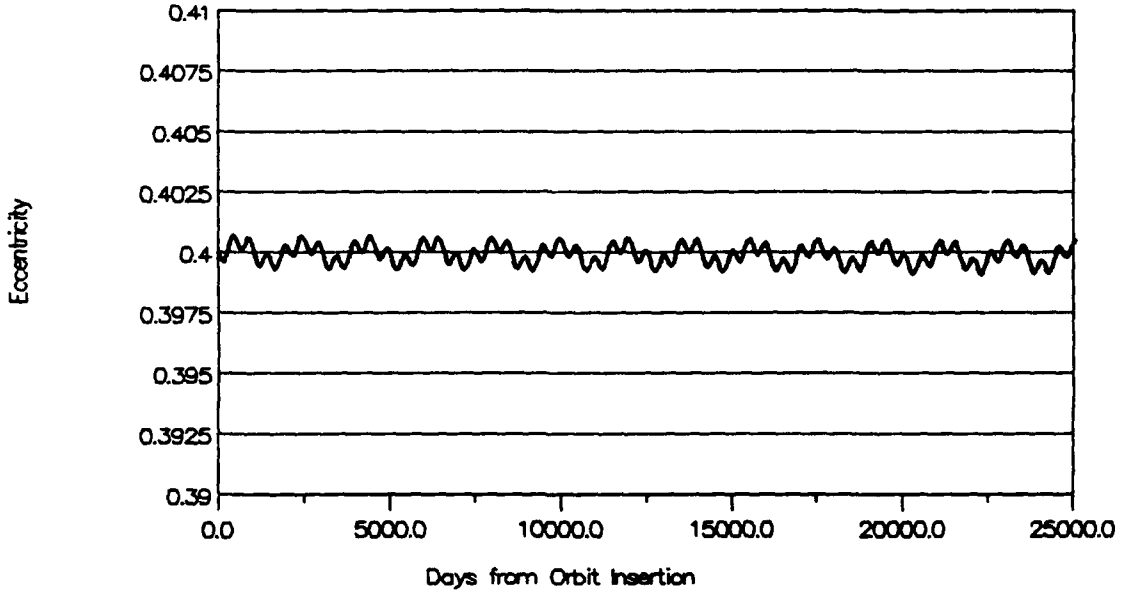

Figure 1. Example of Small Amplitude Variation in Eccentricity for a Long-term Martian Orbit

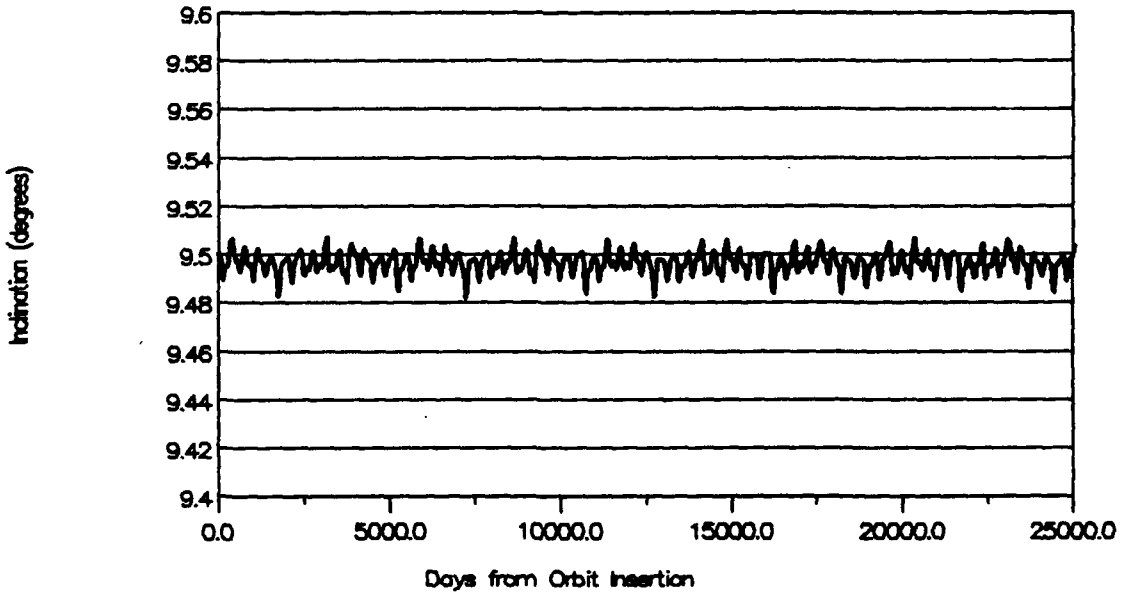

Figure 2. Example of Small Amplitude Variation in Inclination for a Long-term Martian Orbit

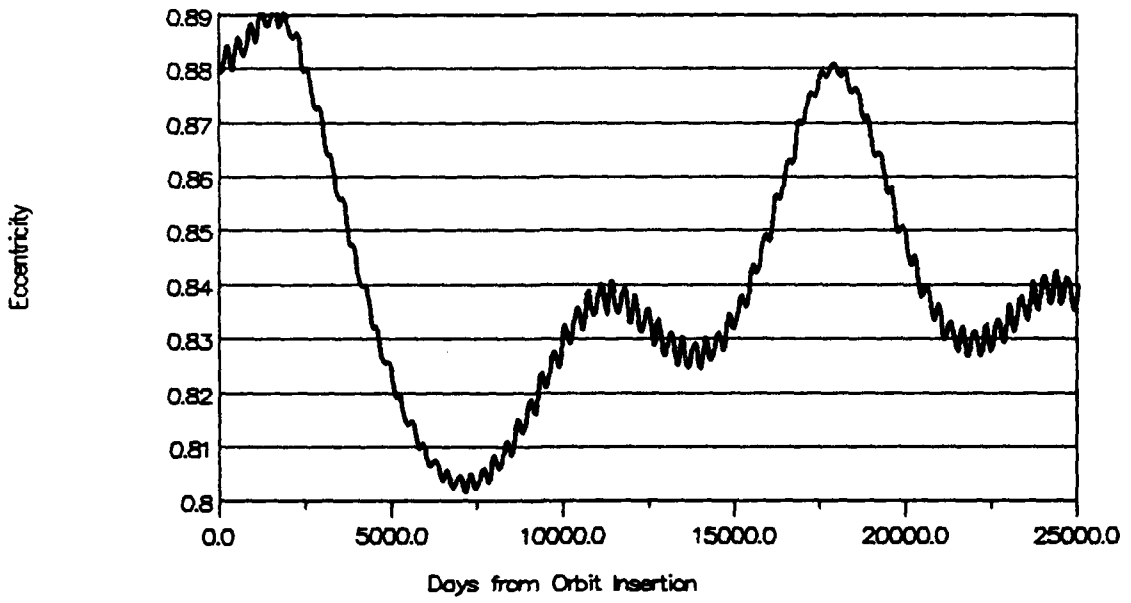

Figure 3. Example of Large Amplitude Variation in Eccentricity for a Long-term Martian Orbit

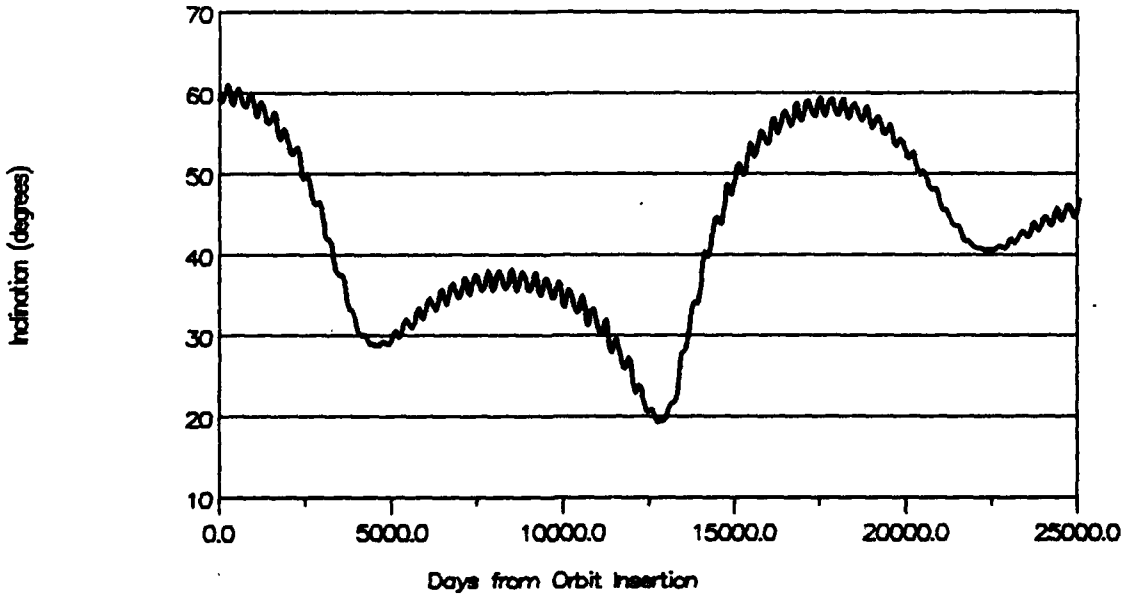

Figure 4. Example of Large Amplitude Variation in Inclination for a Long-term Martian Orbit

The conditions for which such large variations occur are primarily a function of the values of the eccentricity and inclination at orbit insertion. These two elements determine the exposure of the orbit to the effects of the planet oblateness and to the third-body effects of the Sun. The dependence of these variations on eccentricity will be shown to be generally a direct one, that is, the larger the eccentricity, the greater the variations. However, the effects of the orbit inclination are not as clear, and are therefore of greater concern.

This thesis develops a numerical method for determining the values of inclination and eccentricity for which large variations in these two elements occur. The gravity models will be simplified, considering only the first non-zero zonal harmonic (J_2) of the Mars gravity potential, and treating the Sun as a point mass. The reasons for this are twofold: 1) to meet with the constraint of limited computer time, and 2), to provide a basis for comparison with an analytical approach in locating the critical inclinations. This model therefore includes only the dominant sources of perturbation (for Mars, J_2 is larger than any other zonal harmonic by two orders of magnitude, and is twice the magnitude of J_2 for Earth).

This investigation begins by presenting the theory upon which the numerical work is based, including the derivation of the disturbing functions used in Lagrange's Planetary Equations (LPEs) for propagating the time history of the orbital elements, as well as providing a brief summary of an analytical approach to locating the critical inclinations. The numerical work is presented by describing the computer program which was utilized, followed by a description of the approach in locating the critical inclinations. The results are given primarily in graphical form.

II. *Analytical Development*

Equation of Motion

Figure 5 shows the reference frame used throughout this investigation. The Sun, relative to this reference frame, is considered to "orbit" Mars.

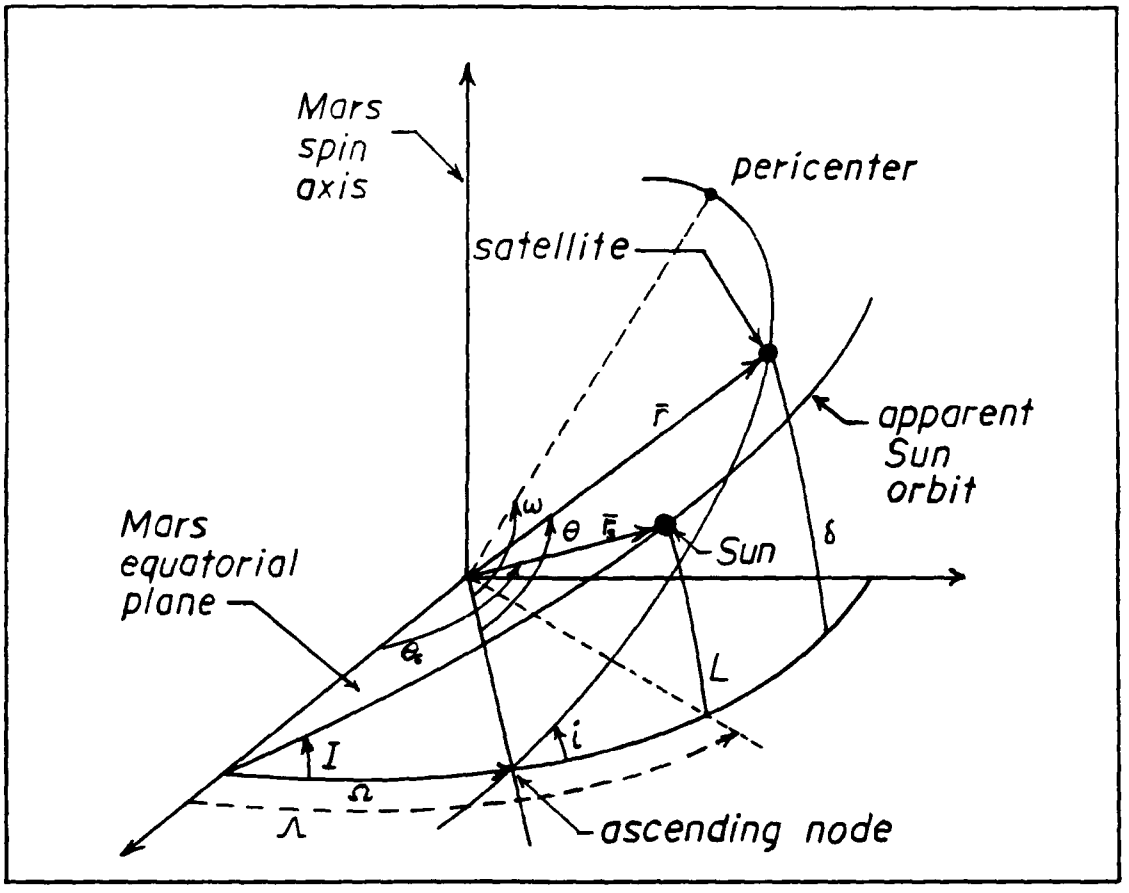

Figure 5. Mars-centered Reference Frame

Symbols used in this figure are defined as follows:

$\bar{r}$ = satellite radius vector

$\bar{r}_s$ = Sun radius vector

i = inclination of satellite orbit

Ω = argument of ascending node for satellite orbit

ω = argument of periapse for satellite orbit

I = inclination of Sun orbit

Λ = right ascension of the Sun

L = Mars-centered latitude of the Sun

θ = satellite central angle

θ_s = Sun central angle

The equations of motion for the satellite in this reference frame may be written as the gradient of the gravity potentials of Mars and of the Sun:

$$\ddot{\vec{r}} = \nabla(R_M + R_S) \tag{1}$$

where

∇ = gradient operator

R_M = Mars gravity potential

R_S = Sun gravity potential

The orbital elements (other than the mean anomaly) remain constant when the central body is modeled as a point mass and no other forces are included. The effects of the Sun and of the oblateness of Mars introduce perturbations which cause the orbital elements to vary with time. The perturbing contribution to the gravity potentials are modeled as a disturbing function R , which, when introduced into the LPEs [4:476-483], describes the 'motion' of the orbital elements.

The LPEs may be written as follows:

$$\frac{d\Omega}{dt} = \frac{1}{nab\sin i}\frac{\partial R}{\partial i} \tag{2}$$

$$\frac{di}{dt} = -\frac{1}{nab\sin i}\frac{\partial R}{\partial \Omega} + \frac{\cos i}{nab\sin i}\frac{\partial R}{\partial \omega} \tag{3}$$

$$\frac{d\omega}{dt} = -\frac{\cos i}{nab\sin i}\frac{\partial R}{\partial i} + \frac{b}{na^3 e}\frac{\partial R}{\partial e} \tag{4}$$

$$\frac{da}{dt} = \frac{2}{na}\frac{\partial R}{\partial M} \tag{5}$$

$$\frac{de}{dt} = \frac{b^2}{na^4 e}\frac{\partial R}{\partial M} - \frac{b}{na^3 e}\frac{\partial R}{\partial \omega} \tag{6}$$

$$\frac{dM}{dt} = n - \frac{2}{na}\frac{\partial R}{\partial a} - \frac{b^2}{na^4 e}\frac{\partial R}{\partial e} \tag{7}$$

where

e = eccentricity of satellite orbit

a = semi-major axis of satellite orbit

$b = a\sqrt{1-e^2}$ = semi-minor axis of satellite orbit

μ_m = Mars gravity constant

M = satellite mean anomaly

$n = \sqrt{\mu_m/a^3}$ = satellite mean motion

The disturbing function R will now be derived.

The Mars Disturbing Function

The gravity potential of Mars may be written as a combination of the two-body, undisturbed potential and the disturbing function:

$$R_M = \frac{\mu_m}{r} + R_m \tag{8}$$

where

r = magnitude of $\bar{r}$

R_m = Mars disturbing function

The Mars disturbing function (3:421), including only the second harmonic coefficient J_2 (i.e., the first non-zero zonal harmonic), may be written as

$$R_m = \frac{\mu_m J_2 R_e^2}{2r^3}(1 - 3\sin^2\delta) \tag{9}$$

where R_e is the Mars equatorial radius, and δ is the satellite declination (see Figure 5).

The parameter δ must now be rewritten in terms of the orbital elements f and ω, where f is the satellite true anomaly. To carry out this transformation, consider Figures 6 and 7 on the following page.

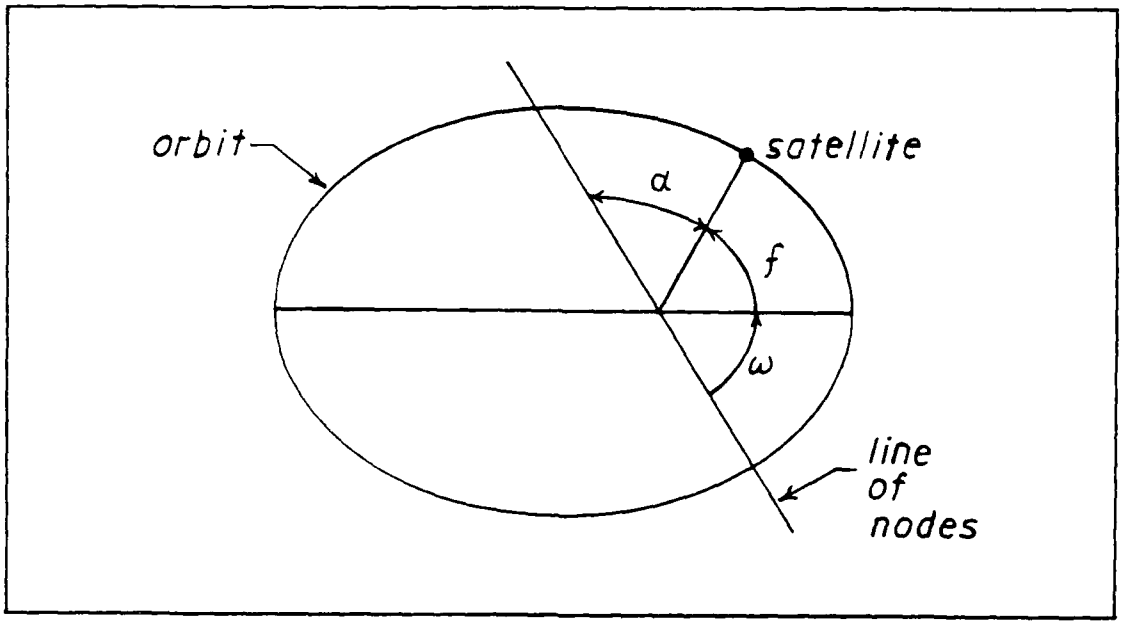

Figure 6. Looking Down the Mars Spin Axis

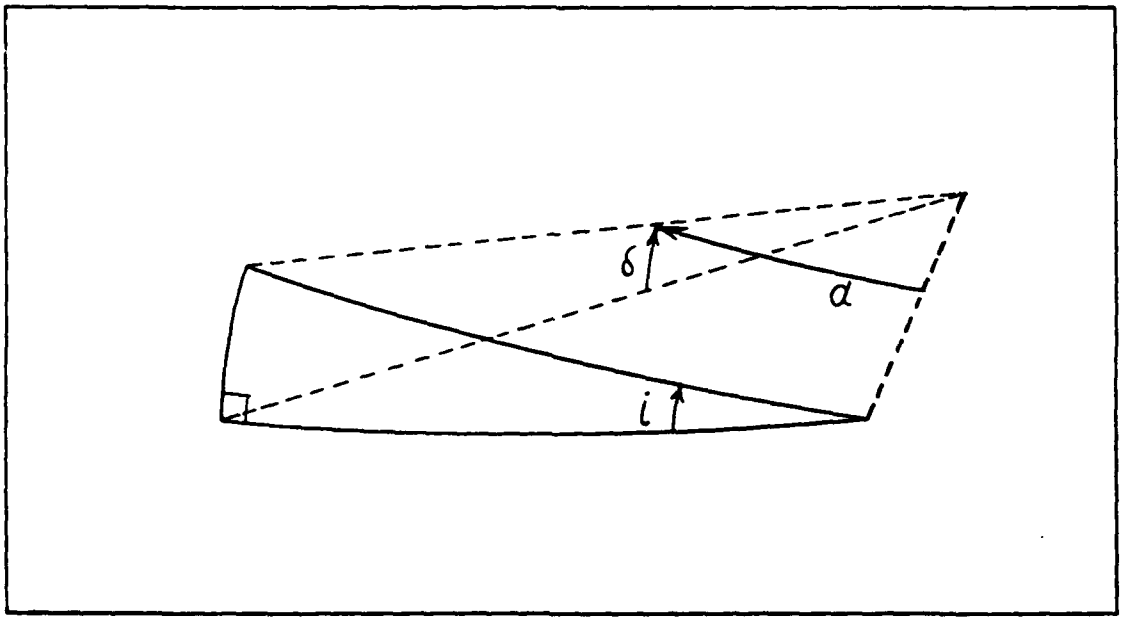

Figure 7. Relationship between δ and $f + \omega$: A Right Spherical Triangle

In Figure 6, ω is measured counterclockwise from the ascending node, f is measured counterclockwise from periapse, and α is defined such that $\alpha + f + \omega = \pi$. The central angles α and δ and the vertex angle i define a right spherical triangle, as shown in Figure 7. Making use of spherical and plane trigonometric identities gives

$$\begin{aligned} \sin\delta &= \sin i \sin\alpha \\ &= \sin i \sin(\pi - (f+\omega)) \\ &= \sin i \sin(f+\omega) \end{aligned}$$

Squaring yields

$$\begin{aligned} \sin^2\delta &= \sin^2 i \sin^2(f+\omega) \\ &= \sin^2 i \left[1 - \cos^2(f+\omega)\right] \\ &= \sin^2 i \left[1 - \left(\frac{1}{2} + \frac{1}{2}\cos 2(f+\omega)\right)\right] \\ &= \frac{1}{2}\sin^2 i \left[1 - \cos 2(f+\omega)\right] \end{aligned}$$

Substituting for $\sin^2\delta$ in equation (9) results in

$$R_m = \frac{\mu_m J_2 R_e^2}{2r^3}\left(1 - \frac{3}{2}\sin^2 i + \frac{3}{2}\sin^2 i \cos 2(f+\omega)\right) \qquad (10)$$

Averaging the Mars Disturbing Function

To determine the long-term behavior of the orbital elements, the short-term effects of the mean (or true) anomaly may be averaged out by integrating the disturbing function over 2π with respect to the mean anomaly M. The averaged Mars disturbing function $\overline{R_m}$ is acquired by

$$\overline{R_m} = \frac{1}{2\pi}\int_0^{2\pi} R_m \, dM \tag{11}$$

This integration is fascillitated by employing Hansen's Coefficients [2]. A brief description of Hansen's Coefficients along with the derivation of the Hansen's Coefficients used below are given in Appendix A. Substituting equation (10) into equation (11) yields

$$\begin{aligned}\overline{R_m} &= \frac{1}{2\pi}\int_0^{2\pi} \frac{\mu_m J_2 R_e^2}{2r^3}\left(1-\frac{3}{2}\sin^2 i\right) dM \\ &\quad + \frac{1}{2\pi}\int_0^{2\pi} \frac{3\mu_m J_2 R_e^2}{4r^3}\sin^2 i \cos 2(f+\omega)\, dM\end{aligned} \tag{12}$$

Calling the first integral A and the second B:

$$A = \frac{\mu_m J_2 R_e^2}{2a^3}\left(1-\frac{3}{2}\sin^2 i\right)\frac{1}{2\pi}\int_0^{2\pi}\left(\frac{r}{a}\right)^{-3} dM \tag{13}$$

From appendix A:

$$\frac{1}{2\pi}\int_0^{2\pi}\left(\frac{r}{a}\right)^{-3} dM = X_0^{-3,0} = \left(1-e^2\right)^{-3/2} \tag{14}$$

Therefore

$$A = \frac{\mu_m J_2 R_e^2}{2a^3\left(1-e^2\right)^{3/2}}\left(1-\frac{3}{2}\sin^2 i\right) \tag{15}$$

Working with the second integral:

$$B = \frac{3\mu_m J_2 R_e^2}{4a^3}\sin^2 i\left\{\frac{1}{2\pi}\int_0^{2\pi}\left(\frac{r}{a}\right)^{-3}\cos 2\left(f+\omega\right) dM\right\} \tag{16}$$

Using the appropriate trigonometric relation, the expression in curly brackets becomes

$$\begin{aligned}&\frac{1}{2\pi}\int_0^{2\pi}\left(\frac{r}{a}\right)^{-3}\left(\cos 2f\cos 2\omega - \sin 2f \sin 2\omega\right) dM \\ &= \cos 2\omega\frac{1}{2\pi}\int_0^{2\pi}\left(\frac{r}{a}\right)^{-3}\cos 2f\, dM - \sin 2\omega\frac{1}{2\pi}\int_0^{2\pi}\left(\frac{r}{a}\right)^{-3}\sin 2f\, dM\end{aligned}$$

From appendix A

$$\frac{1}{2\pi}\int_0^{2\pi}\left(\frac{r}{a}\right)^{-3}\sin 2f\,dM = 0 \tag{17}$$

and

$$\frac{1}{2\pi}\int_0^{2\pi}\left(\frac{r}{a}\right)^{-3}\cos 2f\,dM = X_0^{-3,2} = 0 \tag{18}$$

Hence, the averaged Mars disturbing function becomes

$$\overline{R_m} = \frac{\mu_m J_2 R_e^2}{2a^3\left(1-e^2\right)^{3/2}}\left(1-\frac{3}{2}\sin^2 i\right) \tag{19}$$

The Solar Disturbing Function

Since the third-body effects of the Sun are to be included by considering the Sun to be a point mass, the solar disturbing function may be derived by invoking Newton's Law of Universal Gravitation. The final expression for the solar disturbing function is to be with repect to the reference frame shown in Figure 5. To accomplish this, consider the arbitrary inertial reference frame shown in Figure 8 below.

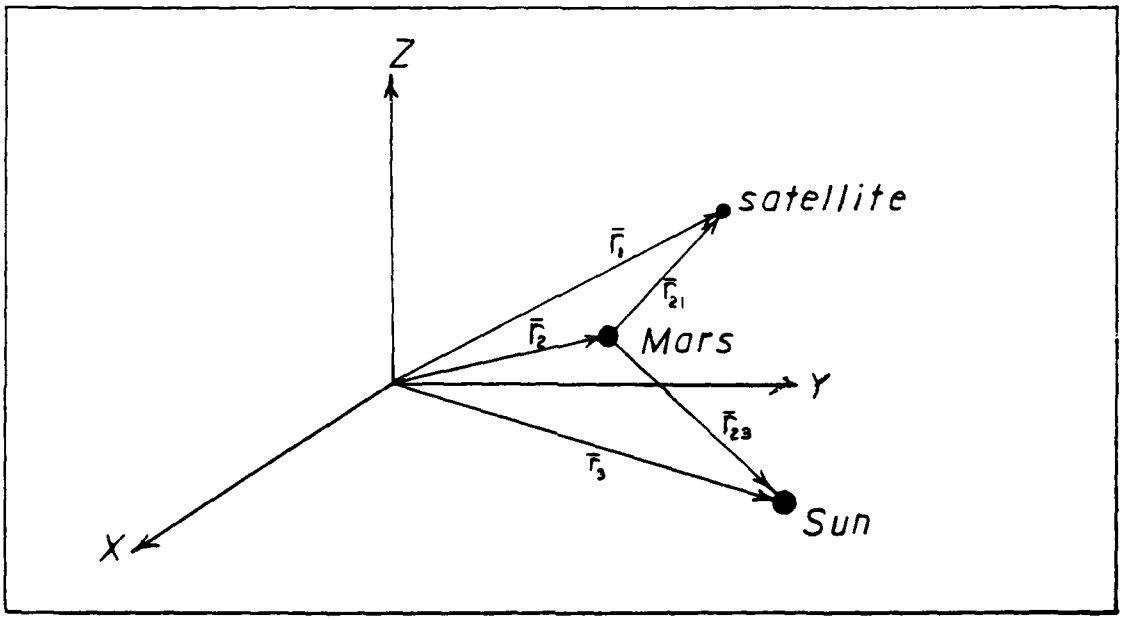

Figure 8. Inertial Reference Frame for Deriving Solar Disturbing Function

Define the following:

$\bar{r}_1$ = radius vector to satellite

$\bar{r}_2$ = radius vector to Mars

$\bar{r}_3$ = radius vector to Sun

m_1 = mass of satellite

m_2 = mass of Mars

m_3 = mass of Sun

$\bar{r}_{ij} = \bar{r}_j - \bar{r}_i$

The force on the satellite due to the combined effects of Mars and the Sun is

$$\overline{F}_1 = -Gm_1\left[\frac{m_2}{r_{21}^3}\overline{r}_{21} + \frac{m_3}{r_{31}^3}\overline{r}_{31}\right] \tag{20}$$

where G is the universal gravitational constant. The force on Mars due to the combined effects of the satellite and the Sun is

$$\overline{F}_2 = -Gm_2\left[\frac{m_1}{r_{12}^3}\overline{r}_{12} + \frac{m_3}{r_{32}^3}\overline{r}_{32}\right] \tag{21}$$

The accelerations of the satellite and of Mars are

$$\ddot{\overline{r}}_1 = \frac{\overline{F}_1}{m_1} = -G\left[\frac{m_2}{r_{21}^3}\overline{r}_{21} + \frac{m_3}{r_{31}^3}\overline{r}_{31}\right] \tag{22}$$

$$\ddot{\overline{r}}_2 = \frac{\overline{F}_2}{m_2} = -G\left[\frac{m_2}{r_{12}^3}\overline{r}_{12} + \frac{m_3}{r_{32}^3}\overline{r}_{32}\right] \tag{23}$$

Since $\overline{r}_{21} = \overline{r}_1 - \overline{r}_2$, the acceleration of the satellite relative to Mars is $\ddot{\overline{r}}_{21} = \ddot{\overline{r}}_1 - \ddot{\overline{r}}_2$, or

$$\begin{aligned}\ddot{\overline{r}}_{21} &= -G\left[\frac{m_2}{r_{21}^3}\overline{r}_{21} + \frac{m_3}{r_{31}^3}\overline{r}_{31}\right] + G\left[\frac{m_1}{r_{12}^3}\overline{r}_{12} + \frac{m_3}{r_{32}^3}\overline{r}_{32}\right] \\ &= -G\frac{(m_2+m_1)}{r_{21}^3}\overline{r}_{21} + Gm_3\left[\frac{\overline{r}_{32}}{r_{32}^3} - \frac{\overline{r}_{31}}{r_{31}^3}\right]\end{aligned} \tag{24}$$

Since $m_2 \gg m_1$, m_1 may be ignored. Making the substitutions $\mu_m = Gm_2$ and $\mu_s = Gm_3$ results in

$$\ddot{\overline{r}}_{21} = -\frac{\mu_m}{r_{21}^3}\overline{r}_{21} - \mu_s\left[\frac{\overline{r}_{31}}{r_{31}^3} - \frac{\overline{r}_{32}}{r_{32}^3}\right] \tag{25}$$

In terms of the notation used in Figure 5

$$\overline{r}_{21} = \overline{r}$$

$$\overline{r}_{23} = -\overline{r}_{32} = \overline{r}_s$$

$$\overline{r}_{31} = \overline{r} - \overline{r}_s$$

Making these substitutions, equation (25) becomes

$$\ddot{\overline{r}} = -\frac{\mu_m}{r^3}\overline{r} - \mu_s\left[\frac{\overline{r} - \overline{r}_s}{|\overline{r} - \overline{r}_s|^3} + \frac{\overline{r}_s}{r_s^3}\right] = \nabla(R_M + R_S) \tag{26}$$

Therefore

$$\nabla R_S = \mu_s\left[\frac{\overline{r}_s - \overline{r}}{|\overline{r}_s - \overline{r}|^3} - \frac{\overline{r}_s}{r_s^3}\right] \tag{27}$$

The solar gravity potential is then (see (11))

$$R_S = \mu_s \left[\frac{1}{|\overline{r}_s - \overline{r}|} - \frac{\overline{r} \cdot \overline{r}_s}{r_s^3} \right] \tag{28}$$

The solar disturbing function R_s may now be extracted from the solar gravity potential R_S. Let $\overline{\rho} = \overline{r}_s - \overline{r}$. Therefore

$$\begin{aligned} \rho^2 &= |\overline{r}_s - \overline{r}|^2 = (\overline{r}_s - \overline{r}) \cdot (\overline{r}_s - \overline{r}) \\ &= \overline{r}_s \cdot \overline{r}_s - 2\overline{r} \cdot \overline{r}_s + \overline{r} \cdot \overline{r} \\ &= r_s^2 - 2 r r_s \cos B + r^2 \end{aligned}$$

where

$$\cos B = \frac{\overline{r} \cdot \overline{r}_s}{r r_s} \tag{29}$$

Factoring out r_s^2

$$\rho^2 = r_s^2 \left(1 + \frac{r^2}{r_s^2} - \frac{2r}{r_s} \cos B \right)$$

$$\rho = r_s \left[1 + \frac{r^2}{r_s^2} - \frac{2r}{r_s} \cos B \right]^{1/2} = |\overline{r}_s - \overline{r}| \tag{30}$$

Substituting Eqs (29) and (30) into Eq (28) yields

$$R_s = \frac{\mu_s}{r_s} \left[\left(1 + \frac{r^2}{r_s^2} - \frac{2r}{r_s} \cos B \right)^{-1/2} - \frac{r \cos B}{r_s} \right] \tag{31}$$

The first term within the brackets of Eq (31) may be expanded in a binomial series:

$$\left[1 + \left(\frac{r^2}{r_s^2} - \frac{2r}{r_s} \cos B \right) \right]^{-1/2} = \sum_{n=0}^{\infty} \binom{-\frac{1}{2}}{n} \left(\frac{r^2}{r_s^2} - \frac{2r}{r_s} \cos B \right)^n$$

$$= 1 - \frac{1}{2} \left(\frac{r^2}{r_s^2} - \frac{2r}{r_s} \cos B \right) + \frac{1}{2} \frac{3}{4} \left(\frac{r^2}{r_s^2} - \frac{2r}{r_s} \cos B \right)^2 + \cdots$$

Since $r_s \gg r$, terms of order $(r/r_s)^3$ and above may be neglected, yielding

$$\begin{aligned} &\left[1 + \left(\frac{r^2}{r_s^2} - \frac{2r}{r_s} \cos B \right) \right]^{-1/2} \\ &= 1 - \frac{1}{2} \left(\frac{r^s}{r_s^2} - \frac{2r}{r_s} \cos B \right) + \frac{3}{8} \left(\frac{4r^2}{r_s^2} \cos^2 B \right) \end{aligned} \tag{32}$$

Substituting Eq (32) into Eq (31) results in

$$\begin{aligned} R_S &= \frac{\mu_s}{r_s}\left[1 - \frac{r^2}{2r_s^2} + \frac{3r^2}{2r_s^2}\cos^2 B\right] \\ &= \frac{\mu_s}{r_s}\left[1 + \frac{r^2}{2r_s^2}\left(3\cos^2 B - 1\right)\right] \end{aligned} \tag{33}$$

Analogous to Eq (8)

$$R_S = \frac{\mu_s}{r_s} + R_s \tag{34}$$

Therefore, the solar disturbing function is

$$R_s = \frac{\mu_s r^2}{2r_s^3}\left[3\cos^2 B - 1\right] \tag{35}$$

or

$$R_s = \frac{\mu_s r^2}{2r_s^3}\left[3\left(\frac{\overline{r}\cdot\overline{r}_s}{r r_s}\right)^2 - 1\right] \tag{36}$$

The parenthetical expression in Eq (36) must now be written in terms of the elements of the satellite orbit and of the apparent Sun orbit. In order to simplify notation, the following abbreviations will be used henceforth for all trigonometric functions:

$$\sin\theta \equiv S_\theta \quad \cos\theta \equiv C_\theta$$

Using the notation of Figure 5, define the following unit vectors:

$$\hat{e}_r = \frac{\overline{r}}{r} = \begin{bmatrix} C_\Omega C_\theta - S_\Omega C_i S_\theta \\ S_\Omega C_\theta + C_\Omega C_i S_\theta \\ S_i S_\theta \end{bmatrix} \tag{37}$$

$$\hat{e}_s = \frac{\overline{r}_s}{r_s} = \begin{bmatrix} C_\Lambda C_L \\ C_L S_\Lambda \\ S_L \end{bmatrix} \tag{38}$$

Therefore

$$\frac{\overline{r}\cdot\overline{r}_s}{r r_s} = \hat{e}_r \cdot \hat{e}_s$$

$$= C_\Omega C_\theta C_\Lambda C_L - S_\Omega C_i S_\theta C_\Lambda C_L + S_\Omega C_\theta C_L S_\Lambda + C_\Omega C_i S_\theta C_L S_\Lambda + S_i S_\theta S_L$$

$$= C_\theta C_L\left(C_\Omega C_\Lambda + S_\Omega S_\Lambda\right) + C_i S_\theta C_L\left(C_\Omega S_\Lambda - S_\Omega C_\Lambda\right) + S_i S_\theta S_L$$

$$= C_\theta C_L C_{\Omega-\Lambda} + C_i S_\theta C_L S_{\Omega-\Lambda} + S_i S_\theta S_L \tag{39}$$

The solar disturbing function now becomes

$$R_s = \frac{\mu_s r^2}{2r_s^3}\left\{3\left[C_\theta C_L C_{\Omega-\Lambda} + C_i S_\theta C_L S_{\Omega-\Lambda} + S_i S_\theta S_L\right]^2 - 1\right\} \tag{40}$$

Expanding the term in brackets yields

$$R_s = \frac{\mu_s r^2}{2r_s^3}\left\{3\left[K_1 C_\theta^2 + 2K_2 C_\theta S_\theta + K_3 S_\theta^2\right] - 1\right\} \tag{41}$$

where

$$\begin{aligned} K_1 &= (C_L C_{\Omega-\Lambda})^2 \\ K_2 &= S_L C_L S_i C_{\Omega-\Lambda} - C_L^2 C_i S_{\Omega-\Lambda} C_{\Omega-\Lambda} \\ K_3 &= (C_i C_L S_{\Omega-\Lambda} - S_L S_i)^2 \end{aligned}$$

But

$$\begin{aligned} C_\theta^2 &= \frac{1}{2} + \frac{1}{2} C_{2\theta} \\ S_\theta^2 &= \frac{1}{2} - \frac{1}{2} C_{2\theta} \\ 2S_\theta C_\theta &= S_{2\theta} \end{aligned}$$

and

$$\theta = f + \omega$$

so the solar disturbing function is finally

$$R_s = \frac{\mu_s r^2}{2r_s^3}\left\{\frac{3}{2} A_1 C_{2(f+\omega)} + 3A_2 S_{2(f+\omega)} + \frac{3}{2} A_3 - 1\right\} \tag{42}$$

where

$$\begin{aligned} A_1 &= K_1 - K_3 \\ A_2 &= K_2 \\ A_3 &= K_1 + K_3 \end{aligned}$$

Averaging the Solar Disturbing Function

As was done in the case of the Mars disturbing function, the short-term effects of the satellite true anomaly may be averaged out. The averaged solar disturbing function $\overline{R_s}$ is obtained by

$$\overline{R_s} = \frac{1}{2\pi}\int_0^{2\pi} R_s \, dM \tag{43}$$

To accomplish the averaging by employing Hansen's Coefficients (appendix A), the true anomaly f must be separated from the argument of periapse ω. Using the trigonometric relations

$$\begin{aligned} C_{2(f+\omega)} &= C_{2f}C_{2\omega} - S_{2f}S_{2\omega} \\ S_{2(f+\omega)} &= S_{2f}C_{2\omega} + C_{2f}S_{2\omega} \end{aligned}$$

Eq (42) becomes

$$\begin{aligned} R_s &= \frac{\mu_s r^2}{2r_s^3}\left\{\frac{3}{2}A_1C_{2f}C_{2\omega} - \frac{3}{2}A_1S_{2f}S_{2\omega} + 3A_2S_{2f}C_{2\omega} + 3A_2C_{2f}S_{2\omega} + \frac{3}{2}A_3 - 1\right\} \\ &= \frac{\mu_s r^2}{2r_s^3}\left\{\left(\frac{3}{2}A_1C_{2\omega} + 3A_2S_{2\omega}\right)C_{2f} + \left(3A_2C_{2\omega} - \frac{3}{2}A_1S_{2\omega}\right)S_{2f} + \frac{3}{2}A_3 - 1\right\} \end{aligned}$$

Multiplying and dividing by the square of the semi-major axis a, and then distributing r^2 results in

$$\begin{aligned} R_s = \frac{\mu_s a^2}{2r_s^3}\Bigg\{&\left(\frac{3}{2}A_1C_{2\omega} + 3A_2S_{2\omega}\right)\left(\frac{r}{a}\right)^2 C_{2f} \\ &+ \left(3A_2C_{2\omega} - \frac{3}{2}A_1S_{2\omega}\right)\left(\frac{r}{a}\right)^2 S_{2\omega} + \left(\frac{3}{2}A_3 - 1\right)\left(\frac{r}{a}\right)^2\Bigg\} \end{aligned} \tag{44}$$

Averaging the terms which are functions of the mean anomaly yields

$$\frac{1}{2\pi}\int_0^{2\pi}\left(\frac{r}{a}\right)^2 C_{2f}\, dM = X_0^{2,2} = \frac{5e^2}{2} \tag{45}$$

$$\frac{1}{2\pi}\int_0^{2\pi}\left(\frac{r}{a}\right)^2 S_{2f}\, dM = 0 \tag{46}$$

$$\frac{1}{2\pi}\int_0^{2\pi}\left(\frac{r}{a}\right)^2 dM = X_0^{2,0} = 1 + \frac{3}{2}e^2 \tag{47}$$

The averaged solar disturbing function is then

$$\begin{aligned} \overline{R_s} &= \frac{\mu_s a^2}{2r_s^3}\left\{\left(\frac{3}{2}A_1C_{2\omega} + 3A_2S_{2\omega}\right)\frac{5e^2}{2} + \left(\frac{3}{2}A_3 - 1\right)\left(1 + \frac{3}{2}e^2\right)\right\} \\ &= \frac{\mu_s a^2}{4r_s^3}\left\{\frac{15}{2}e^2A_1C_{2\omega} + 15e^2A_2S_{2\omega} + \left(2 + 3e^2\right)\left(\frac{3}{2}A_3 - 1\right)\right\} \end{aligned} \tag{48}$$

Substituting for A_1, A_2, and A_3 yields

$$\begin{aligned}\overline{R_s} &= \frac{\mu_s a^2}{4r_s^3}\left\{\frac{15}{2}e^2\left[C_L^2 C_{\Omega-\Lambda}^2 - (C_i C_L S_{\Omega-\Lambda} - S_L S_i)^2\right] C_{2\omega}\right. \\ &+ 15e^2\left[C_L S_L S_i C_{\Omega-\Lambda} - C_L^2 C_i C_{\Omega-\Lambda} S_{\Omega-\Lambda}\right] S_{2\omega} \\ &+ \left.\left(2+3e^2\right)\left[\frac{3}{2}\left[C_L^2 C_{\Omega-\Lambda}^2 + (C_i C_L S_{\Omega-\Lambda} - S_L S_i)^2\right] - 1\right]\right\} \qquad (49)\end{aligned}$$

Eqs (19) and (49) combine to form the complete disturbing function being considered in this investigation:

$$R = \overline{R_m} + \overline{R_s} \qquad (50)$$

Analytical Determination of the Location of Critical Inclinations

The last section detailed the derivation of the disturbing function which will be incorporated into the LPEs for numerical integration. The resulting disturbing function was obtained by averaging on 2π over the satellite mean anomaly for both the Mars disturbing function and the Solar disturbing function. What remains, however, are the time dependent terms of the Sun's motion, namely the solar central angle θ_s and the solar latitude L (see Figure 5). Averaging with respect to these terms fascillitates the development of an analytical approach for determining the location of the critical inclinations (see (5:182-192)). The purpose of this section is to examine the conditions under which such averaging is valid, and to summarize the results of this approach.

The averaging of any cyclic parameter is valid when its variation is faster than the variation of the other variables involved. Averaging with respect to the mean anomaly is valid since, in this investigation, the orbit period is shorter than the period of the variation of the argument of periapse ω or of the argument of the ascending node Ω. To average out the effects of θ_s and L, the mean motion of the Sun n_s must also be greater than the rate at which ω and Ω vary. The conditions for which this relationship holds will now be demonstrated.

To obtain an order-of-magnitude comparison of these terms, the LPEs may be used directly. Also, since $\overline{R_m} \gg \overline{R_s}$, only $\overline{R_m}$ will be used for this comparison. Using Eqs (2), (4), and (19):

$$\frac{\partial \overline{R_m}}{\partial i} = -\frac{3n^2 J_2 R_e^2}{2(1-e^2)^{3/2}} \sin i \cos i \tag{51}$$

$$\frac{\partial \overline{R_m}}{\partial e} = \frac{3n^2 J_2 R_e^2 e}{2(1-e^2)^{5/2}} \left(1 - \frac{3}{2}\sin^2 i\right) \tag{52}$$

$$\frac{d\Omega}{dt} = -\frac{3nJ_2 R_e^2}{2a^2(1-e^2)^2} \cos i \tag{53}$$

$$\frac{d\omega}{dt} = \frac{3nJ_2 R_e^2}{2a^2(1-e^2)^2} \left(1 - \frac{3}{2}\sin^2 i\right) + \frac{3nJ_2 R_e^2}{2a^2(1-e^2)^2} \cos^2 i \tag{54}$$

Considering only the magnitudes of the rates of change of Ω and ω, the following approximations may be obtained:

$$\frac{d\Omega}{dt} \approx \frac{d\omega}{dt} \approx \frac{J_2 R_e^2 \mu_m^{1/2}}{a^{7/2}(1-e^2)^2} \tag{55}$$

Therefore, averaging the effects of the Sun's mean motion n_s is valid when

$$n_s \gg \frac{J_2 R_e^2 \mu_m^{1/2}}{a^{7/2}(1-e^2)^2} \tag{56}$$

The parameters in Eq (56) have the following approximate values (12):

$$\begin{aligned} J_2 &= 0.0019604 \\ R_e &= 3395\, km \\ \mu_m &= 42828\, km^3/sec^2 \\ n_s &= 1.058 \times 10^{-7}\, sec^{-1} \end{aligned}$$

The motivation for using high eccentricity orbits is to reduce orbit insertion costs while allowing for a satellite mission which requires close approaches. To meet this requirement, consider the periapse radius r_p to be in the range $4000\, km \leq r_p \leq 7000\, km$ (it will be shown surface impacts due to the variation of eccentriciy do not allow the examination of periapse radii smaller than $4000\, km$). Using the relation $a = r_p/(1-e)$, averaging the solar central angle requires

$$n_s \gg \frac{J_2 R_e^2 \mu_m^{1/2}}{\left(\frac{r_p}{1-e}\right)^{7/2}(1-e^2)^2} \equiv Q \tag{57}$$

Figure 9 presents a plot of Q vs e for various values of periapse radius, along with the plot of n_s for comparison. The figure indicates averaging the effects of the Sun is valid for high-eccentricity orbits, with the lower bound on eccentricity increasing with decreasing periapse radius.

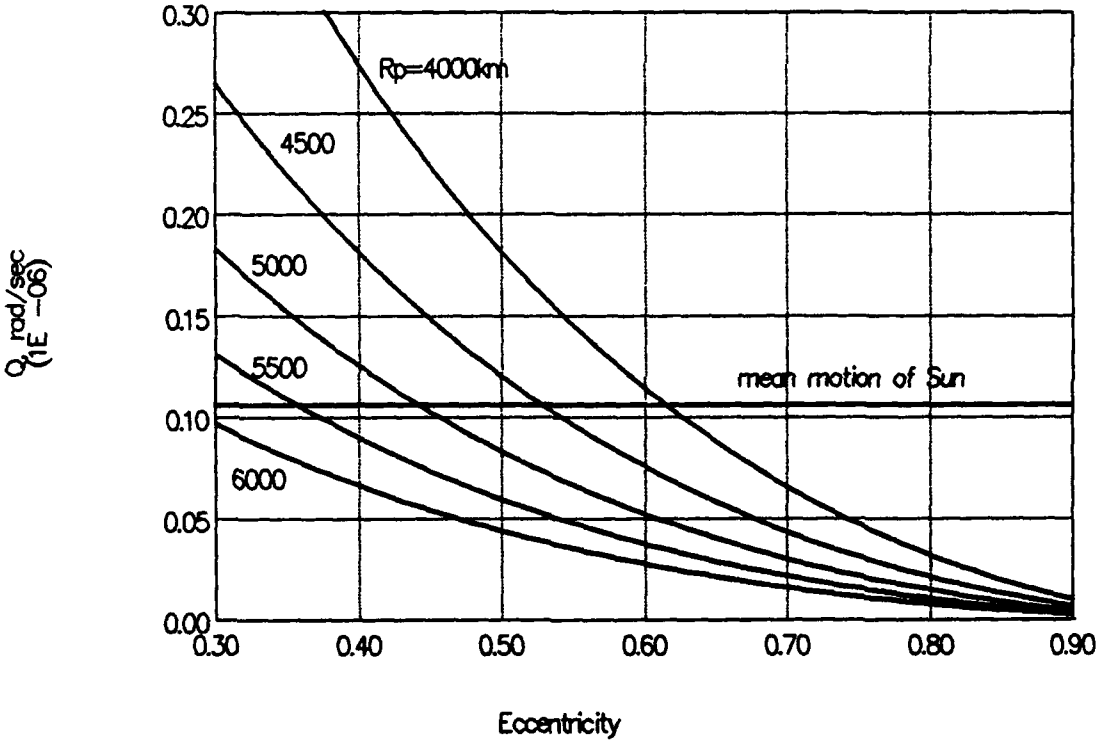

Figure 9. Approximate Magnitude (Q) of $\dot{\omega}$ and $\dot{\Omega}$ vs e for Various Values of Periapse Radius

Averaging the motion of the Sun within the range determined above produces a disturbing function which no longer contains time-varying solar elements. The Hamiltonian for this system may be formed (10, 8, 6), allowing for a canonical transformation into a new set of variables in which the new disturbing function is expandable in powers of J_2. Higher order terms are then ignored, resulting in a disturbing function containing critical divisors (7), all of which are functions only of inclination. The resulting critical inclinations which lie between 0° and 90° are given in the table below.

Table 1. Critical Inclinations from Analytical Approach

i_c (degrees)
46.4
56.1
63.4
69.0
73.2

The numerical approach which follows does not invoke the simplifications of solar averaging and includes all terms related to J_2. The results of the numerical integration will be shown to depart from the analytical results given in the table above.

III. Numerical Development and Results

Numerical Solution of Lagrange's Planetary Equations

Using the disturbing function derived in the last chapter, the LPEs may now be numerically integrated. Integration was accomplished using a multi-step, variable step size and variable order scheme (see [8] and [11]). To avoid numerical difficulties which arise when the classical variable set $(a, e, i, \omega, \Omega, M)$ is used, the following transformations are utilized:

$$h = e\sin\omega \tag{58}$$

$$k = e\cos\omega \tag{59}$$

and

$$\lambda_N = \frac{M+\omega}{S_0} + (\Omega - \phi) \tag{60}$$

where ϕ is the Mars equivalent of the Greenwich hour angle and S_0 approximates the ratio of the number of orbits per planet revolution. The variables h and k are introduced in order to avoid the singularity at zero eccentricity. The variable λ_N , which is called the stroboscopic mean node [6], represents the mean satellite position. Introduction of λ_N allows for averaging the mean anomaly while retaining the effects of resonances with tesseral harmonics. If the position of the satellite is commensurate with one or more tesserals, these tesserals will have long-term effects on the orbital elements (commensurability occurs when S_0 is a ratio of two integers).

Prior to casting the LPEs in terms of the new variable set $(a, h, i, k, \Omega, \lambda_N)$, note the disturbing function of interest does not include the mean anomaly, which was averaged out. Therefore, the semi-major axis a remains constant $(da/dt = 0)$. Also, since J_2 is the only harmonic considered, the stroboscopic mean node is not needed. The six original LPEs (Eqs. 2 to 7) reduce to four (Eqs. 2, 3, 4, and 6). Transforming these four into the new variable set requires the following derivatives:

$$\begin{aligned}\frac{\partial R}{\partial \omega} &= \frac{\partial R}{\partial h}\frac{\partial h}{\partial \omega} + \frac{\partial R}{\partial k}\frac{\partial k}{\partial \omega} \\ &= k\frac{\partial R}{\partial h} - h\frac{\partial R}{\partial k}\end{aligned} \tag{61}$$

$$\begin{aligned}\frac{\partial R}{\partial e} &= \frac{\partial R}{\partial h}\frac{\partial h}{\partial e} + \frac{\partial R}{\partial k}\frac{\partial k}{\partial e} \\ &= \frac{h}{e}\frac{\partial R}{\partial h} + \frac{k}{e}\frac{\partial R}{\partial k}\end{aligned} \tag{62}$$

$$\begin{aligned}\frac{dh}{dt} &= \frac{\partial h}{\partial e}\frac{de}{dt} + \frac{\partial h}{\partial \omega}\frac{dw}{dt} = \frac{h}{e}\frac{de}{dt} + k\frac{d\omega}{dt} \\ &= \frac{h}{e}\left(-\frac{b}{na^3e}\right)\left(k\frac{\partial R}{\partial h} - h\frac{\partial R}{\partial k}\right) + k\left[-\frac{\cos i}{nab\sin i}\frac{\partial R}{\partial i} + \frac{b}{na^3e}\left(\frac{h}{e}\frac{\partial R}{\partial h} + \frac{k}{e}\frac{\partial R}{\partial k}\right)\right] \\ &= \frac{b}{na^3}\frac{\partial R}{\partial k} - \frac{k\cos i}{nab\sin i}\frac{\partial R}{\partial i}\end{aligned} \tag{63}$$

$$\begin{aligned}\frac{dk}{dt} &= \frac{\partial k}{\partial e}\frac{de}{dt} + \frac{\partial k}{\partial \omega}\frac{d\omega}{dt} = \frac{k}{e}\frac{de}{dt} - h\frac{d\omega}{dt} \\ &= \frac{k}{e}\left(-\frac{b}{na^3e}\right)\left(k\frac{\partial R}{\partial h} - h\frac{\partial R}{\partial k}\right) - h\left[-\frac{\cos i}{nab\sin i}\frac{\partial R}{\partial i} + \frac{b}{na^3e}\left(\frac{h}{e}\frac{\partial R}{\partial h} + \frac{k}{e}\frac{\partial R}{\partial k}\right)\right] \\ &= -\frac{b}{na^3}\frac{\partial R}{\partial h} + \frac{\cos i}{nab\sin i}\frac{\partial R}{\partial i}\end{aligned} \tag{64}$$

In terms of the new variable set, the pertinent LPEs become

$$\frac{d\Omega}{dt} = \frac{1}{nab\sin i}\frac{\partial R}{\partial i} \tag{65}$$

$$\frac{di}{dt} = \frac{\cot i}{nab}\left(k\frac{\partial R}{\partial h} - h\frac{\partial R}{\partial k}\right) - \frac{1}{nab\sin i}\frac{\partial R}{\partial \Omega} \tag{66}$$

$$\frac{dh}{dt} = \frac{b}{na^3}\frac{\partial R}{\partial k} - \frac{k\cot i}{nab}\frac{\partial R}{\partial i} \tag{67}$$

$$\frac{dk}{dt} = -\frac{b}{na^3}\frac{\partial R}{\partial h} + \frac{h\cot i}{nab}\frac{\partial R}{\partial i} \tag{68}$$

where $b = a(1-e^2)^{1/2}$ is the semi-minor axis as before, and

$$e = \sqrt{(h^2+k^2)} \tag{69}$$

The complete disturbing function in terms of the new variables is

$$\begin{aligned}R &= \frac{\mu_m J_2 R_e^2}{2a^3(1-h^2-k^2)^{3/2}}\left(1 - \frac{3}{2}\sin^2 i\right) \\ &+ \frac{\mu_s a^2}{4r_s^3}\left\{\frac{15}{2}\left[C_L^2 C_{\Omega-\Lambda}^2 - (C_i C_L S_{\Omega-\Lambda} - S_L S_i)^2\right]\left(k^2 - h^2\right)\right. \\ &+ 30\left[C_L S_L S_i C_{\Omega-\Lambda} - C_L^2 C_i C_{\Omega-\Lambda} S_{\Omega-\Lambda}\right]hk \\ &+ \left.\left(2 + 3h^2 + 3k^2\right)\left[\frac{3}{2}\left[C_L^2 C_{\Omega-\Lambda}^2 + (C_i C_L S_{\Omega-\Lambda} - S_L S_i)^2\right] - 1\right]\right\}\end{aligned} \tag{70}$$

The required partial derivatives are

$$\begin{aligned}\frac{\partial R}{\partial k} &= \frac{3\mu_m J_2 R_e^2 k}{2a^3\left(1-h^2-k^2\right)^{5/2}}\left(1-\frac{3}{2}\sin^2 i\right)\\ &+ \frac{\mu_s a^2}{4r_s^3}\left\{15\left[C_L^2 C_{\Omega-\Lambda}^2-\left(C_i C_L S_{\Omega-\Lambda}-S_L S_i\right)^2\right]k\right.\\ &+ 30\left[C_L S_L S_i C_{\Omega-\Lambda}-C_L^2 C_i C_{\Omega-\Lambda} S_{\Omega-\Lambda}\right]h\\ &+ \left.6k\left[\frac{3}{2}\left[C_L^2 C_{\Omega-\Lambda}^2+\left(C_i C_L S_{\Omega-\Lambda}-S_L S_i\right)^2\right]-1\right]\right\} \qquad (71)\end{aligned}$$

$$\begin{aligned}\frac{\partial R}{\partial h} &= \frac{3\mu_m J_2 R_e^2 h}{2a^3\left(1-h^2-k^2\right)^{5/2}}\left(1-\frac{3}{2}\sin^2 i\right)\\ &+ \frac{\mu_s a^2}{4r_s^3}\left\{-15\left[C_L^2 C_{\Omega-\Lambda}^2-\left(C_i C_L S_{\Omega-\Lambda}-S_L S_i\right)^2\right]h\right.\\ &+ 30\left[C_L S_L S_i C_{\Omega-\Lambda}-C_L^2 C_i C_{\Omega-\Lambda} S_{\Omega-\Lambda}\right]k\\ &+ \left.6h\left[\frac{3}{2}\left[C_L^2 C_{\Omega-\Lambda}^2+\left(C_i C_L S_{\Omega-\Lambda}-S_L S_i\right)^2\right]-1\right]\right\} \qquad (72)\end{aligned}$$

$$\begin{aligned}\frac{\partial R}{\partial i} &= -\frac{3\mu_m J_2 R_e^2}{4a^3\left(1-h^2-k^2\right)^{3/2}}\sin 2i\\ &+ \frac{\mu_s a^2}{4r_s^3}\left\{15\left(C_i C_L S_{\Omega-\Lambda}-S_L S_i\right)\left(S_i C_L S_{\Omega-\Lambda}+S_L C_i\right)\left(k^2-h^2\right)\right.\\ &+ 30\left[C_L S_L C_i C_{\Omega-\Lambda}+C_L^2 S_i C_{\Omega-\Lambda} S_{\Omega-\Lambda}\right]hk\\ &- \left.3\left(2+3h^2+3k^2\right)\left(C_i C_L S_{\Omega-\Lambda}-S_L S_i\right)\left(S_i C_L S_{\Omega-\Lambda}+S_L C_i\right)\right\} \qquad (73)\end{aligned}$$

$$\begin{aligned}\frac{\partial R}{\partial \Omega} &= \frac{\mu_s a^2}{4r_s^3}\left\{-\frac{15}{2}\left[C_L^2 S_{2(\Omega-\Lambda)}+2\left(C_i C_L S_{\Omega-\Lambda}-S_L S_i\right)C_i C_L C_{\Omega-\Lambda}\right]\left(k^2-h^2\right)\right.\\ &- 30\left[C_L S_L S_i S_{\Omega-\Lambda}+C_L^2 C_i C_{2(\Omega-\Lambda)}\right]hk\\ &- \left.\frac{3}{2}\left(2+3h^2+3k^2\right)\left[C_L^2 S_{2(\Omega-\Lambda)}-2\left(C_i C_L S_{\Omega-\Lambda}-S_L S_i\right)C_i C_L C_{\Omega-\Lambda}\right]\right\} \qquad (74)\end{aligned}$$

The details of employing the numerical integrator to locate critical inclinations is described in the next section.

Locating Critical Inclinations

Figures 1 through 4 illustrated the phenomenon of large amplitude variations in eccentricity and inclination. These large variations occur under specific conditions, namely certain critical inclinations for high eccentricity orbits. The last section of Chapter II summarized an analytical approach for determining the location of these critical inclinations, which were found to be independent of eccentricity (i.e., constant). The resultant critical inclinations also had the property of producing a local maximum in the variations of both eccentricity and inclination. The intent of the numerical approach is to accomplish a discrete numerical search for the critical inclinations throughout a range of interest. For the purpose of this search, a critical inclination is defined as the inclination at orbit insertion which results in the largest local variation in eccentricity or inclination (i.e, a local maximum). No assumption is made concerning correlations between the behavior of the eccentricity and the behavior of inclination, therefore a separate search is made for each.

Search Method.

The numerical integrator produces an output data file consisting of the values of the orbital elements at time increments determined by the user. The behavior of the elements may be observed by plotting the data. However, the magnitude of the search demands the use of a numerical technique for locating the local maximums in the variations, thereby identifying the critical inclinations. The method employed is to fit a linear function, in the least squares sense [9:23-47], to the graph of eccentricity versus time and the graph of inclination verses time. The standard deviation of the residuals then becomes the tool for locating critical inclinations. The larger the variation in the behavior of these elements, the greater the standard deviation will be for the linear fit. By looping through the range of orbit insertion inclinations while keeping other initial conditions the same, critical inclinations for a given eccentricity are those which produce a local maximum in the plot of standard deviation verses inclination. An outer loop which increments the orbit insertion eccentricity completes the search, allowing for a three- dimensional surface to be plotted, where eccentricity and inclination are the independent variables, and standard deviation is the dependent variable. The 'peaks' in this surface are the points of interest.

Search Parameter Values and Initial Conditions.

The search method described above would be best accomplished with very small increments in eccentricity and inclination, combined with a sufficiently long propagation time. The plot in Figure 3, showing data which spans a period of seventy Earth years about Mars, does not yet exhibit a repeatable pattern. However, computer time and storage constraints did not allow for large data collection, therefore a smaller sample was used. This is not a serious constraint since large variations near critical inclinations become evident very soon after orbit insertion. Also, an orbit period of five or ten years may be of more immediate concern.

The table below lists the initial conditions and search parameter increments used to perform the numerical search. Choosing the periapse radius r_p determines the value of the semi-major axis by $a = r_p/(1 - e)$. For a complete listing of the program input file, see appendix B.

Table 2. Search Increment Values and Initial Conditions

ω at insertion	0
Ω at insertion	0
M at insertion	0
e at insertion	incremented from 0.40 to 0.90 by 0.02
i at insertion	incremented from 0.25 to 90.0 by 0.25 (degrees)
r_p at insertion	incremented from 4500 km to 7000 km by 500 km
orbit lifetime	10 Earth years
epoch at insertion	7 January 2001
data output increment	100 days

The effect of using a different epoch at orbit insertion was tested and found to produce no noticeable change in the results for the search range considered.

Critical Inclinations for Eccentricity

The inner loop of the search procedure described in the last section consisted of incrementing through the range of inclinations for a given eccentricity. For each of these insertion eccentricities, a plot of the standard deviation of the residuals in eccentricity (SDE) verses inclination may be generated. These plots are too numerous to include them all here, however, all such plots for a periapse radius of $6500km$ can be found in appendix D.

Three-Dimensional Surface Plots.

Combining all the plots of SDE vs Inclination for a given periapse radius allows for the generation of a three-dimensional plot, where the third axis is the range of eccentricities (these plots are presented in Figures 10 through 16). These surfaces indicate the locations of the critical inclinations, which vary with eccentricity.

Critical inclinations at eccentricities near 0.4 and inclinations near 0.25 degrees vary rapidly with eccentricity, generating a rough surface topography. This rough area moves *out of the search range as periapse* radius increases and is totally absent at periapse radii greater than 6000km. Subsequent analysis will therefore focus on the remaining smoother areas where pronounced topography is present throughout the range of interest.

Some of the surfaces do not contain the complete range of data (i.e., eccentricities between 0.4 and 0.9). Where this data is not present, large variations in the eccentricity caused the orbit to impact before the full set of data was collected. These computer runs were rejected (see appendix C for further discussion).

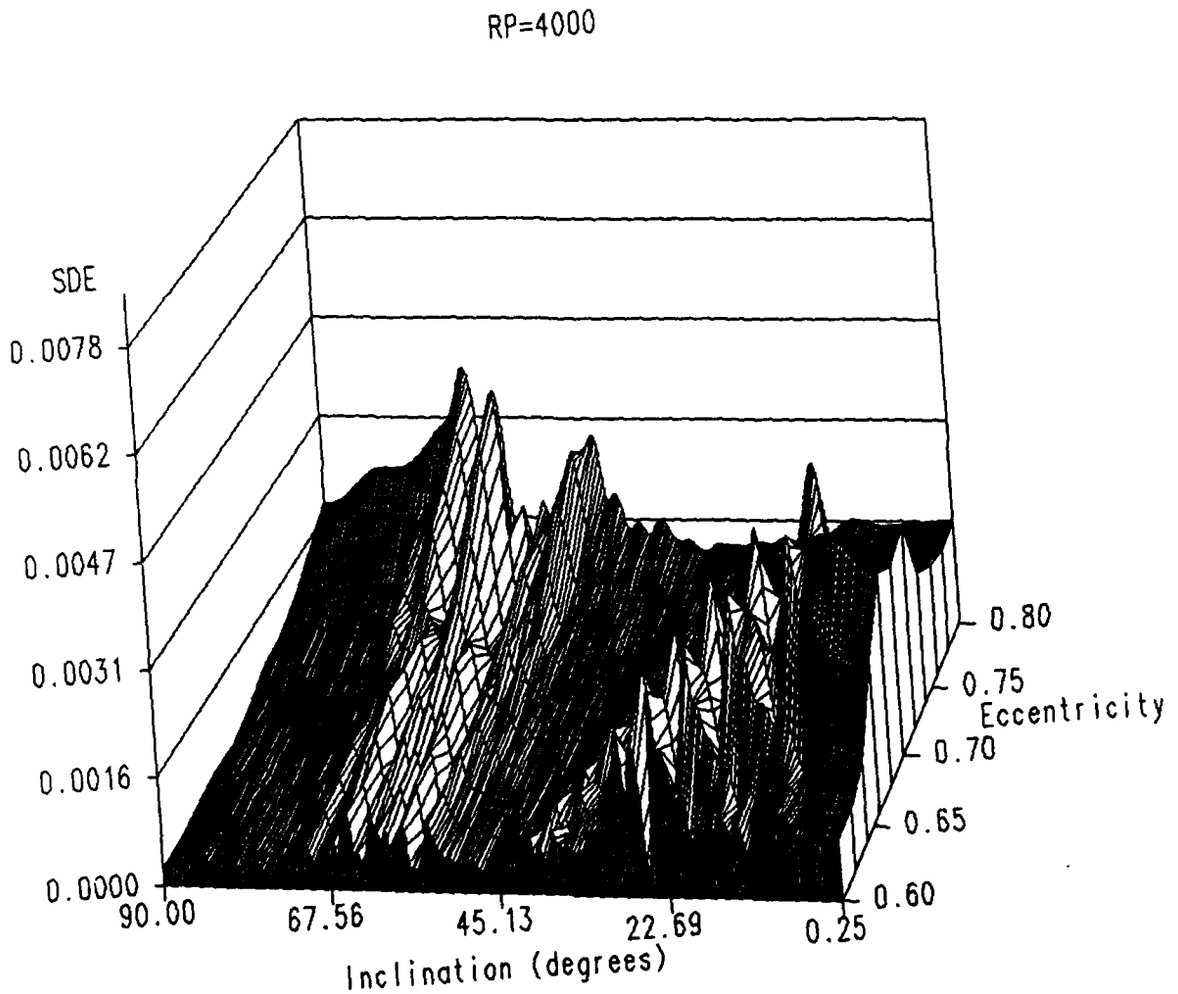

Figure 10. Standard Deviation in Eccentricity vs Inclination and Eccentricity : Periapse Radius=4000 km

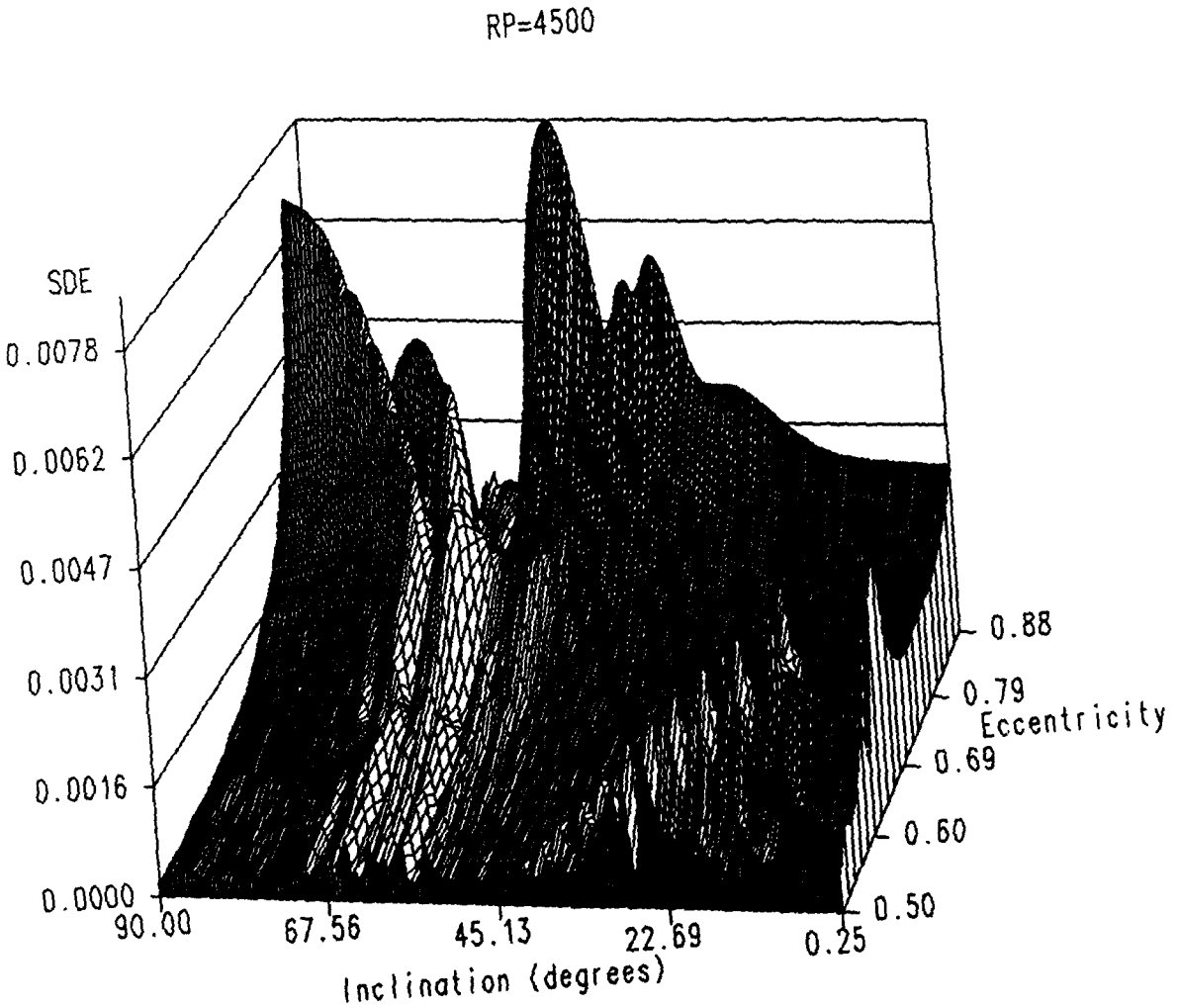

Figure 11. Standard Deviation in Eccentricity vs Inclination and Eccentricity : Periapse Radius=4500 km

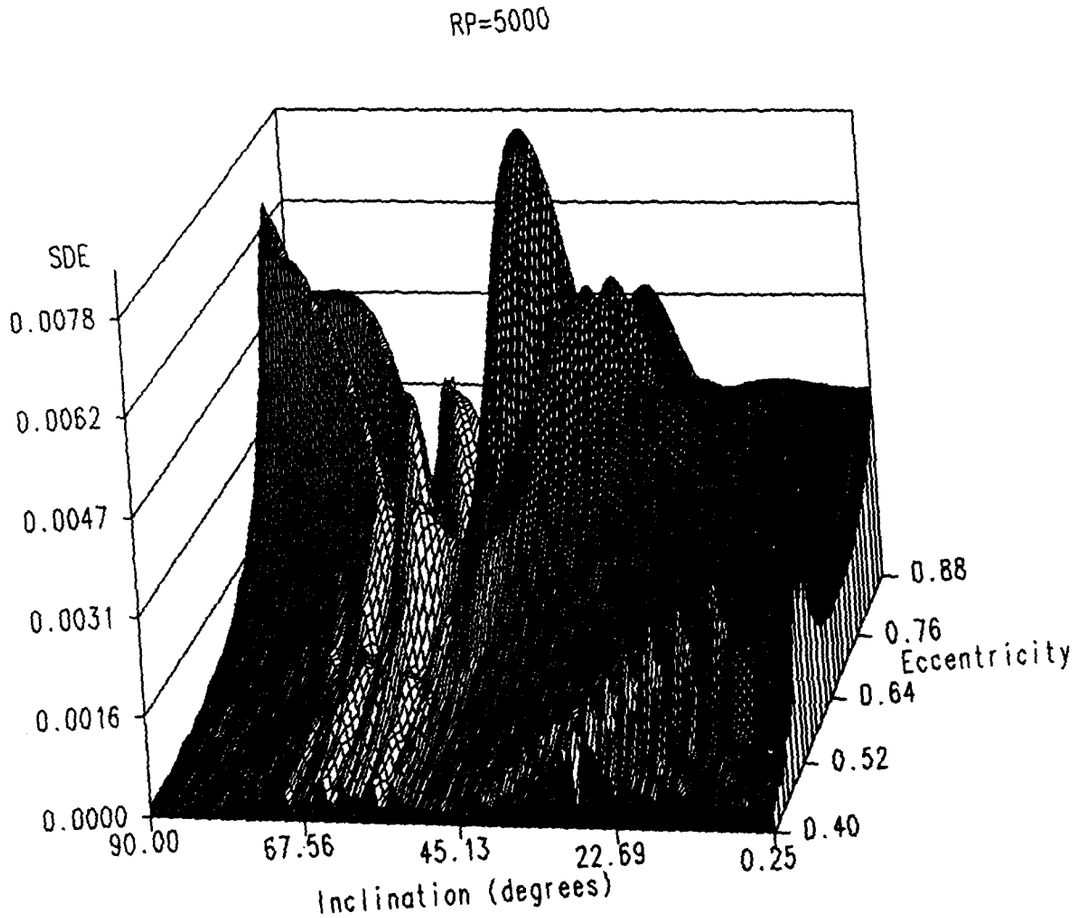

Figure 12. Standard Deviation in Eccentricity vs Inclination and Eccentricity : Periapse Radius=5000 km

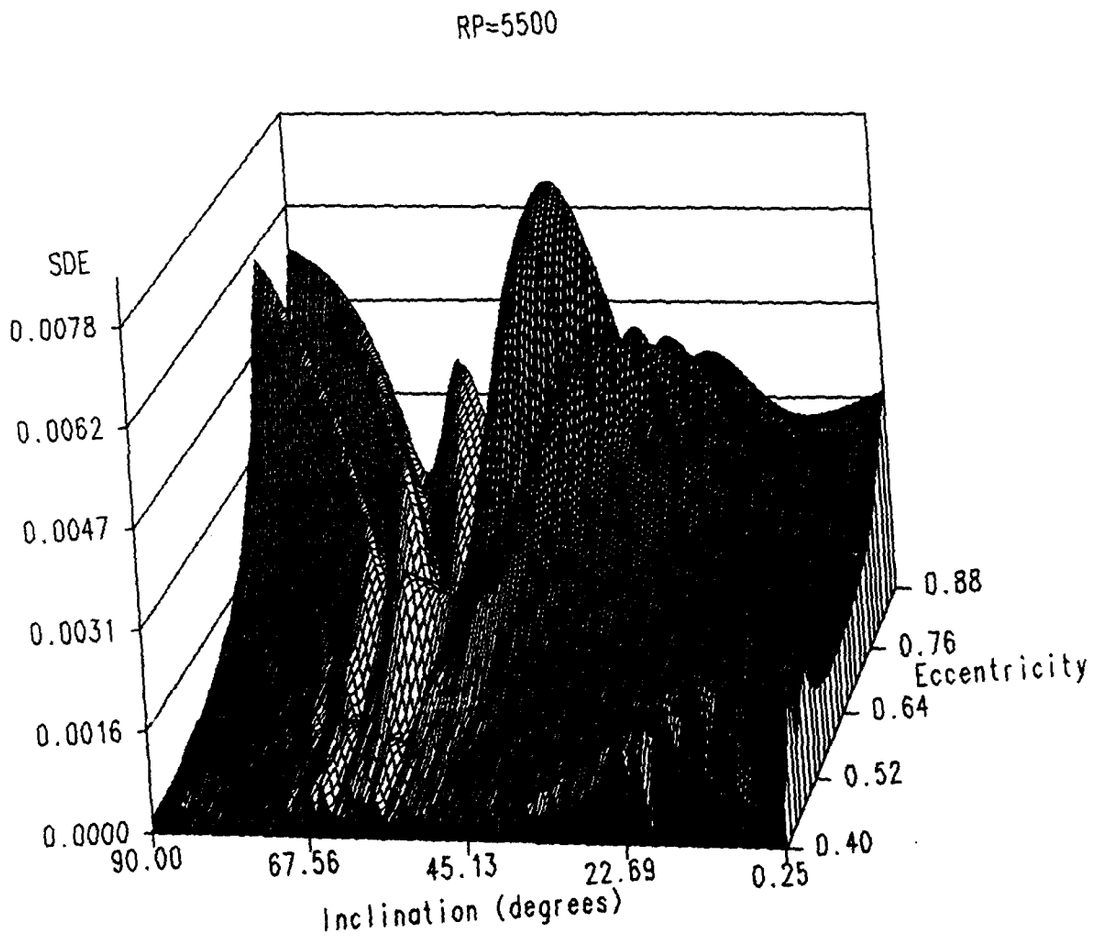

Figure 13. Standard Deviation in Eccentricity vs Inclination and Eccentricity : Periapse Radius=5500 km

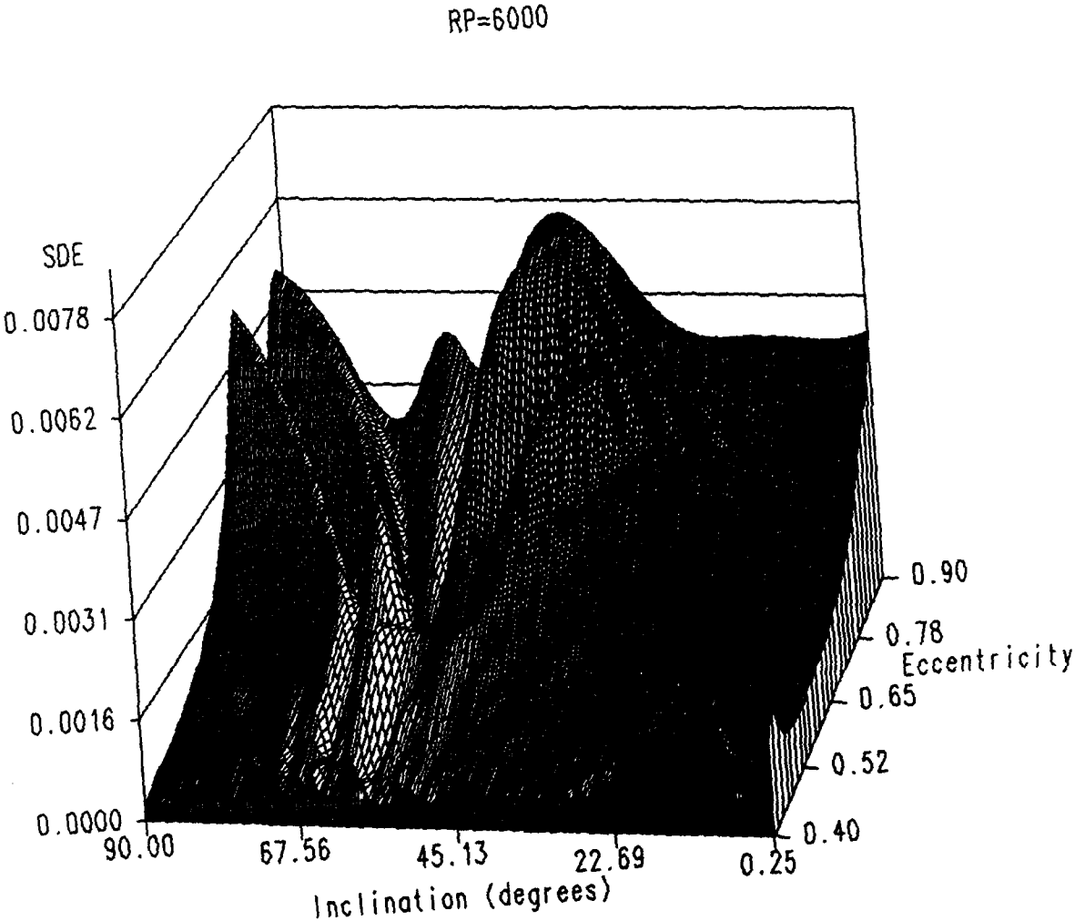

Figure 14. Standard Deviation in Eccentricity vs Inclination and Eccentricity : Periapse Radius=6000 km

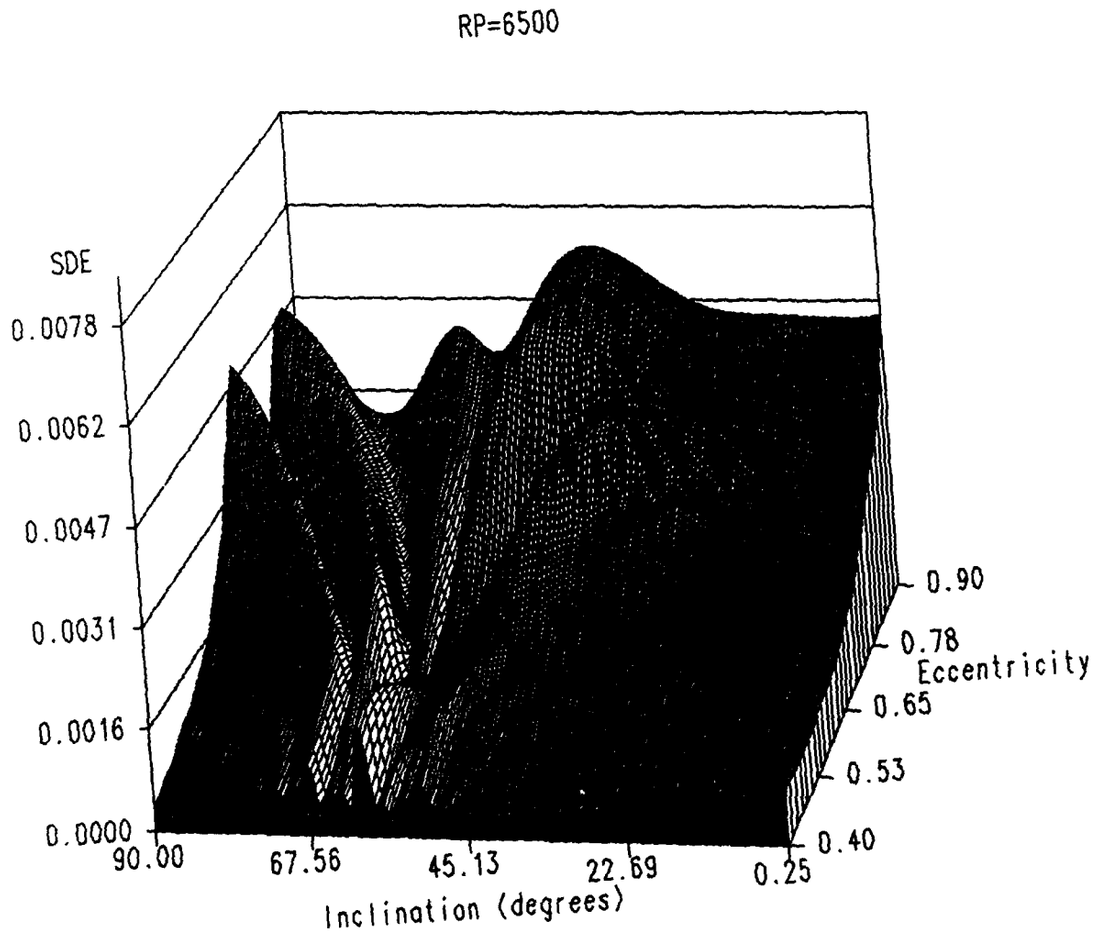

Figure 15. Standard Deviation in Eccentricity vs Inclination and Eccentricity : Periapse Radius=6500 km

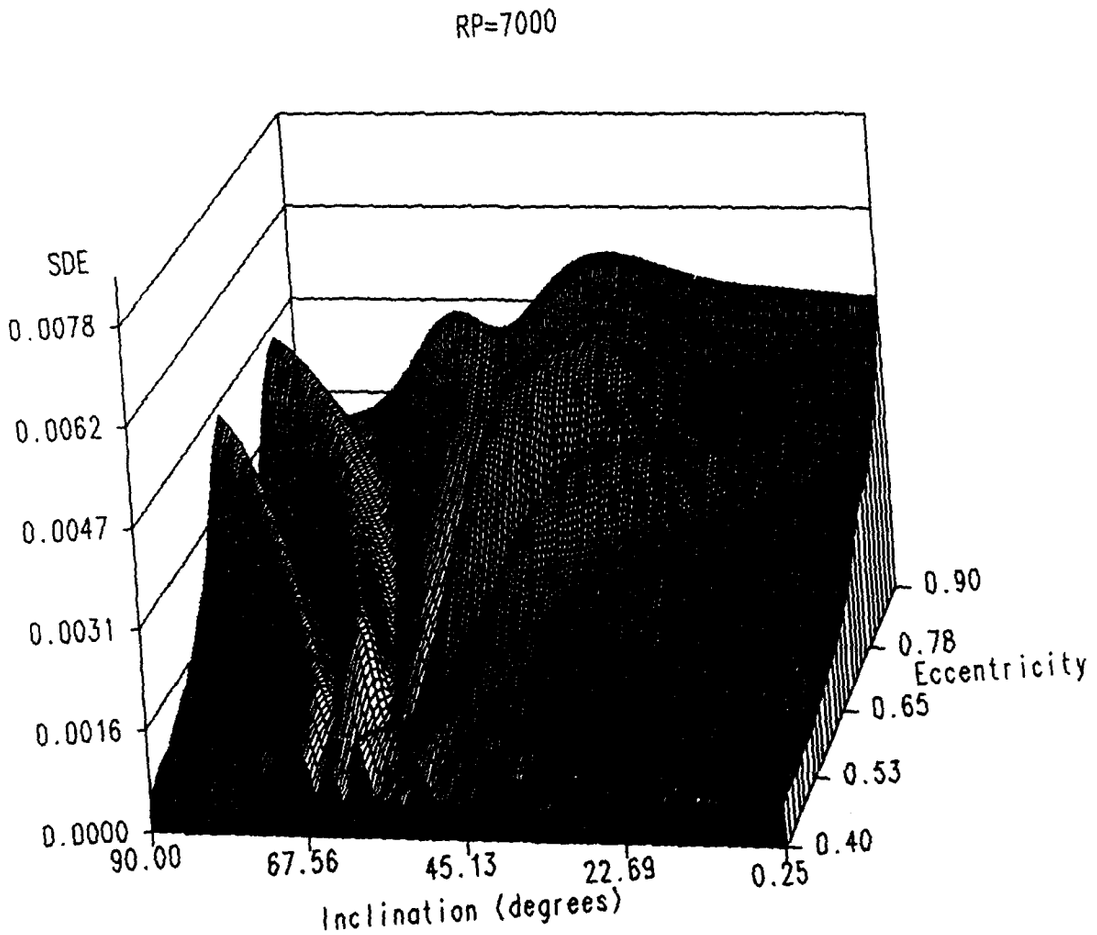

Figure 16. Standard Deviation in Eccentricity vs Inclination and Eccentricity : Perigee Radius=7000 km

Two-Dimensional Plots.

In order to reduce each three-dimensional surface to a two-dimensional plot of critical inclination verses eccentricity, the following procedure was employed. For each eccentricity considered, local maximums were identified by observing the slope of the line connecting adjacent data points in the plot of SDE versus inclination. A data point was considered a maximum (critical) when the slope of the line transitioned from positive to negative. Figures 10 through 16 indicate the presence of five significant critical inclination curves, as well as other smaller local maximums. These smaller maximums were filtered out, retaining maximums with the five greatest values of SDE. The resultant data is given in tabular form in appendix E, and the plots of critical inclinations verses eccentricity are given in Figures 17 through 22. Insufficient data was collected at periapse radius of 4000 km to produce a meaningful two-dimensional plot, therefore only periapse radii of 4500 km and above are presented.

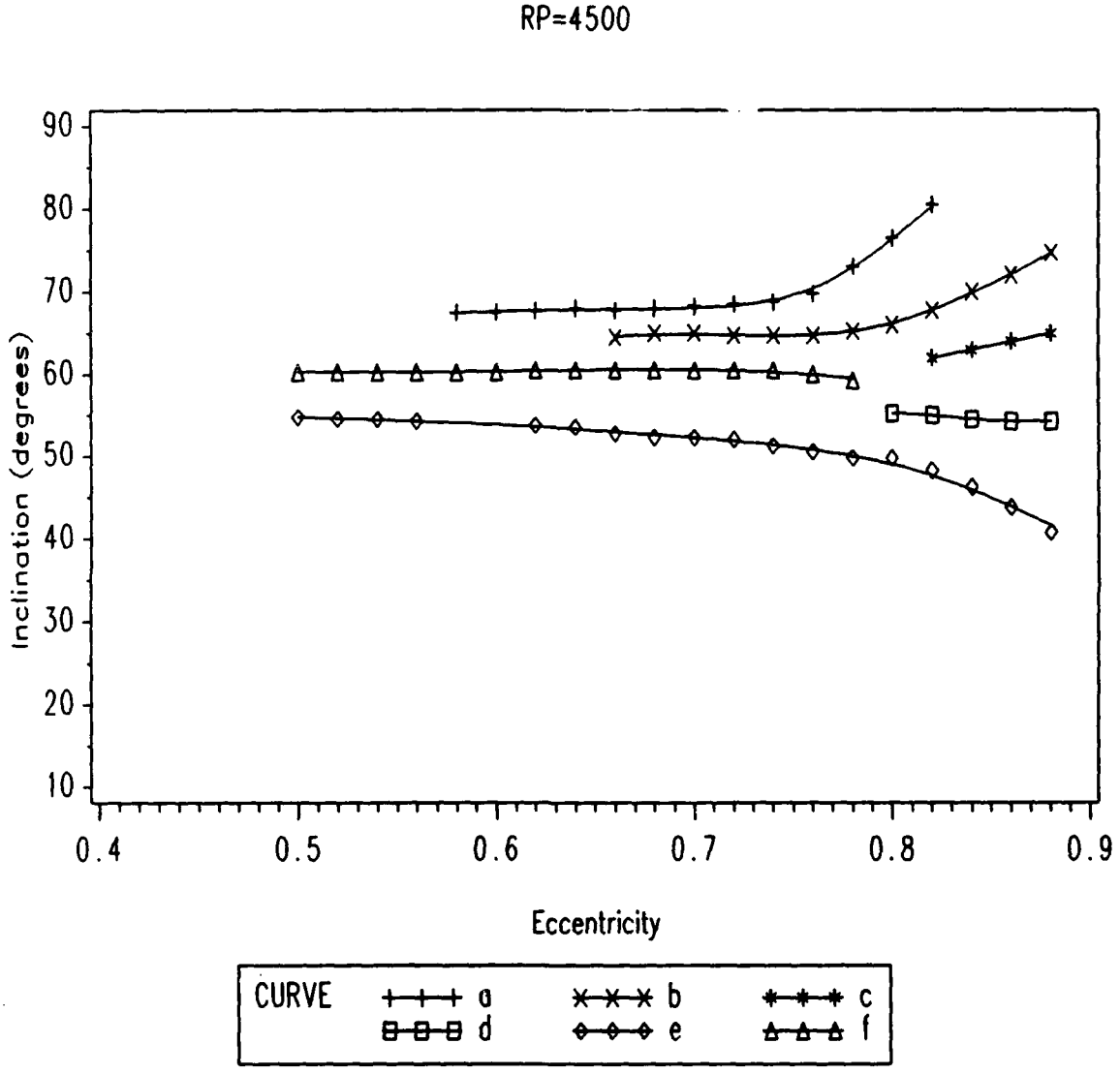

Figure 17. Critical Inclination vs Eccentricity: Periapse Radius=4500 km

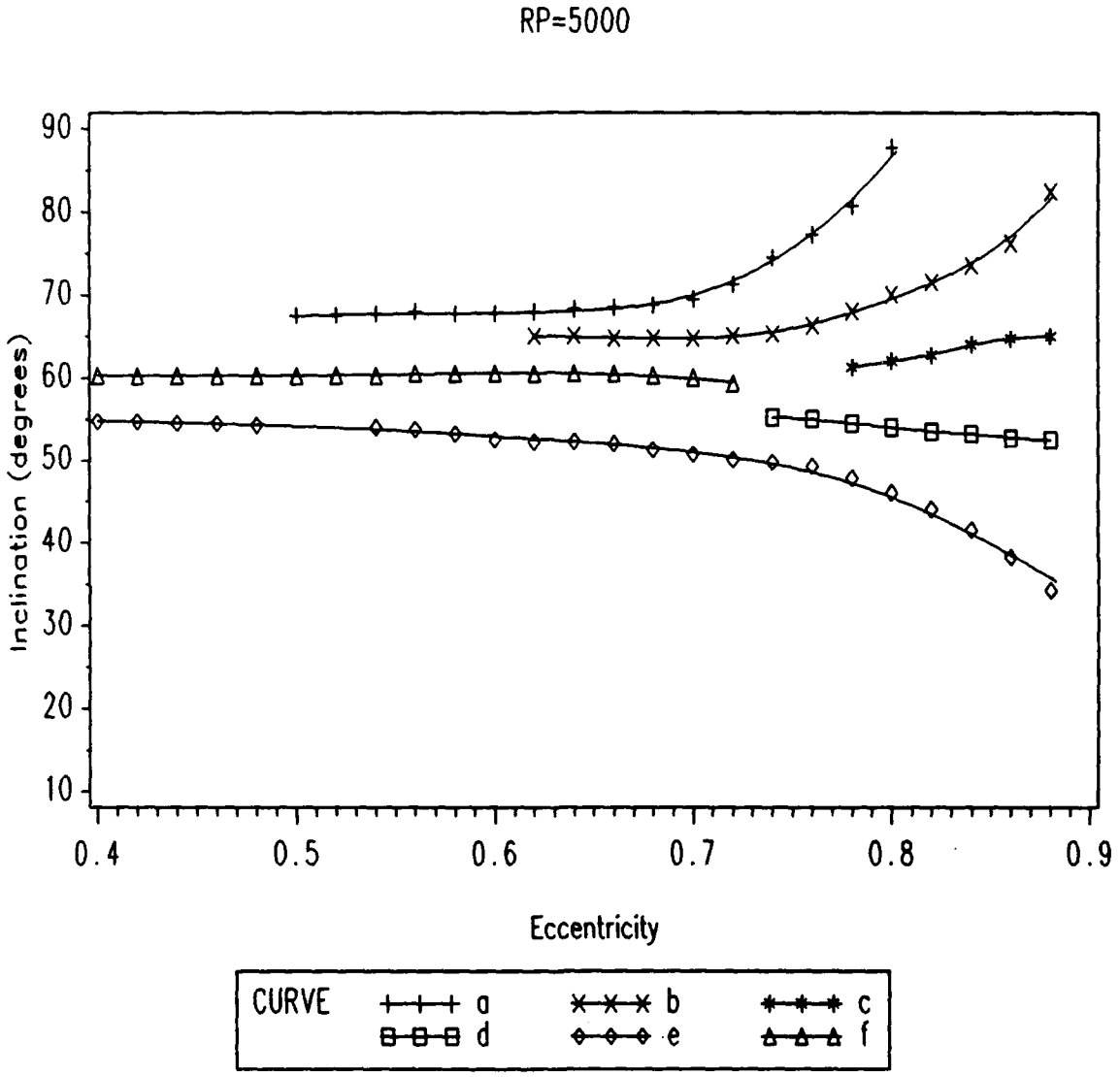

Figure 18. Critical Inclination vs Eccentricity: Periapse Radius=5000 km

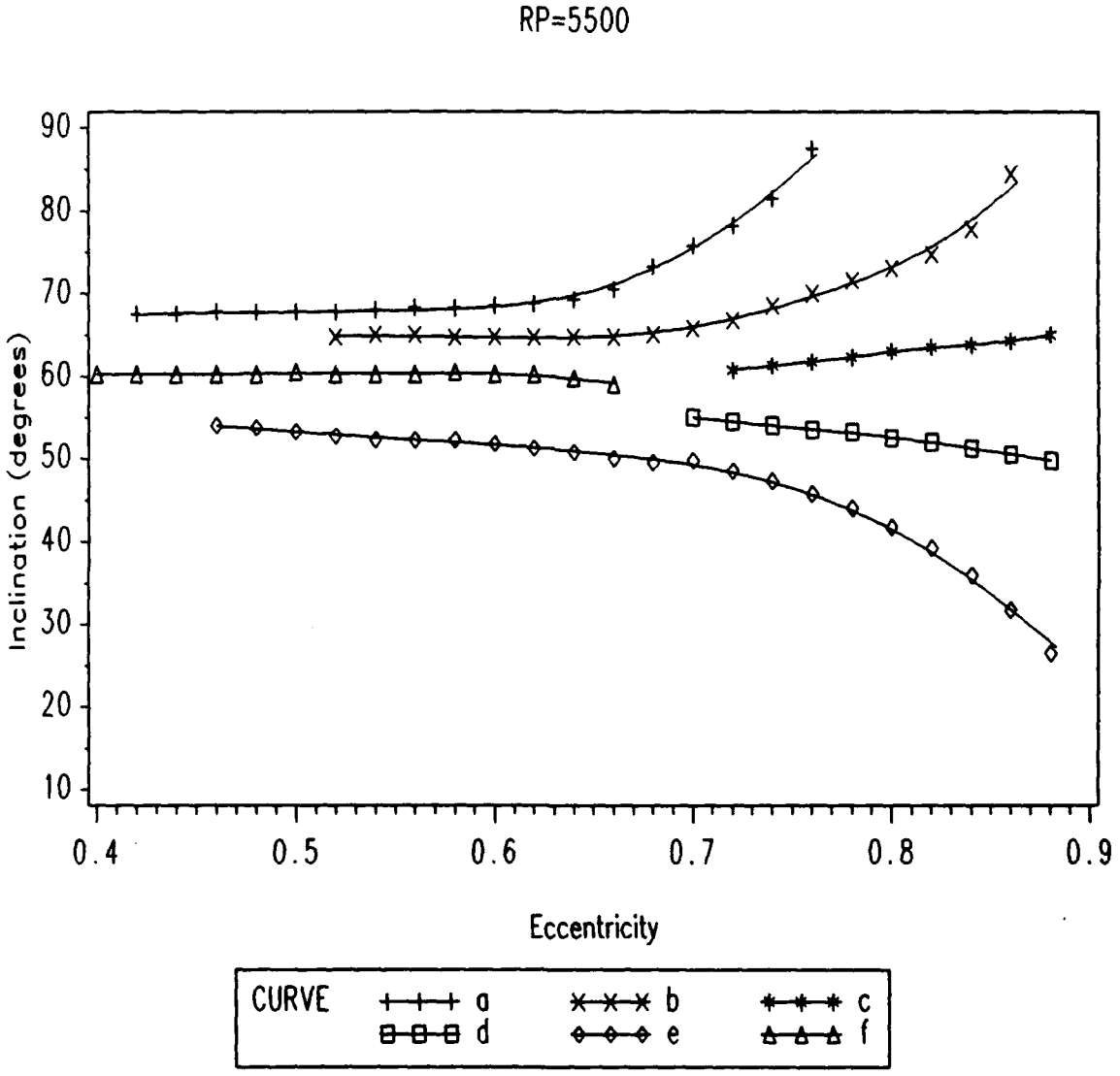

Figure 19. Critical Inclination vs Eccentricity: Periapse Radius=5500 km

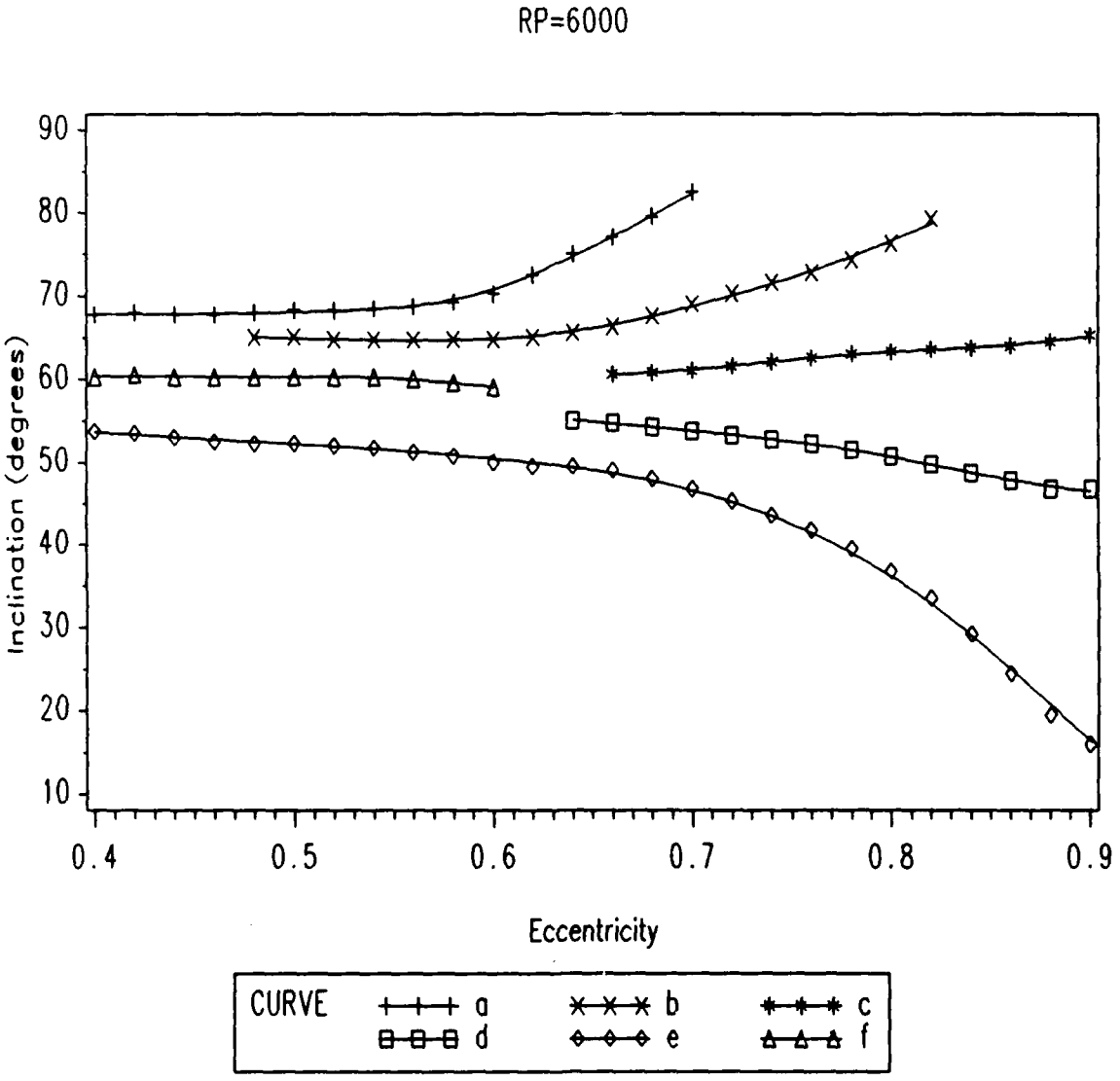

Figure 20. Critical Inclination vs Eccentricity: Periapse Radius=6000 km

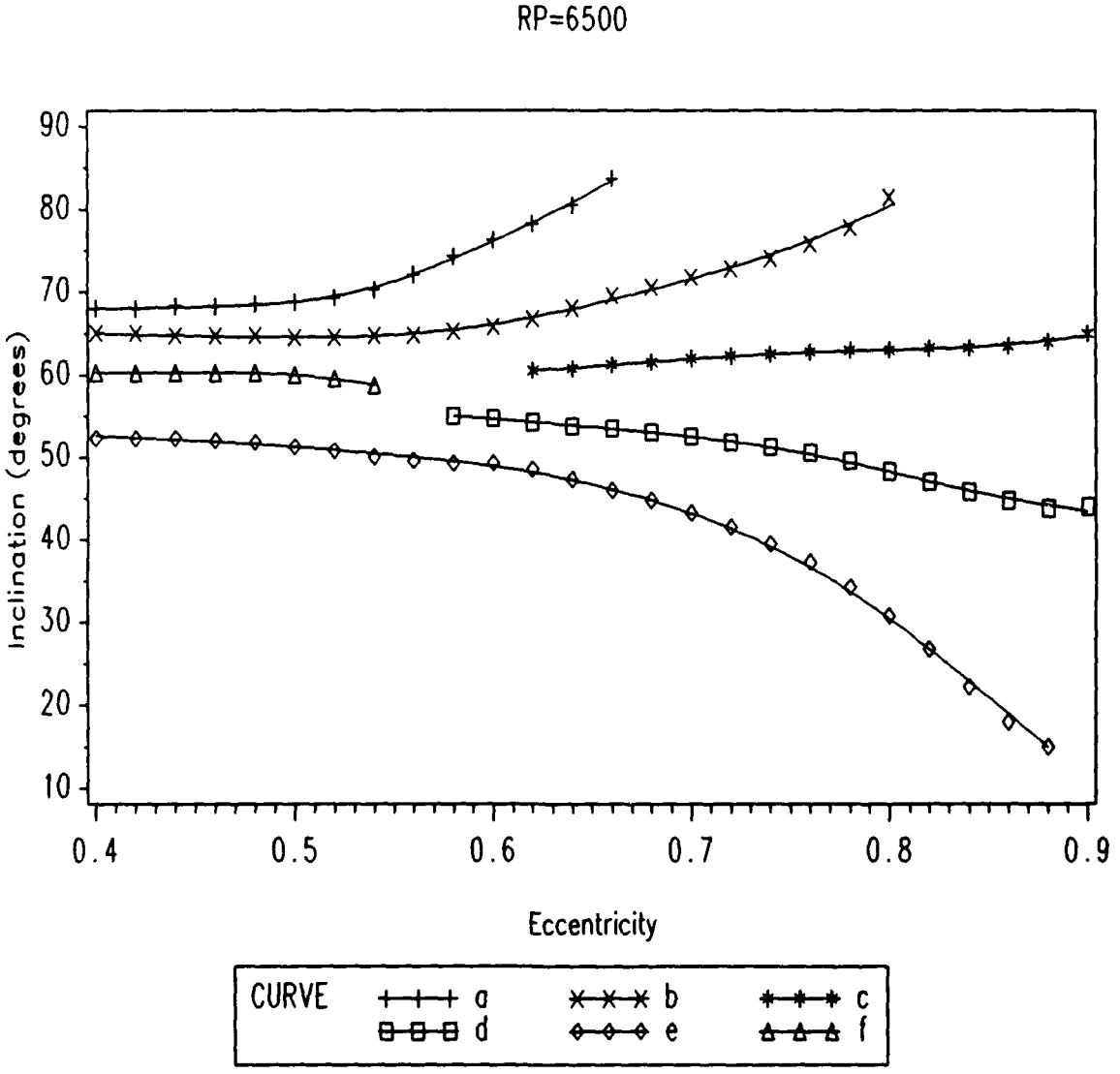

Figure 21. Critical Inclination vs Eccentricity: Periapse Radius=6500 km

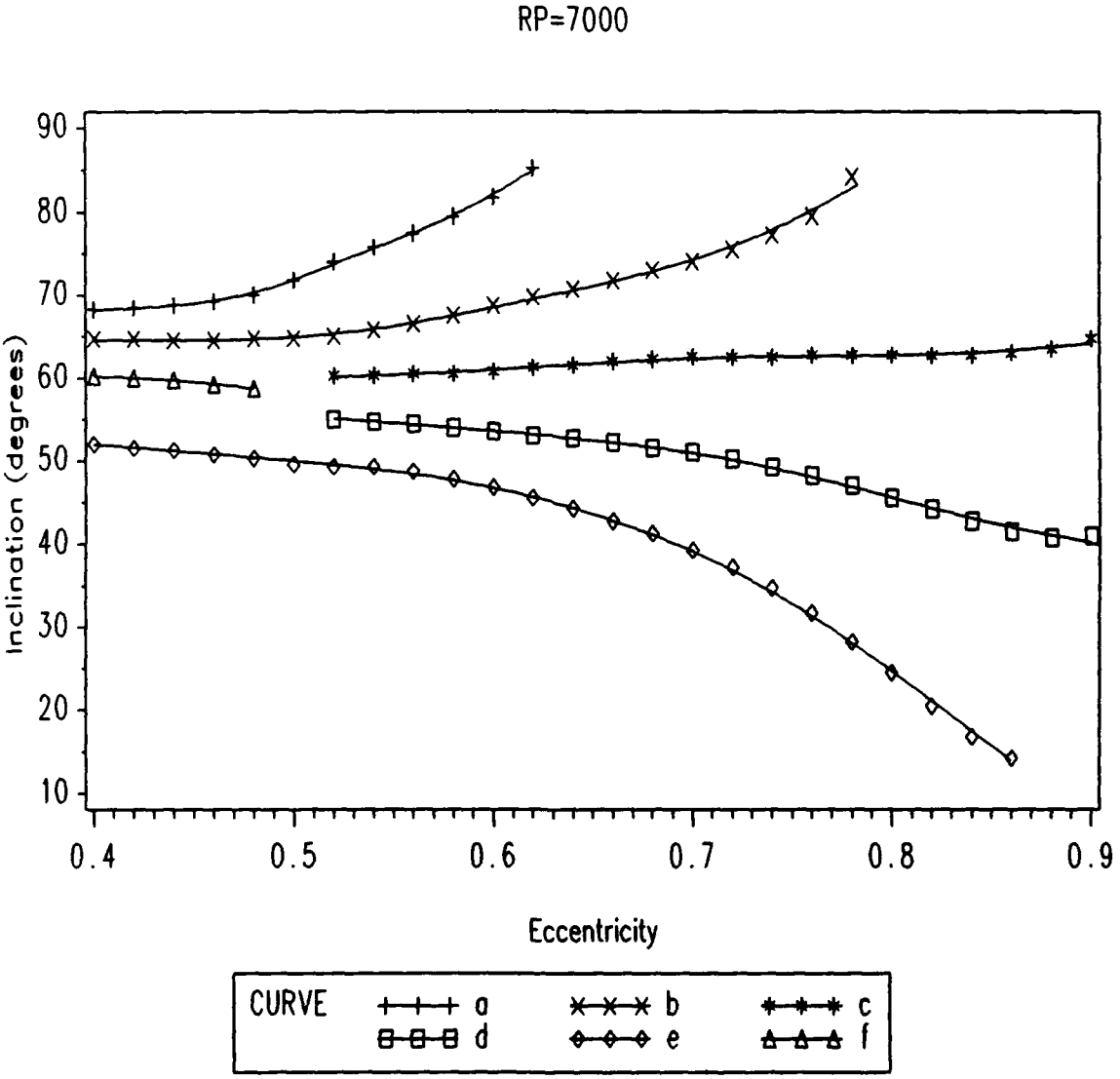

Figure 22. Critical Inclination vs Eccentricity: Periapse Radius=7000 km

Critical Inclinations for Inclination

The techniques for locating critical inclinations in eccentricity were also applied to inclination. Incrementing through the range of inclinations for a given eccentricity produces a plot of the standard deviation of the residuals in inclination (SDI) verses inclination (see appendix D). As before, combining the data for the full range of eccentricities allows for the creation of a three-dimensional surface plot for each periapse radius considered. These surface plots are given in Figures 23 through 29.

Unlike the surfaces for eccentricity, the surfaces for inclination indicate fewer distinct critical locations. The presence of one or two well pronounced critical locations in the surface topography at high eccentricities forces other possible critical locations to appear flat. Attempting to reduce the surfaces for inclination to two dimensions as was done for eccentricity did not produce meaningful results.

Although the attempt to produce a two-dimensional view of the critical values for inclination was not successful, overlapping the plots of SDE and SDI verses inclination *for each eccentricity* allows for a comparison of the location of the local maximums. Appendix D presents these plots for a periapse radius of 6500km. There is no indication of any correlation between the location of critical inclinations for eccentricity and critical inclinations for inclination. However, recall these results apply to a ten Earth-year orbit lifetime, which does not capture a full period of the large amplitude variations. A longer orbit lifetime may produce different results.

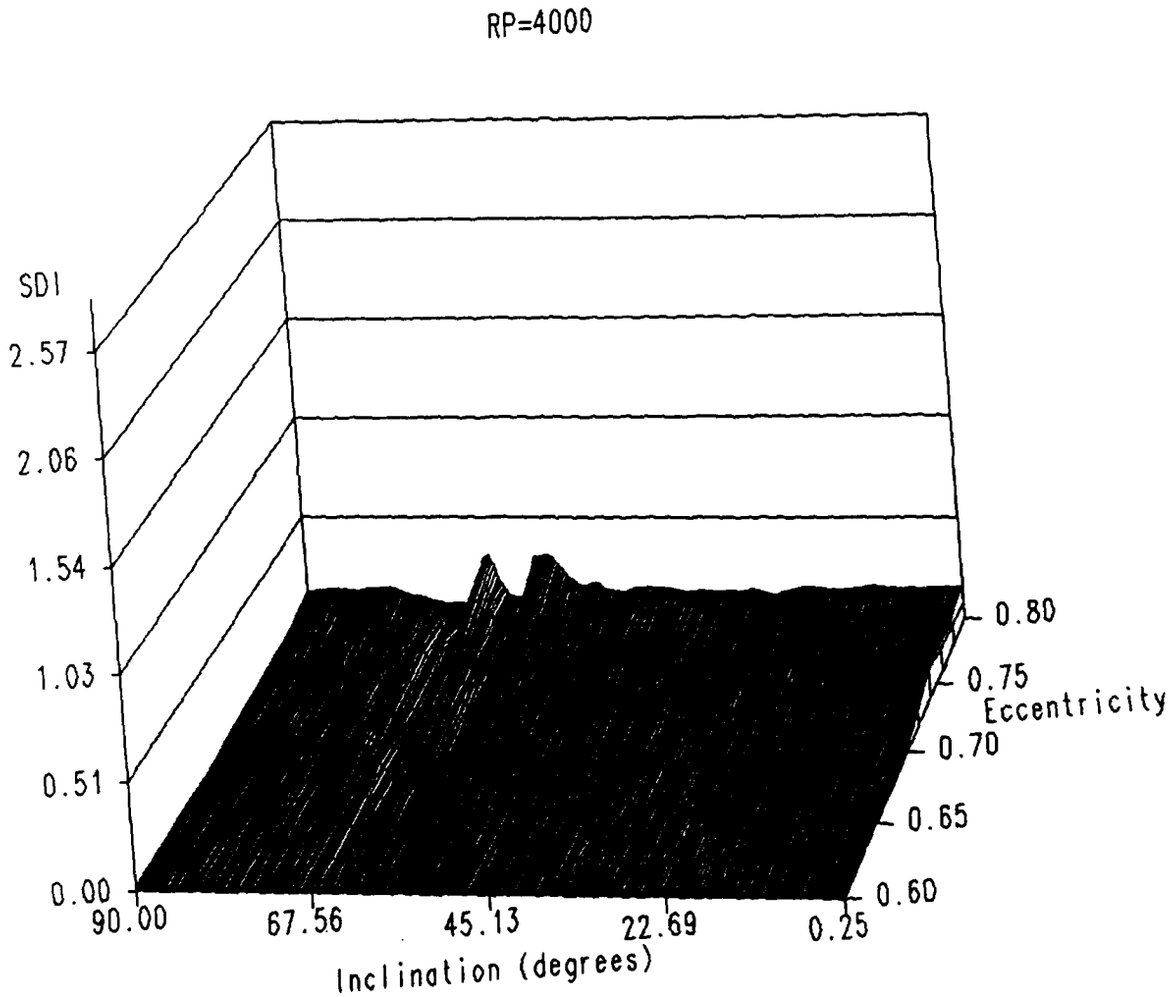

Figure 23. Standard Deviation in Inclination vs Eccentricity and Inclination : Periapse Radius=4000 km

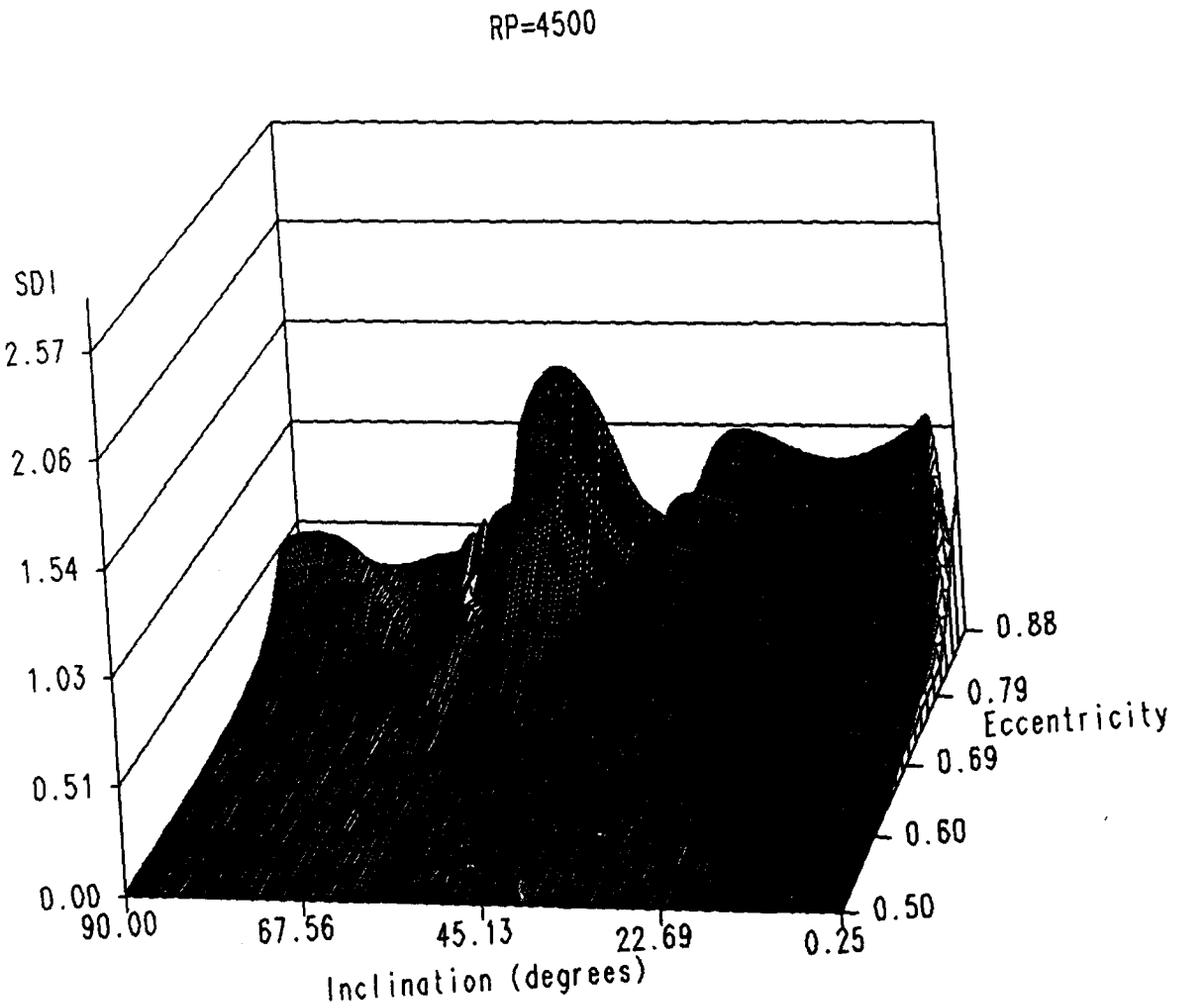

Figure 24. Standard Deviation in Inclination vs Eccentricity and Inclination : Periapse Radius=4500 km

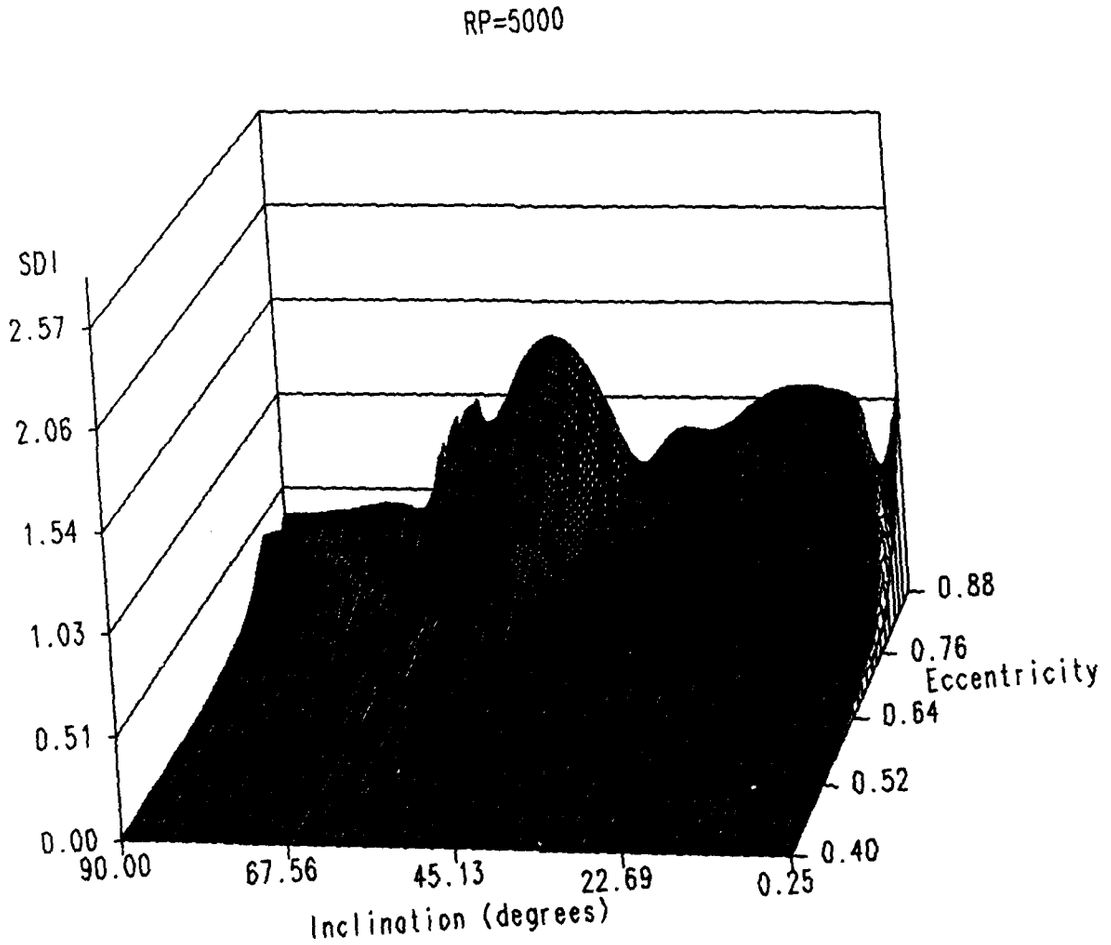

Figure 25. Standard Deviation in Inclination vs Eccentricity and Inclination : Periapse Radius=5000 km

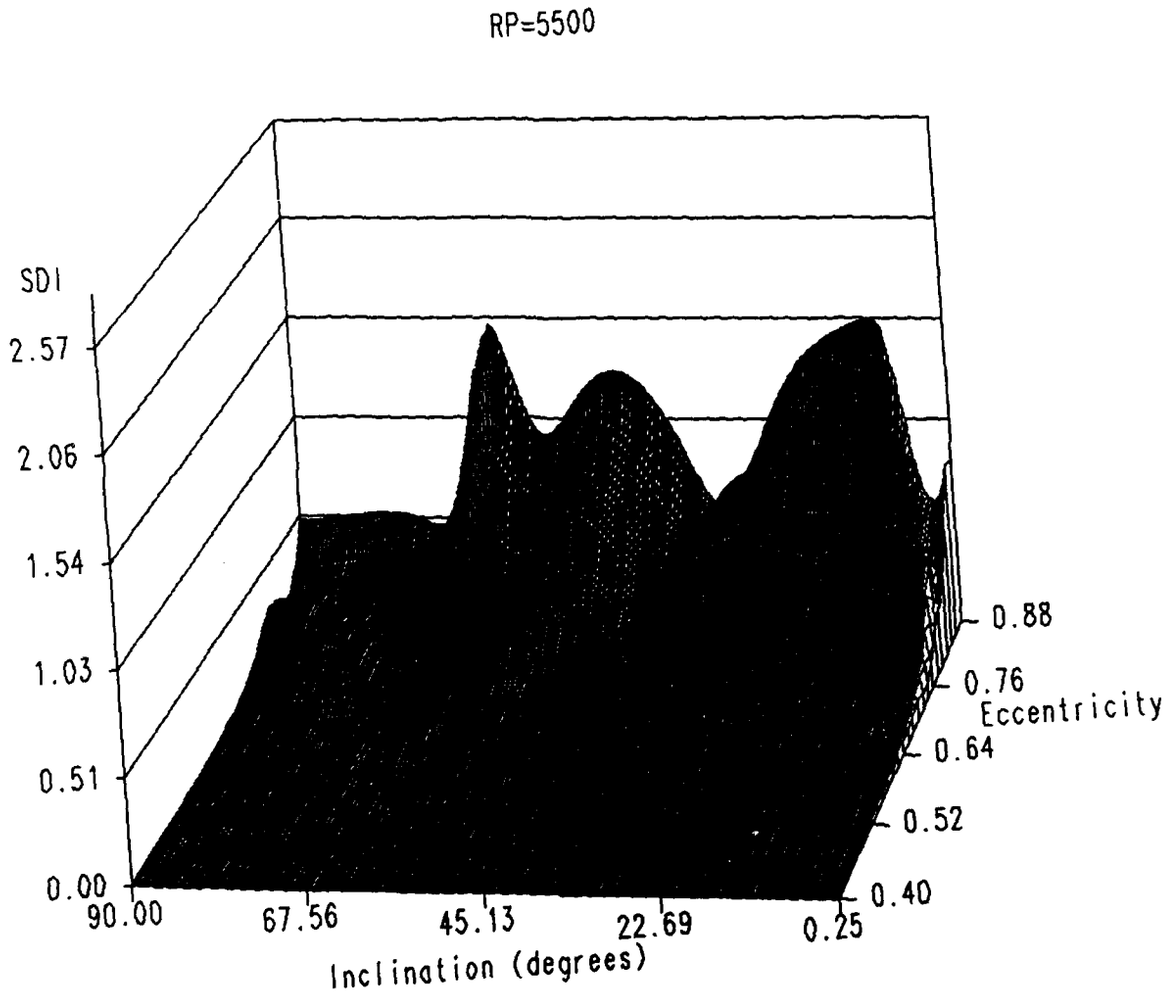

Figure 26. Standard Deviation in Inclination vs Eccentricity and Inclination : Periapse Radius=5500 km

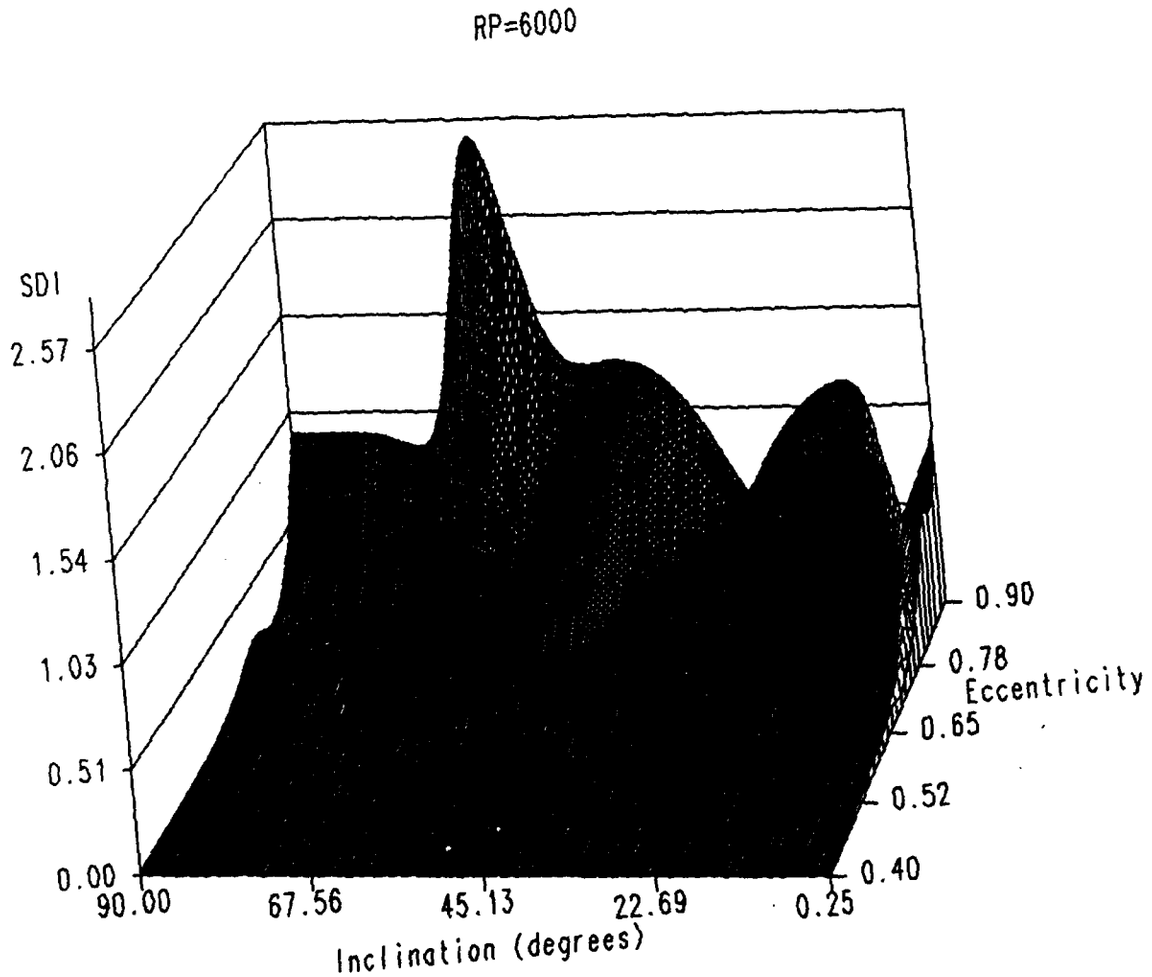

Figure 27. Standard Deviation in Inclination vs Eccentricity and Inclination : Perigee Radius=6000 km

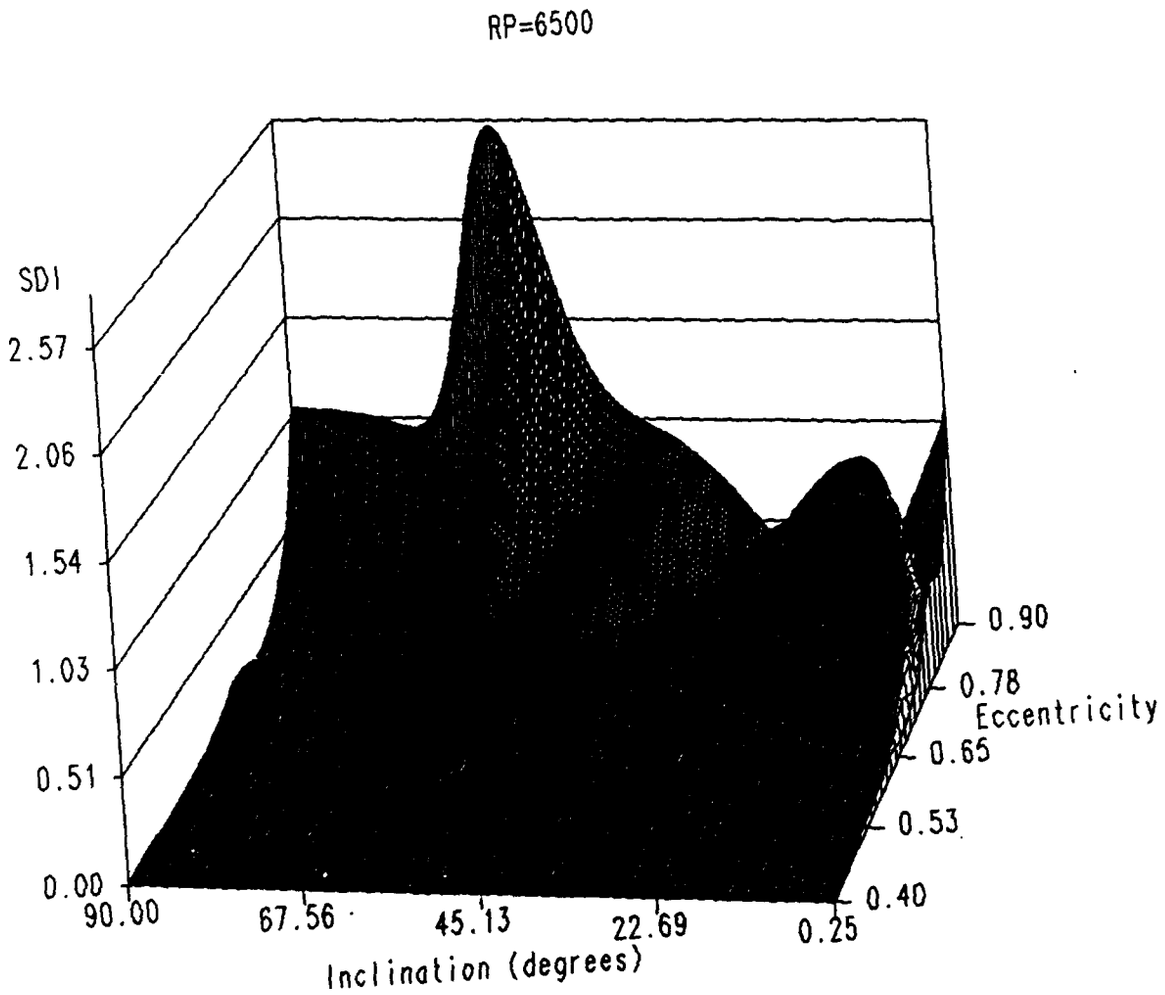

Figure 28. Standard Deviation in Inclination vs Eccentricity and Inclination : Periapse Radius=6500 km

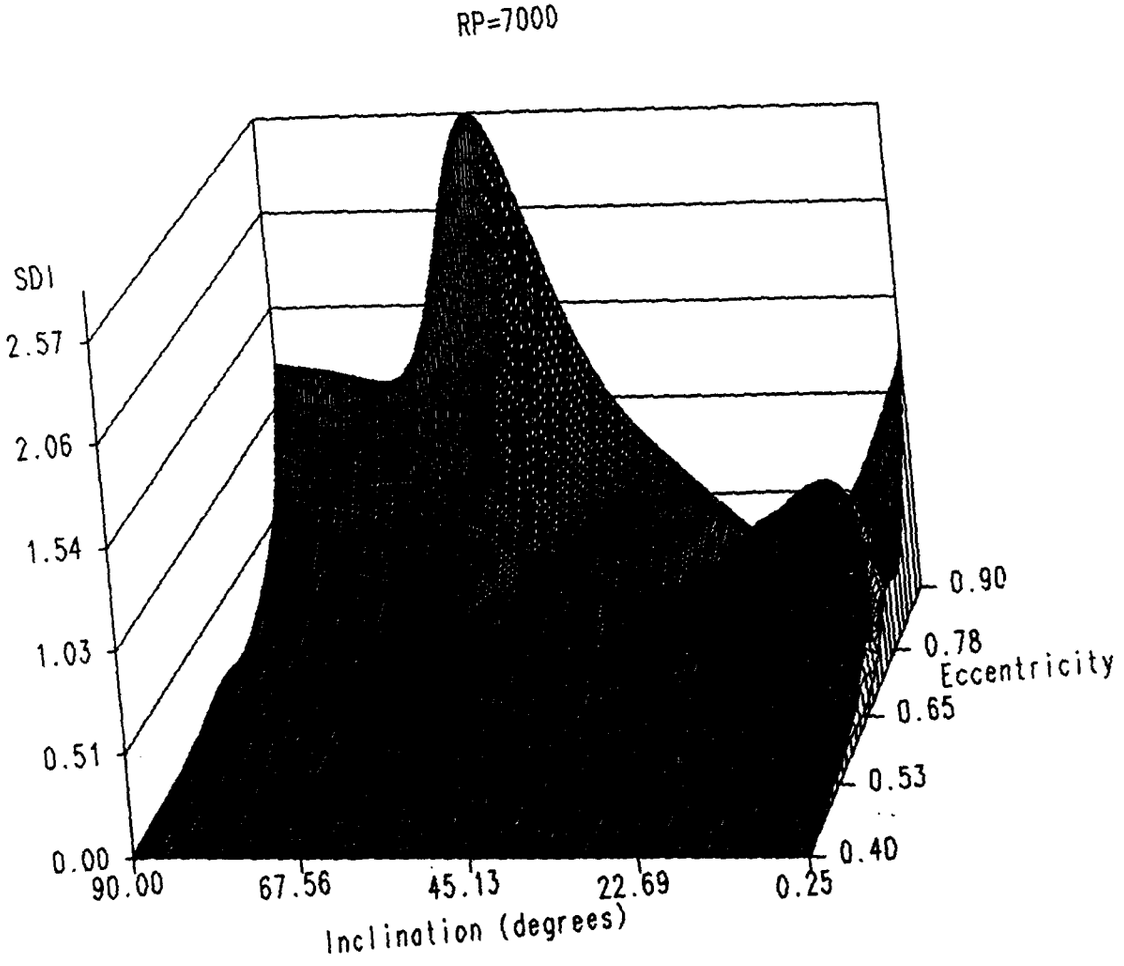

Figure 29. Standard Deviation in Inclination vs Eccentricity and Inclination : Perigee Radius=7000 km

Modeling the Locations of Critical Inclinations in Eccentricity

The locations of critical inclinations for each periapse radius considered were presented in Figures 17 through 22. The shapes of the curves are similar between periapse radii, but shifted slightly from one periapse radius to another. This section will take a closer look at the dependence of these critical inclination curves on eccentricity and periapse radius, and a curve fit will be applied to three of the curves.

The Variation of Critical Inclination Curves with Periapse Radius.

To better view the dependence of the critical inclination curves on periapse radius, Figures 30 through 35 present plots of the overlap of all similar curves (i.e., all curves labeled 'a' appear in Figure 30, all curves labeled 'b' in Figure 31, and so forth). Each set of curves is similar in shape but is shifted toward lower eccentricities as periapse radius increases. Two other features are also present.

The first is the tendency of each group of curves to converge at lower eccentricities. By inspection, curves a, b, and f converge to approximately 67.5, 64.5, and 61 degrees respectively, and curves e appear to converge to approximately 54 degrees. Curves 'c' and 'd' do not extend far enough into the lower eccentricities to estimate their convergence points. Comparing these convergence inclinations directly with the critical inclinations determined by analytical means may not be justified since the numerical search did not capture the full period of the variations. Nevertheless, curves 'a' may be compared with the 69.0 degree analytical result, curves 'b' with the 63.4 degree analytical result, and curves 'e' with the 56.1 degree analytical result.

The second feature of the critical inclination curves is the direction in which the curves diverge from the convergence points discussed above. Curves a, b, and c diverge toward increasing inclinations; curves d, e, and f diverge toward decreasing inclinations. The dividing inclination seems to be near the well known critical inclination produced by J_2 alone, namely 63.4 degrees, at which the argument of pericenter remains constant. The direction of divergence may be related to the direction of the change in the argument of pericenter.

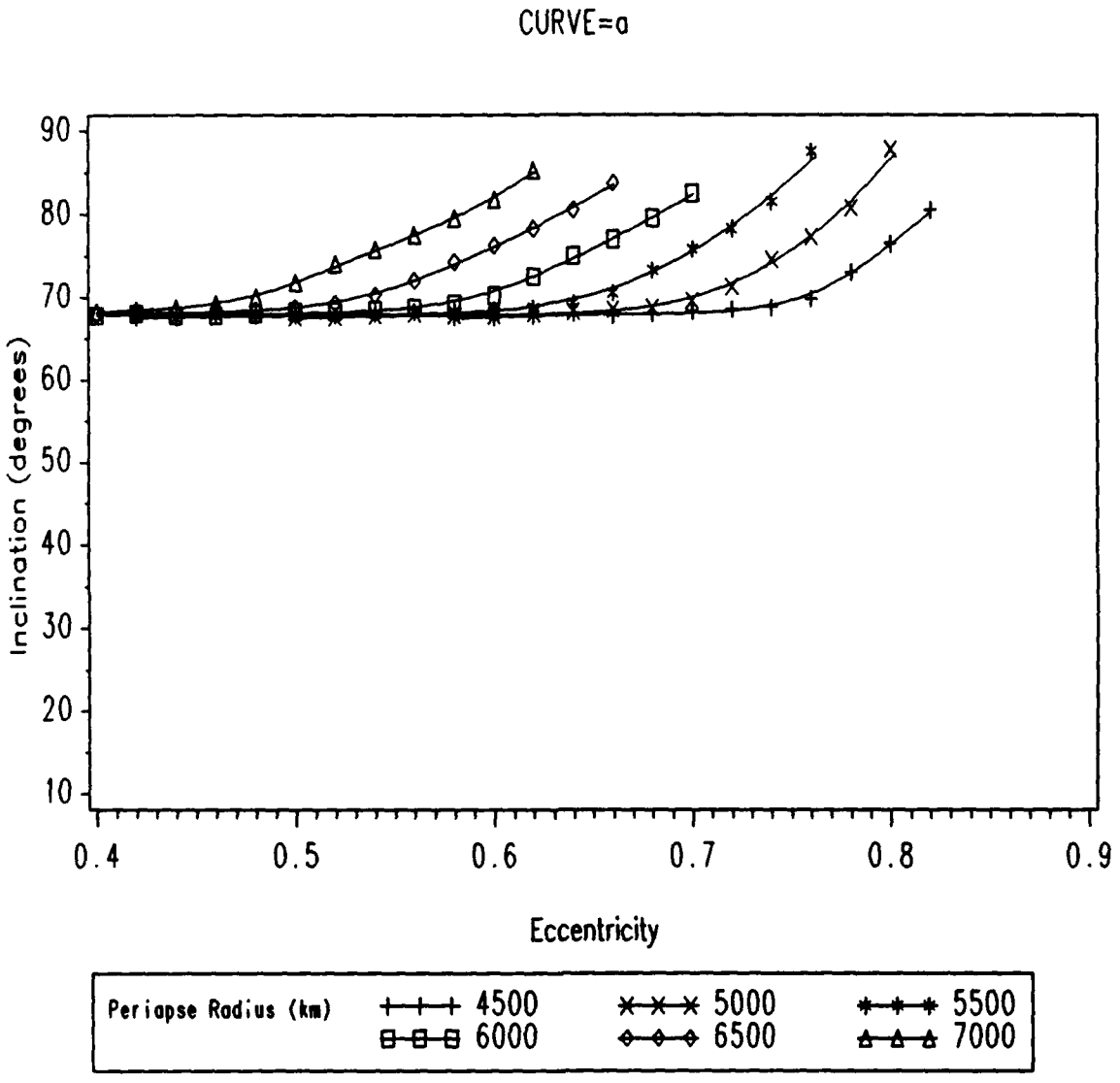

Figure 30. Critical Inclination vs Eccentricity: Curve a

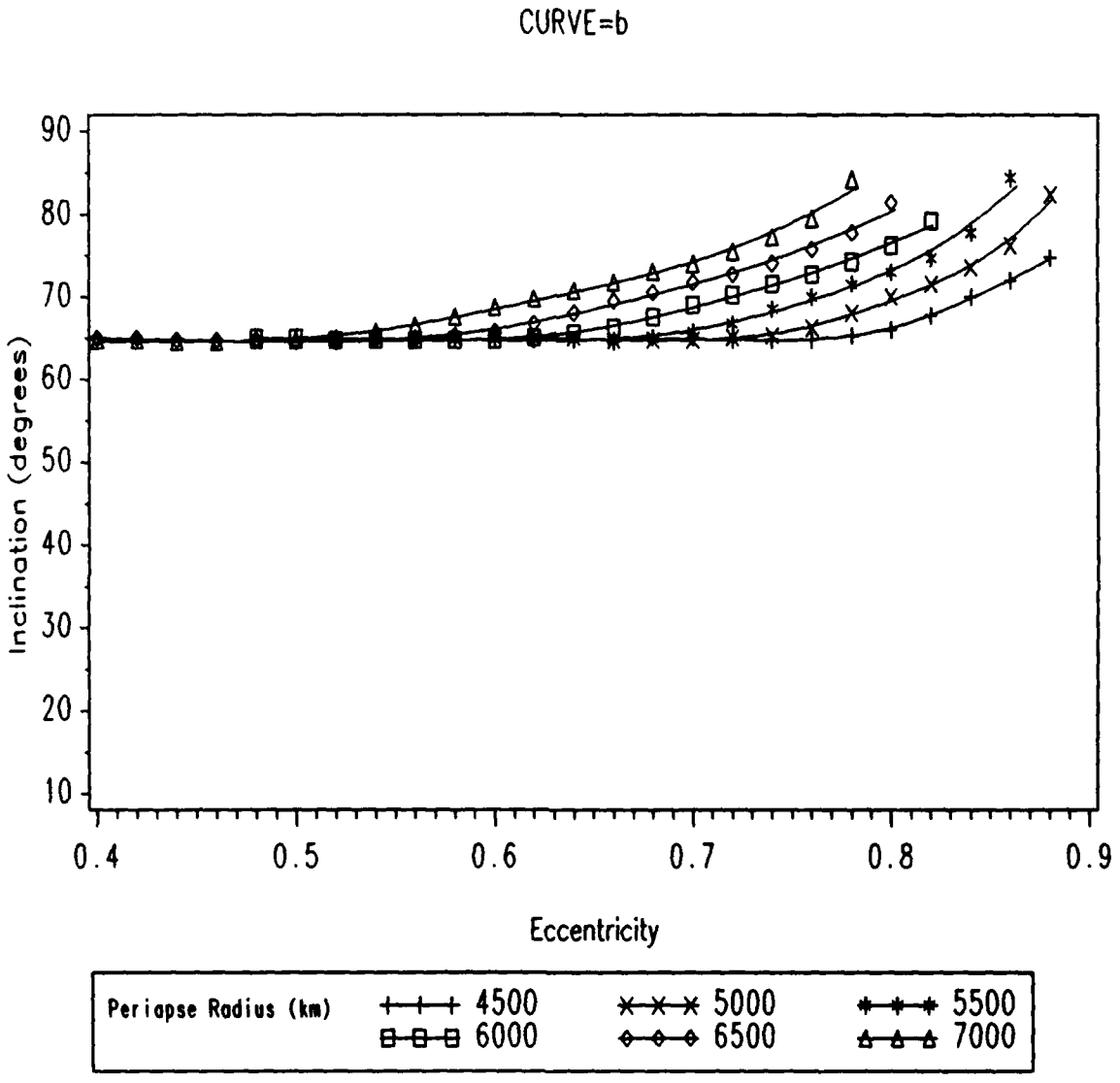

Figure 31. Critical Inclination vs Eccentricity: Curve b

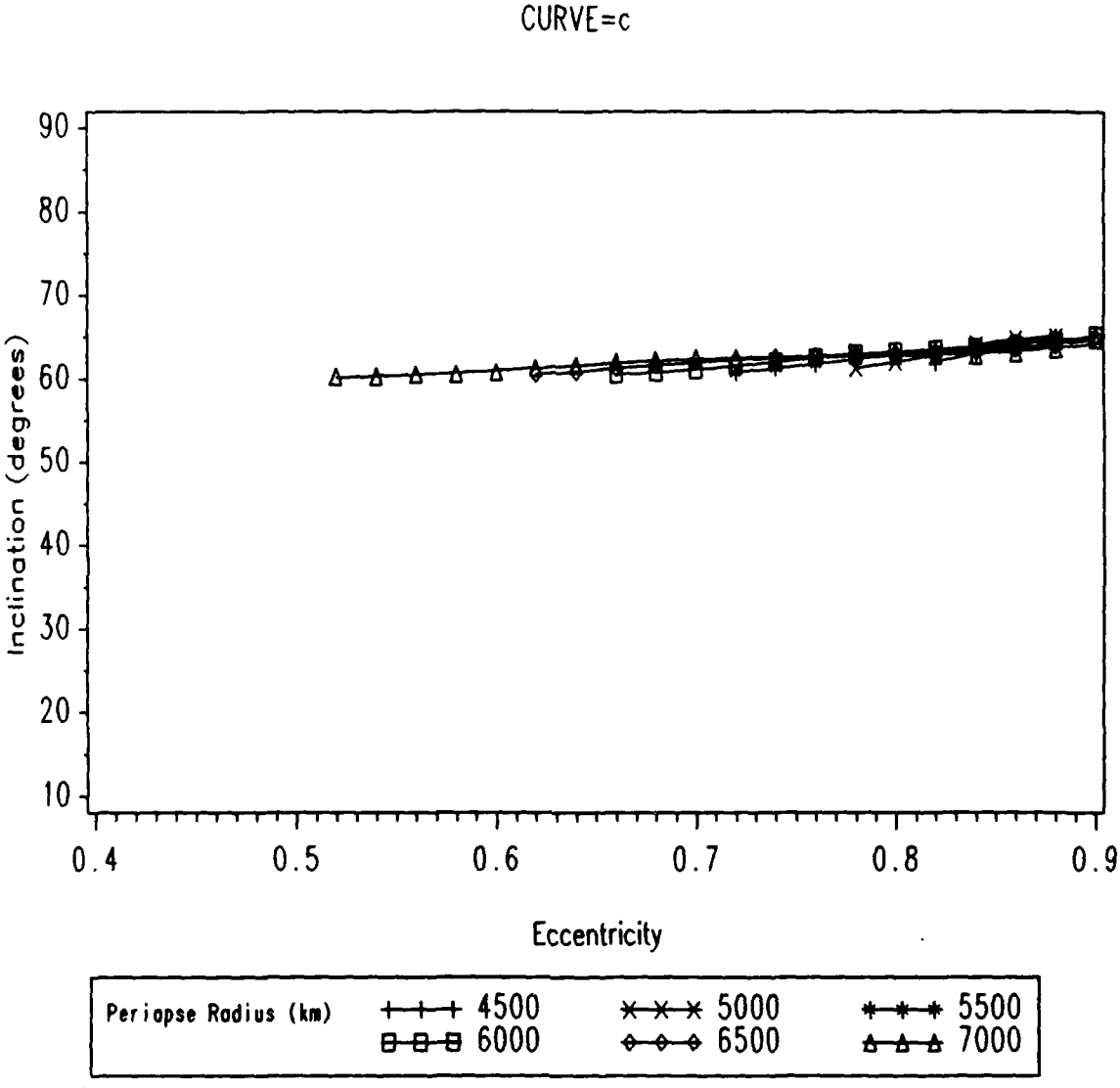

Figure 32. Critical Inclination vs Eccentricity: Curve c

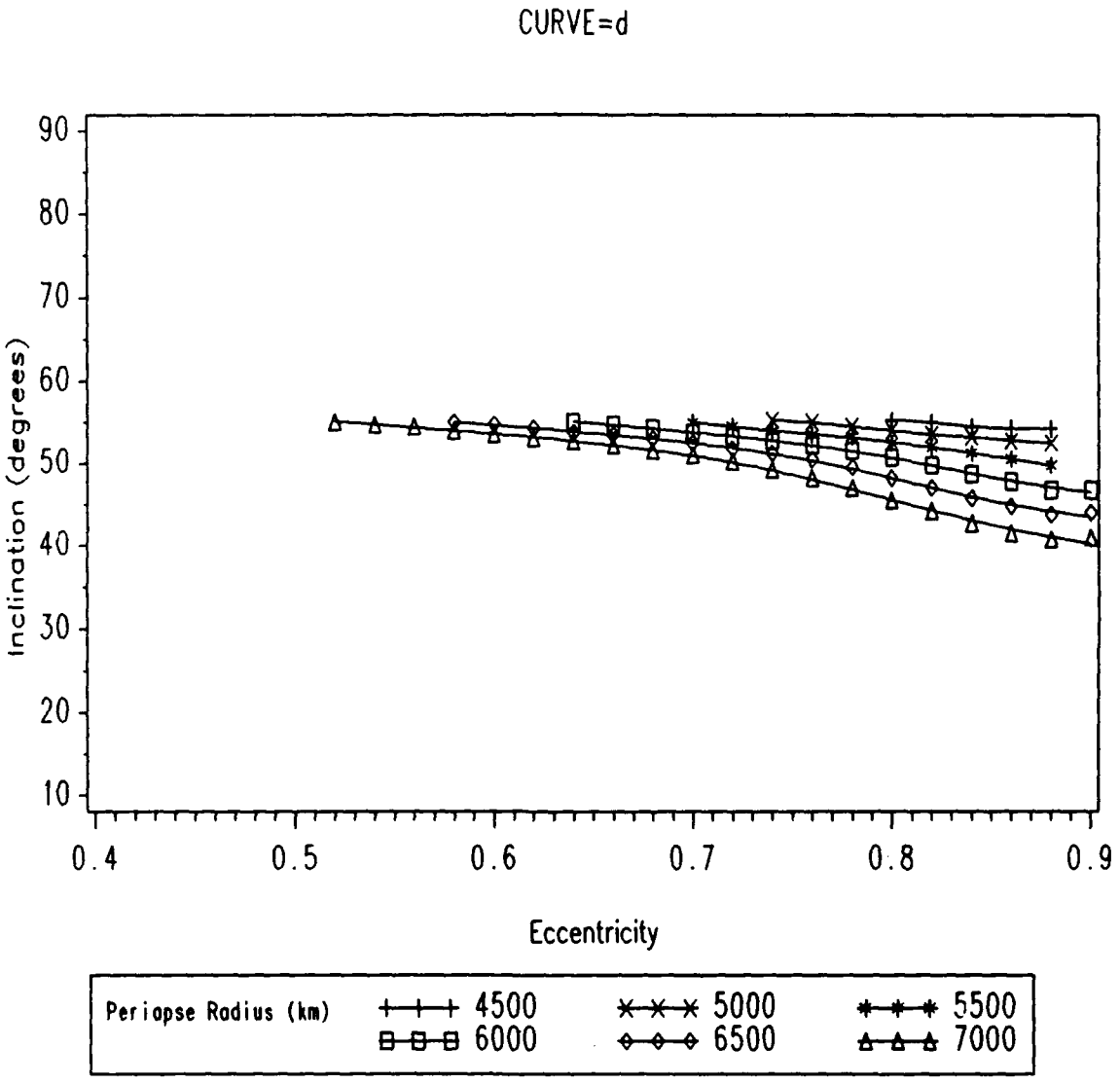

Figure 33. Critical Inclination vs Eccentricity: Curve d

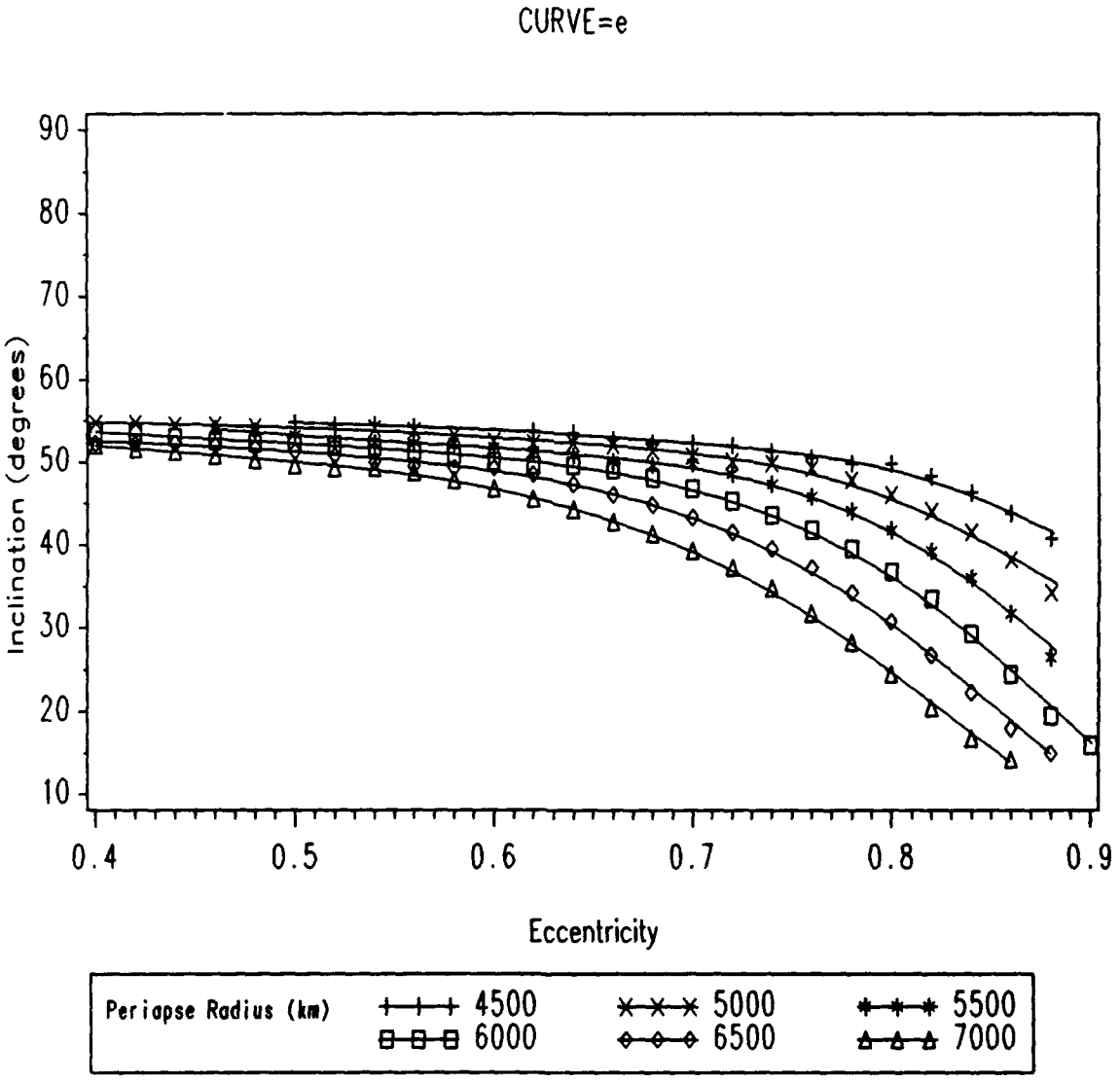

Figure 34. Critical Inclination vs Eccentricity: Curve e

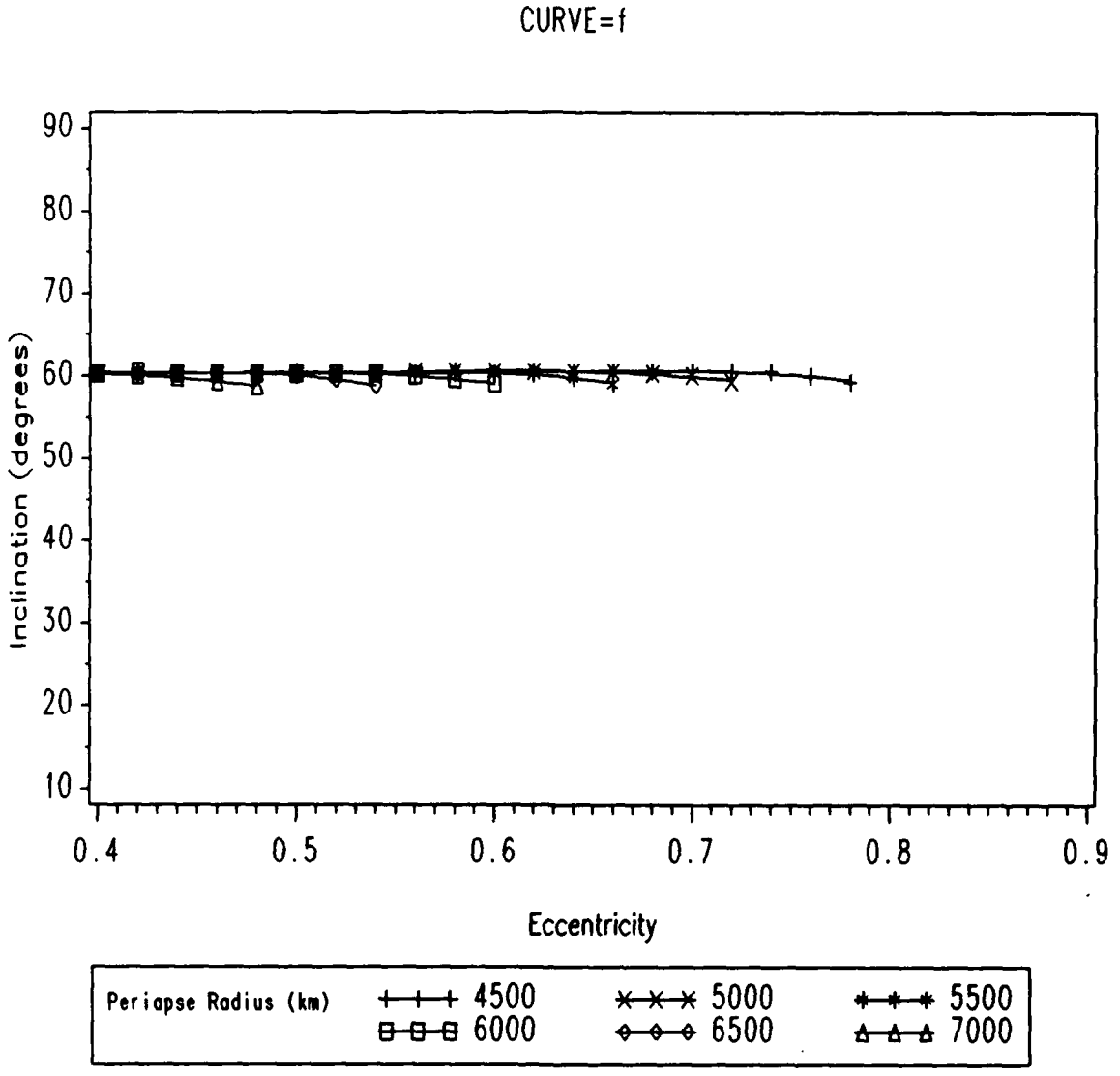

Figure 35. Critical Inclination vs Eccentricity: Curve f

Curve Fitting.

Of the six critical inclination curves plotted, curves a, b, and e best demonstrate the convergence behavior discussed above. For curves a and b, as eccentricity increases from 0.4, the critical inclination remains constant until a specific eccentricity is reached, henceforth called the departure eccentricity. Beyond the departure eccentricities, the critical inclination curves are no longer constant. Curve e exhibits the same behavior, however the departure eccentricities appear to occur below the range of data examined.

In order to apply multiple regression to curves a, b, and e, each curve must be divided into two sections. The section which lies below the departure eccentricity is simply a straight line at constant inclination. The section above the departure eccentricity is the section to be fitted (for curve e, the entire range of data will be assumed to lie above the departure eccentricity). The location of the departure eccentricities must be determined as a function of periapse radius. Since the data for each curve is discrete, the departure eccentricities for the data collected may be approximated (recall, the search increment in inclination was 0.25 degrees). Table 3 below lists the departure eccentricities for curves a and b for each periapse radius.

Table 3. Departure Eccentricities for Curves a, b, and e

	Curve a	Curve b
Periapse Radius (km)	Departure Eccentricity	
4500	0.74	0.78
5000	0.68	0.74
5500	0.62	0.70
6000	0.56	0.64
6500	0.50	0.58
7000	0.44	0.54

A linear fit to the data above yields correlation coefficients of -1.0000 and -0.997 for curves a and b respectively. The resulting functions are

$$DE_a = 1.280 - 1.20 \times 10^{-4} r_p \quad (75)$$

$$DE_b = 1.235 - 9.94 \times 10^{-5} r_p \quad (76)$$

where DE_a and DE_b are the respective departure eccentricities for curves a and b, and r_p is in kilometers.

Fitting the critical inclination curves above the departure eccentricities to a curve linear in periapse radius and quadratic in eccentricity yields the following functions:

$$i_{ca} = \begin{cases} 67.5 & e < DE_a \\ -33.9 + 0.01204 r_p + 89.403 e^2 & e \geq DE_a \end{cases}$$

$$i_{cb} = \begin{cases} 64.5 & e < DE_b \\ 0.0068443 r_p + 56.411 e^2 & e \geq DE_b \end{cases}$$

$$i_{ce} = \begin{cases} 107.72 - 0.0067837 r_p - 49.59 e^2 & e \geq 0.40 \end{cases}$$

where i_{ca} , i_{cb} , and i_{ce} are the respective critical inclination functions for curves a, b, and e. The coefficients of multiple determination (R^2) for these fits are 0.95, 0.94, and 0.86 respectively. The curve fits were accomplished using the GLM (general linear model) procedure of the SAS (Statistical Analysis System) computer package [10].

IV. Conclusions and Recommendations

Summary and Conclusions

The purpose of this thesis was to locate critical inclinations in long term high eccentricity orbits about Mars using numerical methods. The approach consisted of applying a linear least squares fit to the graphs of eccentricity versus time and inclination versus time for a range of eccentricities and inclinations. The residuals from the linear fits served as the search parameter for identifying the critical inclinations, which appeared in the form of local maximums in the three-dimensional surface plots of the standard deviation in the residuals versus e and i. The following results were obtained:

1. The numerical approach clearly identified the locations of some of the critical inclinations in eccentricity within the range searched. The presence of other critical inclinations were indicated, however the range and resolution of the search were not extensive enough for close examination of these other locations.
2. The locations of critical values for eccentricity were found to vary with eccentricity and periapse radius. Six distinct critical location curves were identified, three of which were curve fit to functions linear in periapse radius and quadratic in eccentricity.
3. These three curves converge to three critical inclinations determined by analytical results to within the search increments used. The remaining curves did not include enough data for direct comparison with analytical results.
4. Critical values for inclination were not clearly identified. Three dimensional surface plots of the standard deviation in the residuals for inclination produced one or two dominant local maximums.
5. For the range and resolution of data collected, no evidence of correlation between critical values for eccentricity and critical values for inclination was found.

Based on these results, a high eccentricity orbit about Mars may be utilized to meet specific satellite mission requirements, or to reduce orbit insertion costs, provided

care is taken to avoid critical inclinations which produce unacceptable variations. This investigation demonstrated a numerical procedure for identifying the conditions for which such variations occur.

Recommendations for Further Study

The presence of constraints within any form of research automatically provides opportunities for further study when the contraints are removed. The work presented here could be repeated using much finer search increments, and more importantly, longer orbit lifetimes. Capturing at least one full period of the variations in eccentricity and inclination may provide for a much more detailed analysis, as well as a more complete comparison with analytical results. Under these more favorable conditions, the following additional studies might also be accomplished:

1. Attempt to determine low eccentricity convergence points for all critical inclination curves identified.
2. Determine not only the location of the critical inclinations but also the magnitudes and periods of the variations.
3. Extend the search range to 180 degrees inclination. The work accomplished in this investigation produced no evidence of symmetry about 90 degrees inclination.
4. Include the effects of additional harmonics in the Mars gravity potential.
5. Investigate the effects of varying the arguments of periapse and ascending node at orbit insertion.

Appendix A. *Hansen's Coefficients*

For a complete derivation of Hansen's Coefficients, see [2]. This appendix provides a brief definition, as well as the derivation of Eqs (14), (17), and (18), and Eqs (45), (46), and (47).

Definition of Hansen's Coefficient

Let

$$x = \exp(jf), \quad y = \exp(jE), \quad z = \exp(jM)$$

where f is the true anomaly, E is the eccentric anomaly, M is the mean anomoly, and $j = \sqrt{-1}$. Hansen's Coefficients are then defined

$$X_p^{n,m} = \frac{1}{2\pi} \int_0^{2\pi} \left(\frac{r}{a}\right)^n x^m z^{-p}\, dM \tag{77}$$

For $p = 0$:

$$X_0^{n,m} = \left(-\frac{e}{2}\right)^{|m|} \begin{pmatrix} n+|m|+1 \\ |m| \end{pmatrix} F\left(\frac{|m|-n-1}{2}, \frac{|m|-n}{2}; |m|+1; e^2\right) \tag{78}$$

where F is the hypergeometric function [1:272-277] defined as

$$F(a, b; c; y) = \sum_{n=0}^{\infty} \frac{(a)_n (b)_n}{(c)_n} \frac{y^n}{n!}, \quad |y| < 1$$

The abbreviation $(a)_n$, which is called the *Pochhammer symbol*, has the following properties:

$$(a)_0 = 1$$

$$(1)_n = n!$$

$$(a)_n = a(a+1)(a+2)\cdots(a+n-1) \qquad n = 1, 2, 3, \ldots$$

The *Pochhammer symbol* and the *binomial coefficient* are related by

$$(a)_n = (-1)^n\, n! \begin{pmatrix} -a \\ n \end{pmatrix}$$

The following property of Hansen's Coefficients will be used below:

$$X_0^{m,n} = X_0^{m,-n} \tag{79}$$

Derivations

Derivation of Eq (14):

$$\begin{aligned}
\frac{1}{2\pi}\int_0^{2\pi}\left(\frac{r}{a}\right)^{-3} dM &= X_0^{-3,0} \\
&= \left(-\frac{e}{2}\right)^0 \binom{-2}{0} F\left(1, \frac{3}{2}; 1; e^2\right) \\
&= (1)(1)\sum_{n=0}^{\infty} \frac{(1)_n \left(\frac{3}{2}\right)_n}{(1)_n} \frac{e^{2n}}{n!} \\
&= \sum_{n=0}^{\infty} n! \binom{-3/2}{n} (-1)^n \frac{e^{2n}}{n!} \\
&= \sum_{n=0}^{\infty} \binom{-\frac{3}{2}}{n} \left(-e^2\right)^n
\end{aligned}$$

The last expression is simply the binomial expansion for $(1-e^2)^{-3/2}$, so

$$X_0^{-3,0} = \left(1-e^2\right)^{-3/2} \tag{80}$$

Derivation of Eq (17):

Using the identity

$$\sin 2f = \frac{1}{2j}\left[\exp(j2f) - \exp(-j2f)\right] \tag{81}$$

then

$$\frac{1}{2\pi}\int_0^{2\pi}\left(\frac{r}{a}\right)^{-3} \sin 2f \, dM$$

$$\begin{aligned}
&= \frac{1}{2\pi}\int_0^{2\pi}\left(\frac{r}{a}\right)^{-3} \frac{1}{2j}\left[\exp(j2f) - \exp(-j2f)\right] dM \\
&= \frac{1}{2j}\left[\frac{1}{2\pi}\int_0^{2\pi}\left(\frac{r}{a}\right)^{-3} \exp(j2f)\, dM - \frac{1}{2\pi}\int_0^{2\pi}\left(\frac{r}{a}\right)^{-3} \exp(-j2f)\, dM\right] \\
&= \frac{1}{2j}\left(X_0^{-3,2} - X_0^{-3,-2}\right) = 0
\end{aligned} \tag{82}$$

because of Eq (79).

Derivation of Eq (18):

Using the identity

$$\cos 2f = \frac{1}{2}\left[\exp(j2f) + \exp(-j2f)\right] \tag{83}$$

then

$$\frac{1}{2\pi}\int_0^{2\pi}\left(\frac{r}{a}\right)^{-3}\cos 2f\, dM$$

$$\begin{aligned}
&= \frac{1}{2\pi}\int_0^{2\pi}\left(\frac{r}{a}\right)^{-3}\frac{1}{2}\left[\exp(j2f)+\exp(-j2f)\right] dM \\
&= \frac{1}{2}\left[\frac{1}{2\pi}\int_0^{2\pi}\left(\frac{r}{a}\right)^{-3}\exp(j2f)\, dM + \frac{1}{2\pi}\int_0^{2\pi}\left(\frac{r}{a}\right)^{-3}\exp(-j2f)\, dM\right] \\
&= \frac{1}{2}\left(X_0^{-3,2} + X_0^{-3,2}\right) = X_0^{-3,2}
\end{aligned} \tag{84}$$

$$X_0^{-3,2} = \left(-\frac{e}{2}\right)^2 \binom{0}{2} F\left(2\,,\,\frac{5}{2}\,;\,3\,;\,e^2\right) = 0 \tag{85}$$

Derivation of Eq (45)

$$\frac{1}{2\pi}\int_0^{2\pi}\left(\frac{r}{a}\right)^{2}\cos 2f\, dM$$

$$\begin{aligned}
&= \frac{1}{2\pi}\int_0^{2\pi}\left(\frac{r}{a}\right)^{2}\frac{1}{2}\left[\exp(j2f)+\exp(-j2f)\right] dM \\
&= \frac{1}{2}\left[\frac{1}{2\pi}\int_0^{2\pi}\left(\frac{r}{a}\right)^{2}\exp(j2f)\, dM + \frac{1}{2\pi}\int_0^{2\pi}\left(\frac{r}{a}\right)^{2}\exp(-j2f)\, dM\right] \\
&= \frac{1}{2}\left(X_0^{2,2} + X_0^{2,2}\right) = X_0^{2,2}
\end{aligned} \tag{86}$$

$$\begin{aligned}
X_0^{2,2} &= \left(-\frac{e}{2}\right)^2 \binom{5}{2} F\left(-\frac{1}{2}\,,\,0\,;\,3\,;\,e^2\right) \\
&= \left(\frac{e^2}{4}\right)(10)(1) \\
&= \frac{5e^2}{2}
\end{aligned} \tag{87}$$

Derivation of Eq (46)

$$\frac{1}{2\pi}\int_0^{2\pi}\left(\frac{r}{a}\right)^2 \sin 2f\, dM$$

$$\begin{aligned}
&= \frac{1}{2\pi}\int_0^{2\pi}\left(\frac{r}{a}\right)^2 \frac{1}{2j}\left[\exp(j2f) - \exp(-j2f)\right] dM \\
&= \frac{1}{2j}\left[\frac{1}{2\pi}\int_0^{2\pi}\left(\frac{r}{a}\right)^2 \exp(j2f)\, dM - \frac{1}{2\pi}\int_0^{2\pi}\left(\frac{r}{a}\right)^2 \exp(-j2f)\, dM\right] \\
&= \frac{1}{2j}\left(X_0^{2,2} - X_0^{2,-2}\right) = 0
\end{aligned} \tag{88}$$

Derivation of Eq (47)

$$\begin{aligned}
\frac{1}{2\pi}\int_0^{2\pi}\left(\frac{r}{a}\right)^2 dM &= X_0^{2,0} \\
&= \left(-\frac{e}{2}\right)^0 \begin{pmatrix} 3 \\ 0 \end{pmatrix} F\left(-\frac{3}{2}\,;\,-1\,;\,1\,;\,e^2\right) \\
&= (1)(1)\sum_{n=0}^{\infty} \frac{\left(-\frac{3}{2}\right)_n (-1)_n}{(1)_n}\frac{e^{2n}}{n!} \\
&= 1 + \frac{3}{2}e^2
\end{aligned} \tag{89}$$

Appendix B. *Sample Program Input File*

This appendix includes the program input file for the numerical integrator (this information is included to provide consistency should further analysis be performed). Only A (a), E (e), and I (i) were changed for each computer run. All other parameters remained constant. For an explanation of the parameters listed, see [8].

```
2                                   L
0                                   M
1                                   ISUN
0                                   IMOON
0                                   IEPHEM
0                                   IDRAG
0                                   ISRP
0                                   IORB
0                                   IPRINT
1                                   IPLOT
1                                   NP
1                                   NQ
0                                   IQMAX
0                                   NK
0                                   ICASE
0                                   LSUN
0                                   NSUN(1)
0                                       (2)
0                                       (3)
0                                       (4)
0                                       (5)
0                                       (6)
0                                       (7)
0                                       (8)
0                                       (9)
0                                   LMOON
0                                   NMOON(1)
0                                        (2)
0                                        (3)
0                                        (4)
0                                        (5)
0                                        (6)
0                                        (7)
0                                        (8)
0                                        (9)
4                                   NSEG1
4                                   NSEG2
                  70000.D0          ORB(1), A
```

```
                0.9D0          (2), E
               40.75D0         (3), I
                 0.D0          (4), NODE
                 0.D0          (5), W
                 0.D0          (6), M
                1.D-6          RELERR
                1.D-6          ABSERR
               100.D0          STEP
          19911007.D0          TINT(1)
                 0.D0              (2)
          20011007.D0          TFIN(1)
                 0.D0              (2)
          19911007.D0          TREF(1)
                 0.D0              (2)
         4.2828287D4           GE
            3397.2D0           RE
     4.061249803D-3            RATE
          333.55971D0          PM
              .1017D0          ELLIP
            3487.2D0           RATM
                6.D-4          RDENS
              361.D0           RHT
               36.D0           SHT
             1000.D0           ALTMAX
               10.D-6          AREAD
               20.D-6          AREAS
             1000.D0           SCMASS
                2.D0           CDRAG
             1.95D-3           CSRP
       .13271244D12            GS
        227.9410D6             ES(1)
       93.39697D-3             ES(2)
       25.191153D0             ES(3)
                0.D0           ES(4)
         -109.0506D0           ES(5)
        171.60476D0            ES(6)
    6.065196184D-6             ES(7)
                0.D0           GM
                0.D0           EM(1)
                0.D0           EM(2)
                0.D0           EM(3)
                0.D0           EM(4)
                0.D0           EM(5)
                0.D0           EM(6)
                0.D0           EM(7)
```

```
2    0        -0.1960387250000000E-02          0.0000000000000000E+00
```

Appendix C. *Linear Least Squares Fit for Eccentricity and Inclination*

Linear fits to the curves of eccentricity versus time and inclination versus time allowed for using the standard deviation of the residuals as the search parameter for locating critical inclinations. In the standard notation, x is the independent variable, y is the dependent variable, and ε is the residual (13:23-47), so that

$$y_i = \beta_0 + \beta_1 x_i + \epsilon_i \tag{90}$$

where the subscript i refers to the ith observation or data point. The coefficients are determined by

$$\beta_1 = \frac{\sum x_i y_i - \frac{(\sum x_i)(\sum y_i)}{n}}{\sum x_i^2 - \frac{(\sum x_i)^2}{n}} \tag{91}$$

$$\beta_0 = \frac{1}{n}\left(\sum y_i - \beta_1 \sum x_i\right) \tag{92}$$

where n is the number of data points. The error mean square (MSE) of the residuals is given by

$$MSE = \frac{\sum (y_i - \beta_0 - \beta_1 x_i)^2}{n-2} = \frac{\sum \epsilon_i^2}{n-2} \tag{93}$$

The estimator of the standard deviation of the residuals is simply the positive square root of MSE.

A FORTRAN program was written to calculate the standard deviations. The program reads data from the numerical integrator output file, calculates the standard deviation of the residuals to the linear fit in eccentricity and inclination for each orbit run, then outputs the standard deviations to a new file. Three-dimensional surface plots were created using the data from this new file.

The program includes a provision for computer runs which ended prematurely. If the radius of periapse became equal to or less than the planet radius due to a large variation in eccentricity, an impact occured and the run was terminated. In order to use the standard deviation as a search parameter for critical inclinations, each run must have the same (or nearly the same) number of data points. Significantly shorter runs were rejected, runs which were only a few days shorter were kept. The shorter runs appear as discontinuities at the edges of the surface plots.

Appendix D. *Plots of SDE and SDI versus Inclination for* $r_p = 6500km$

This appendix includes all the plots of Standard Deviation in Eccentricity (SDE) and Standard Deviation in Inclination (SDI) versus Inclination for a periapse radius of 6500km. The plots of SDE and SDI are overlayed for the purpose of comparison. Each vertical axis is relatively scaled.

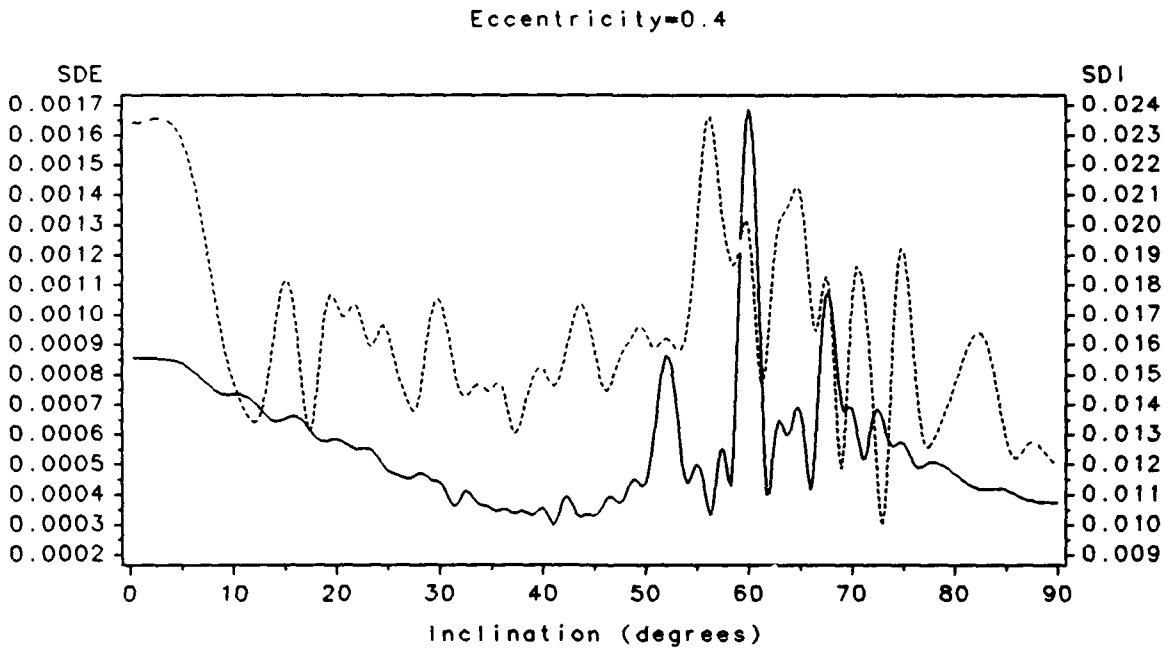

Figure 36. SDE and SDI (dashed) vs Inclination

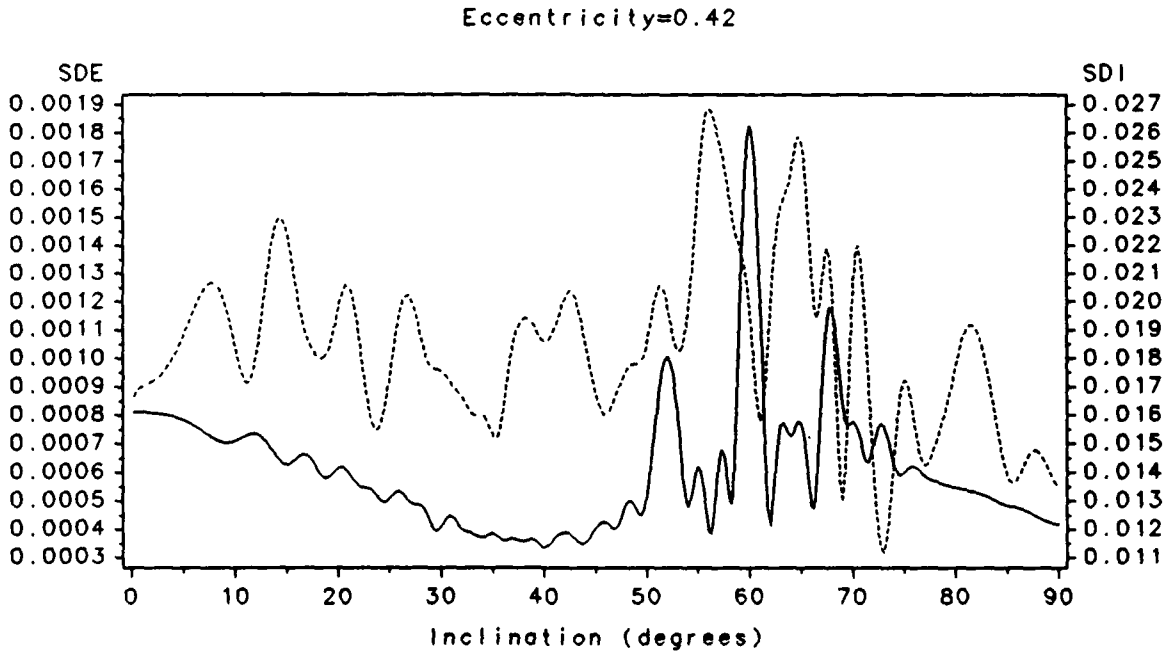

Figure 37. SDE and SDI (dashed) vs Inclination

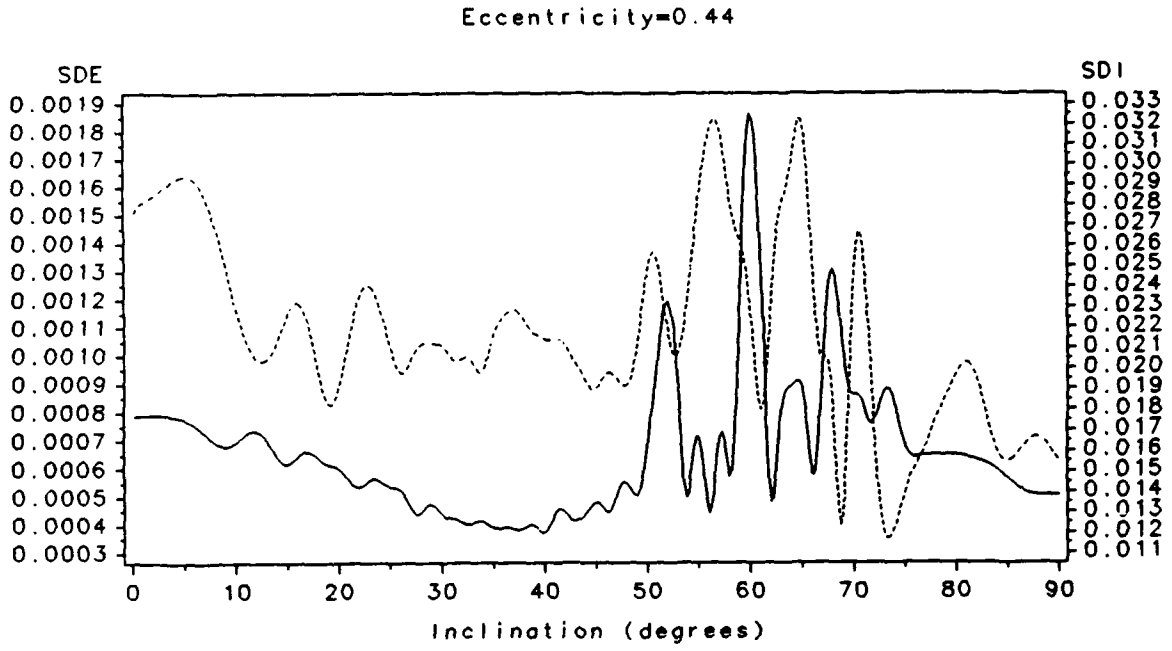

Figure 38. SDE and SDI (dashed) vs Inclination

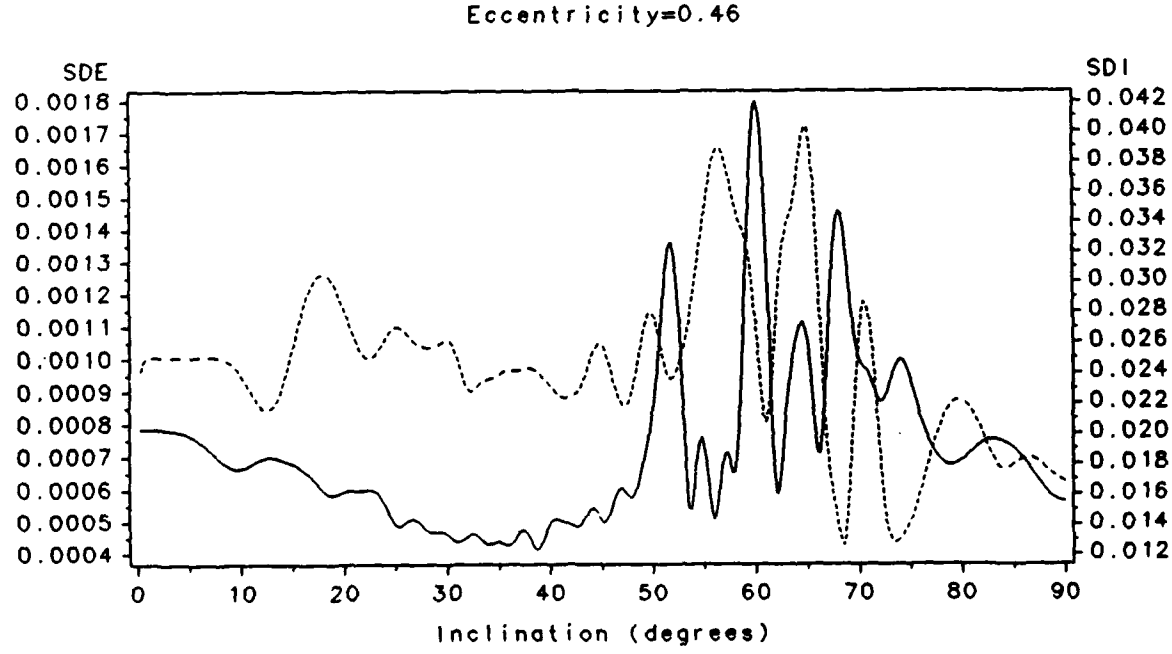

Figure 39. SDE and SDI (dashed) vs Inclination

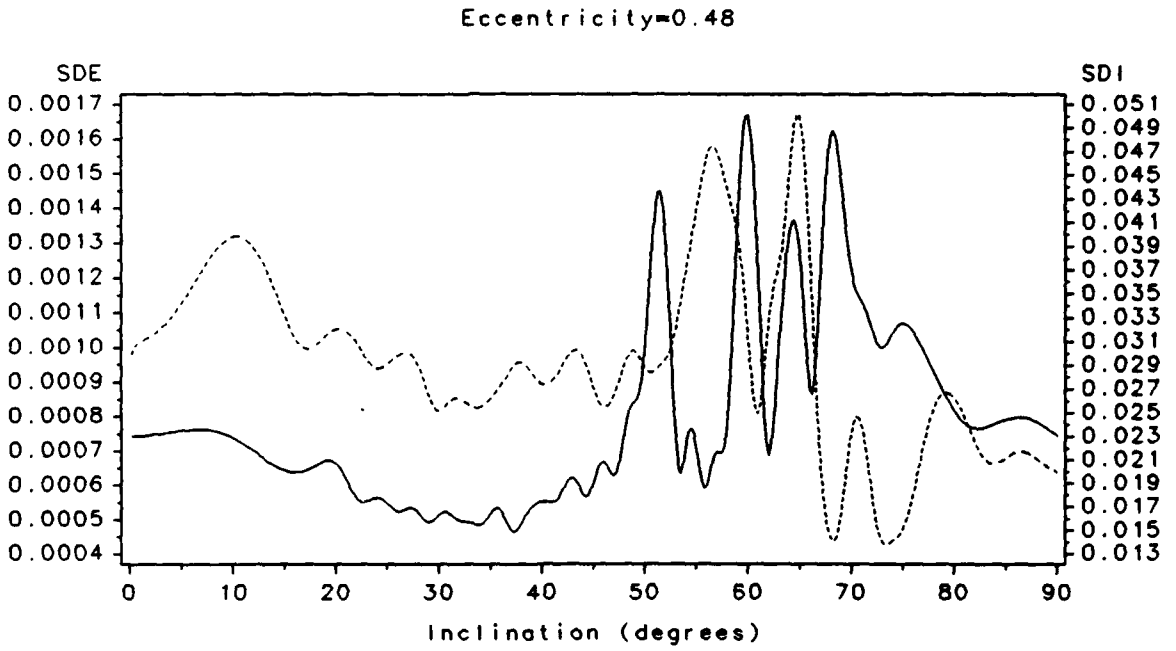

Figure 40. SDE and SDI (dashed) vs Inclination

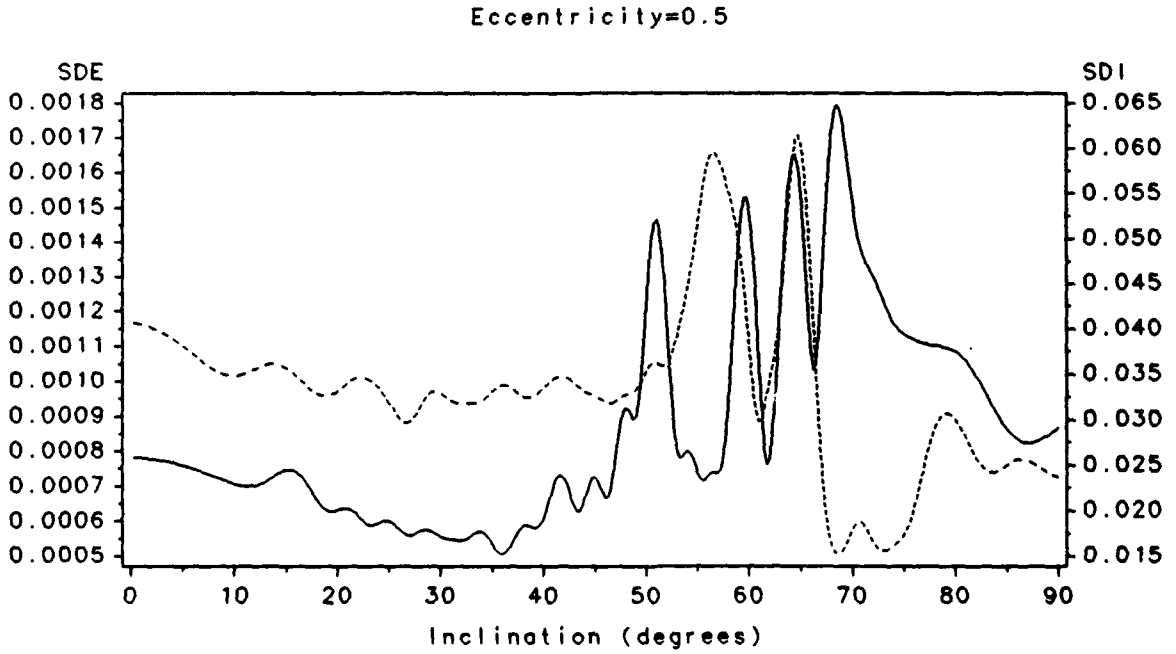

Figure 41. SDE and SDI (dashed) vs Inclination

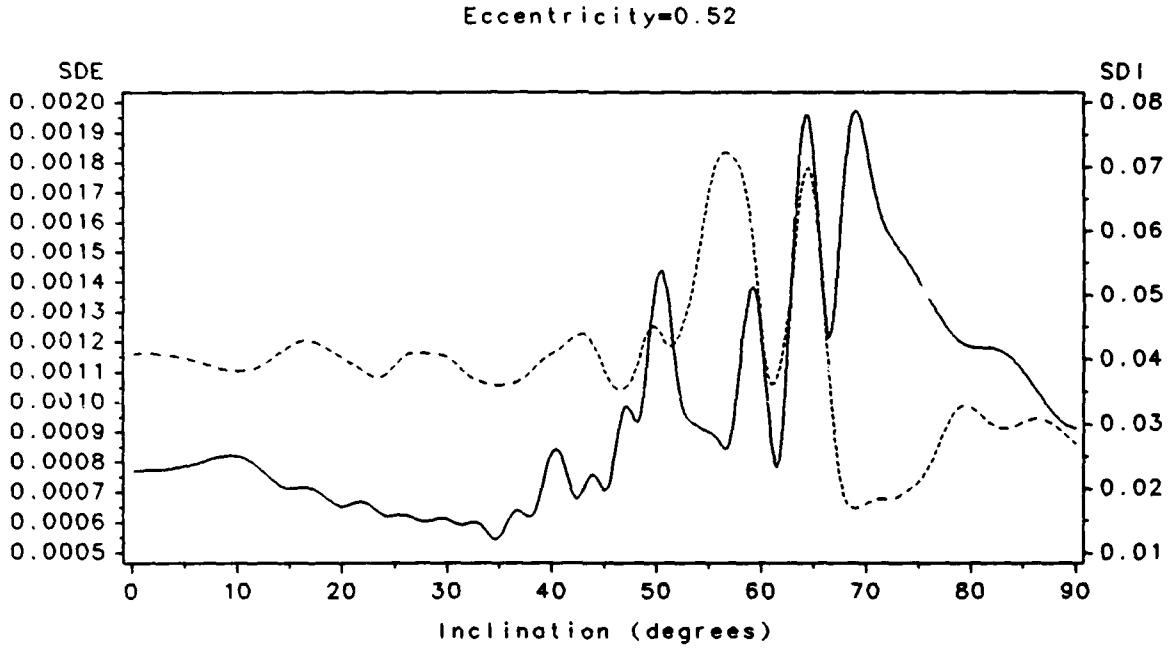

Figure 42. SDE and SDI (dashed) vs Inclination

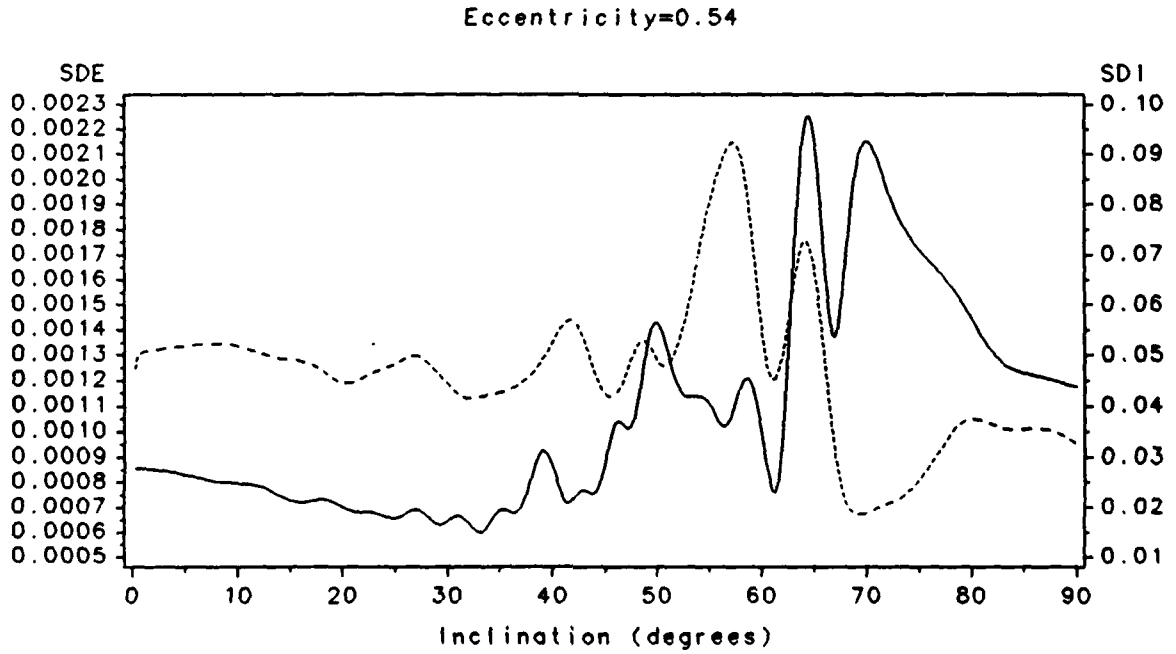

Figure 43. SDE and SDI (dashed) vs Inclination

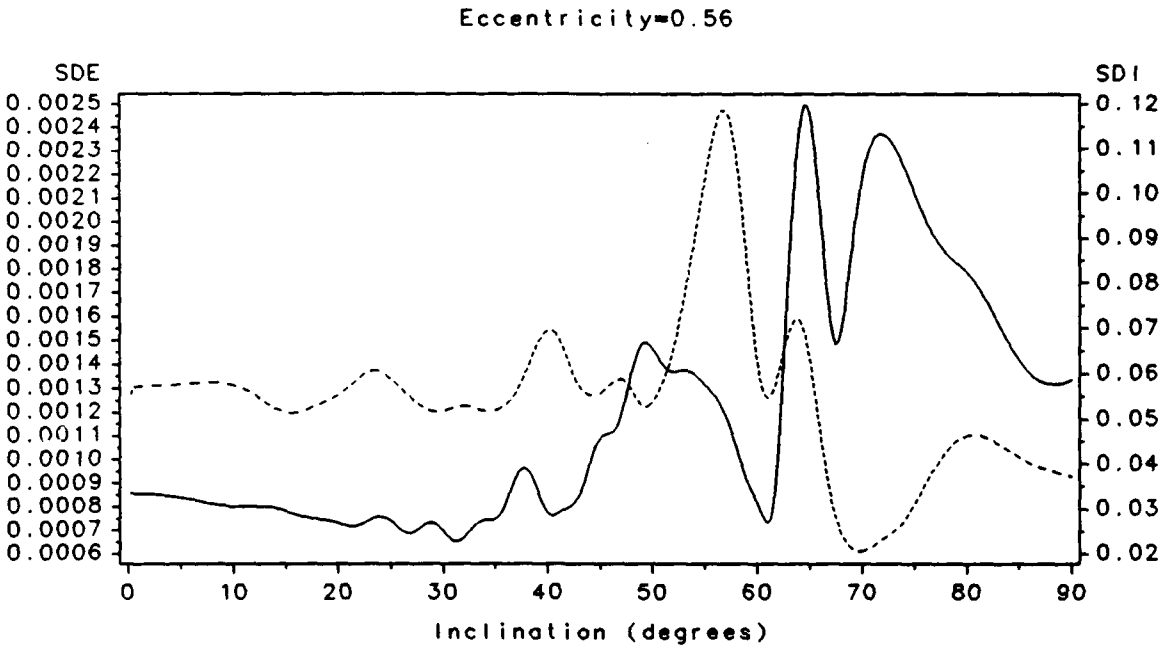

Figure 44. SDE and SDI (dashed) vs Inclination

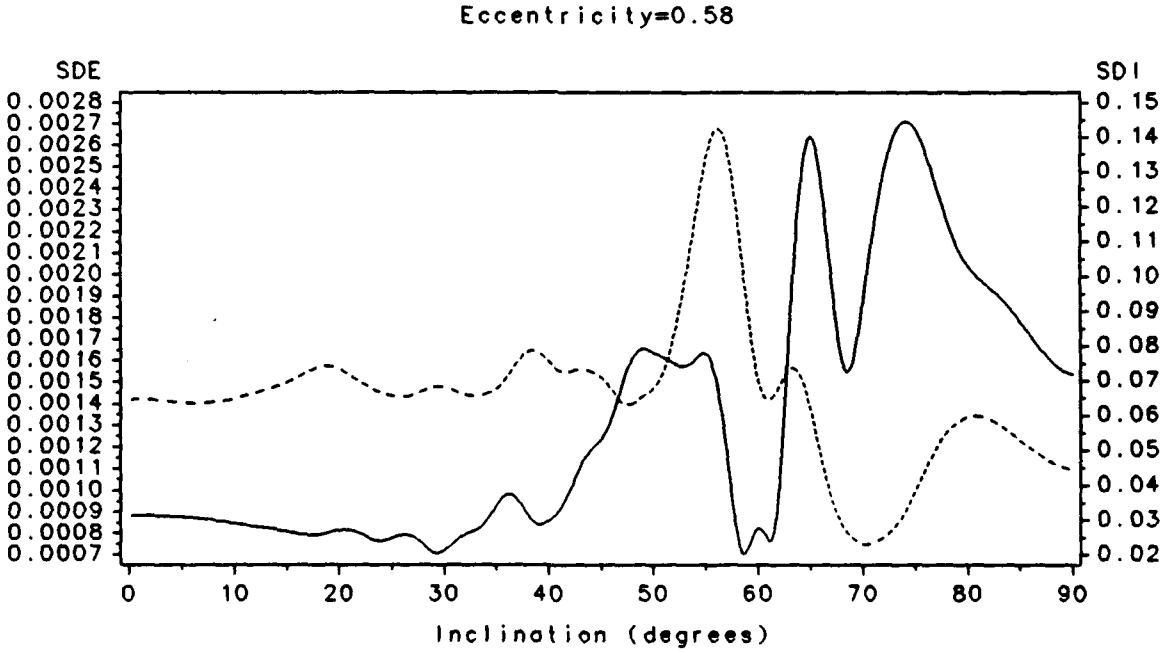

Figure 45. SDE and SDI (dashed) vs Inclination

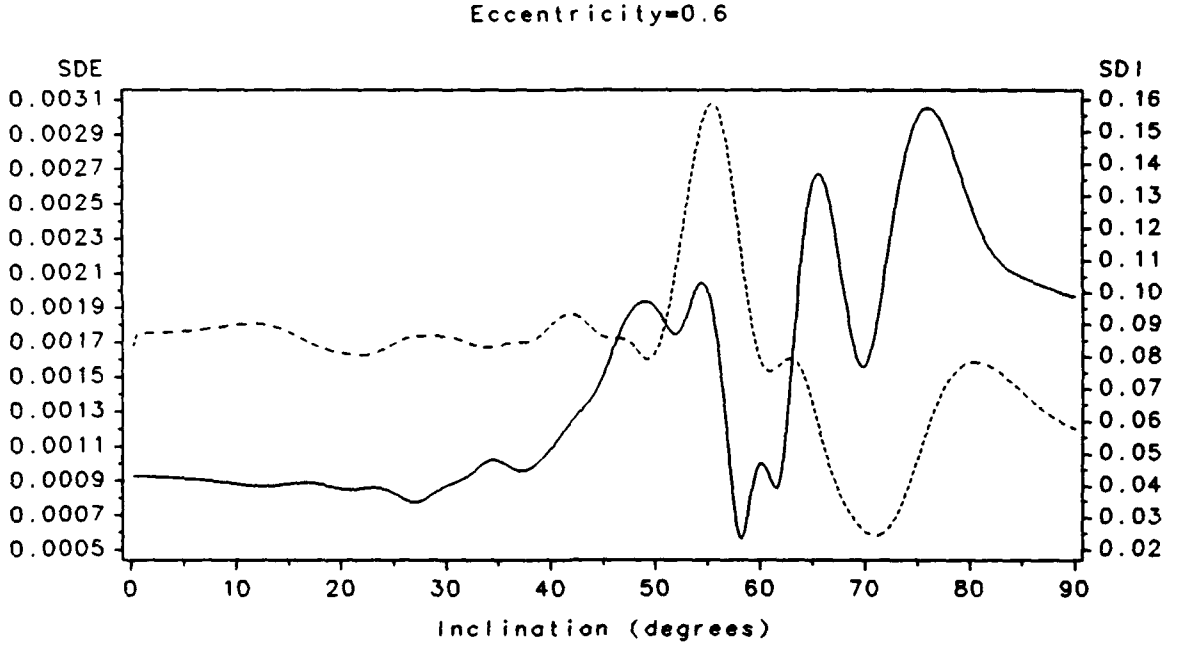

Figure 46. SDE and SDI (dashed) vs Inclination

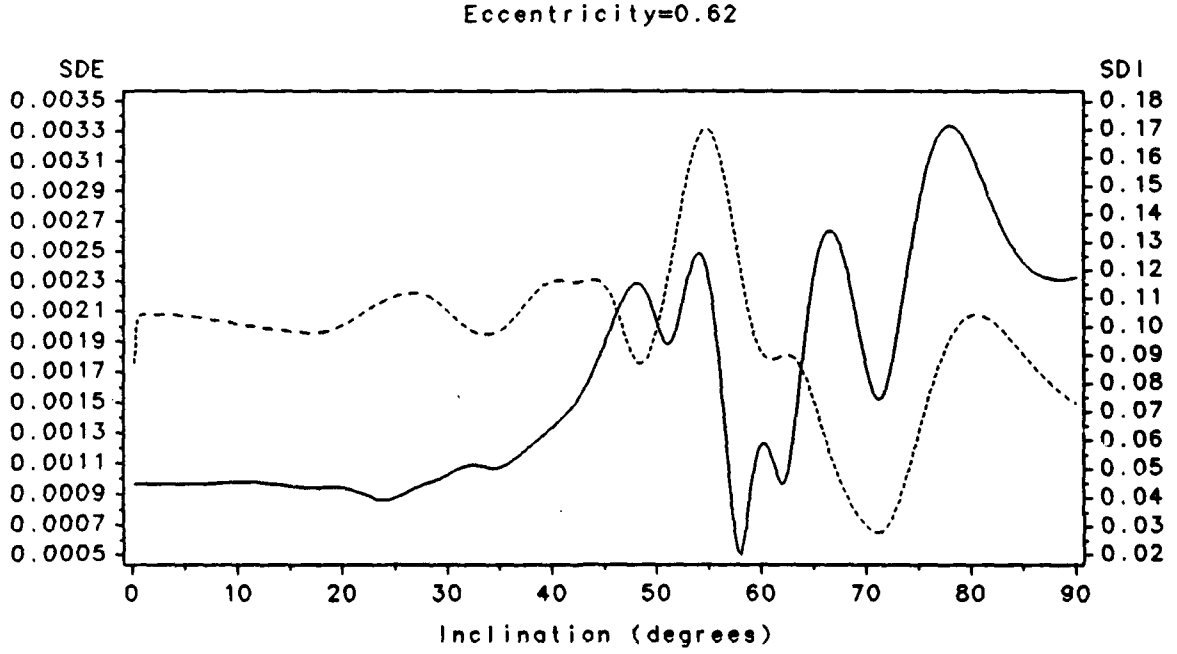

Figure 47. SDE and SDI (dashed) vs Inclination

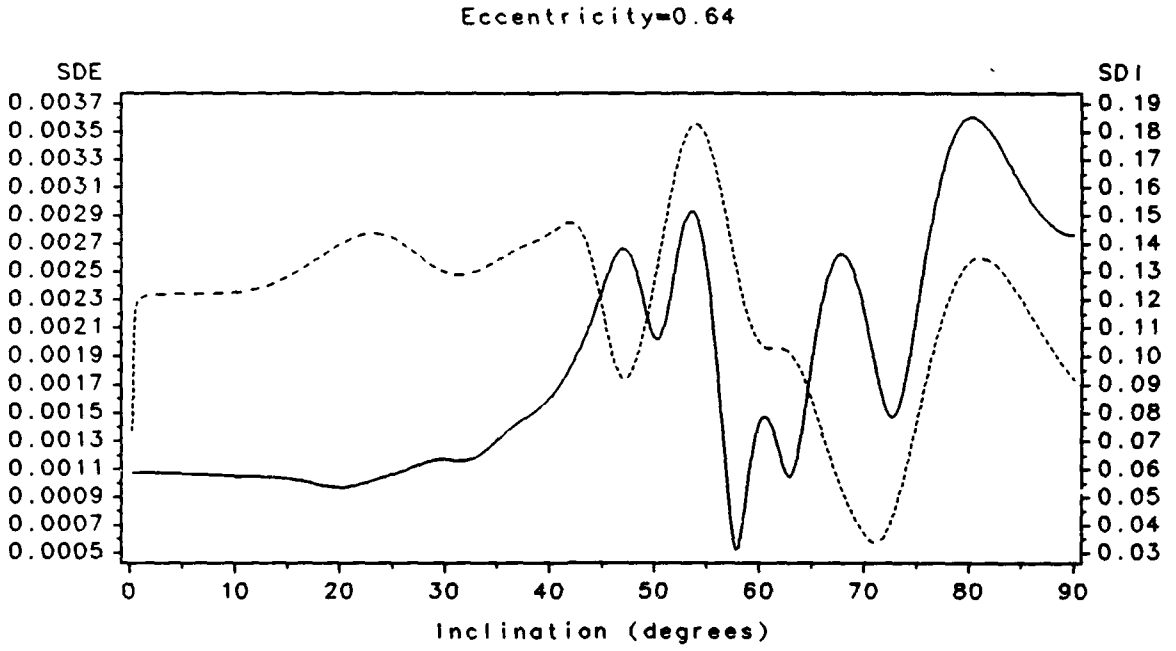

Figure 48. SDE and SDI (dashed) vs Inclination

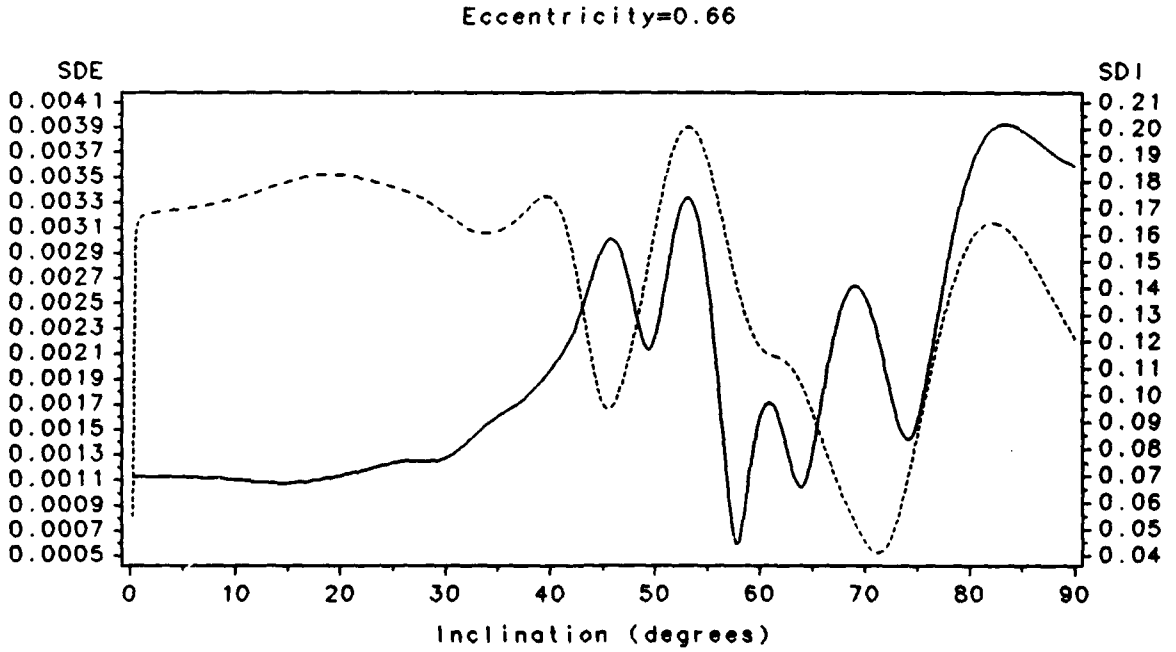

Figure 49. SDE and SDI (dashed) vs Inclination

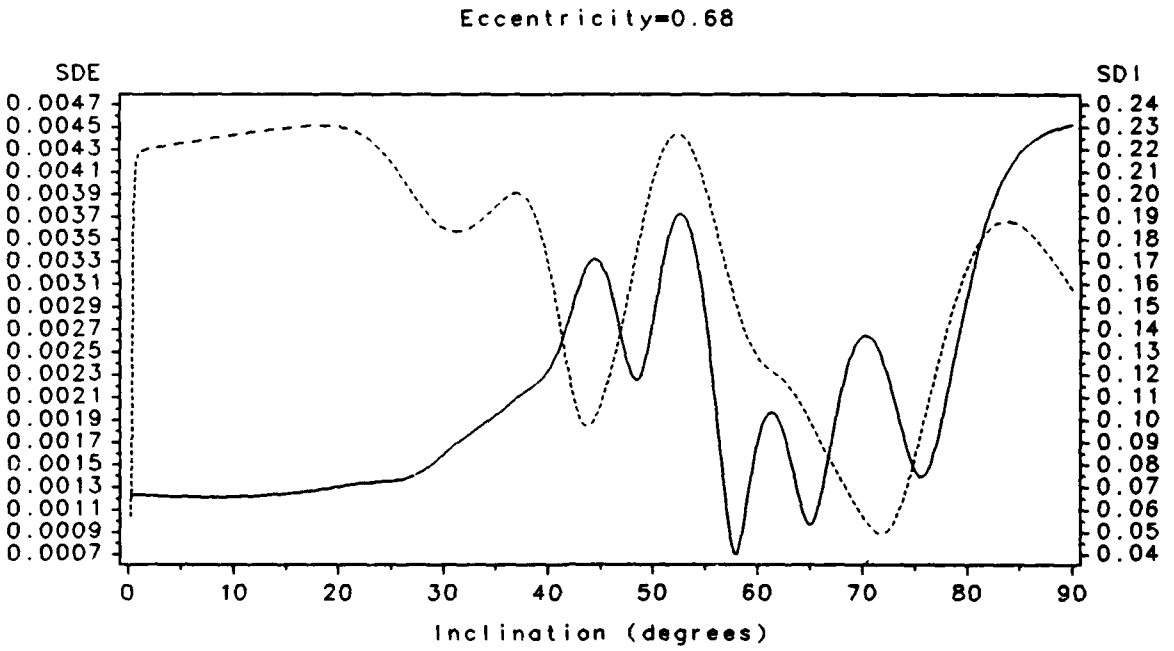

Figure 50. SDE and SDI (dashed) vs Inclination

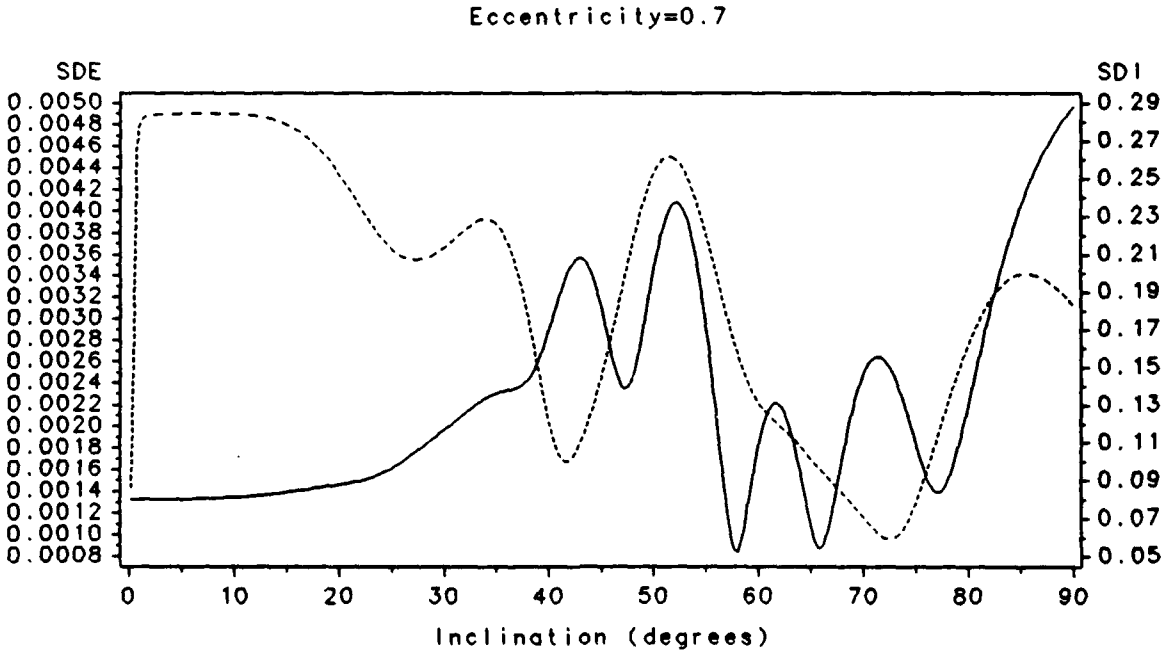

Figure 51. SDE and SDI (dashed) vs Inclination

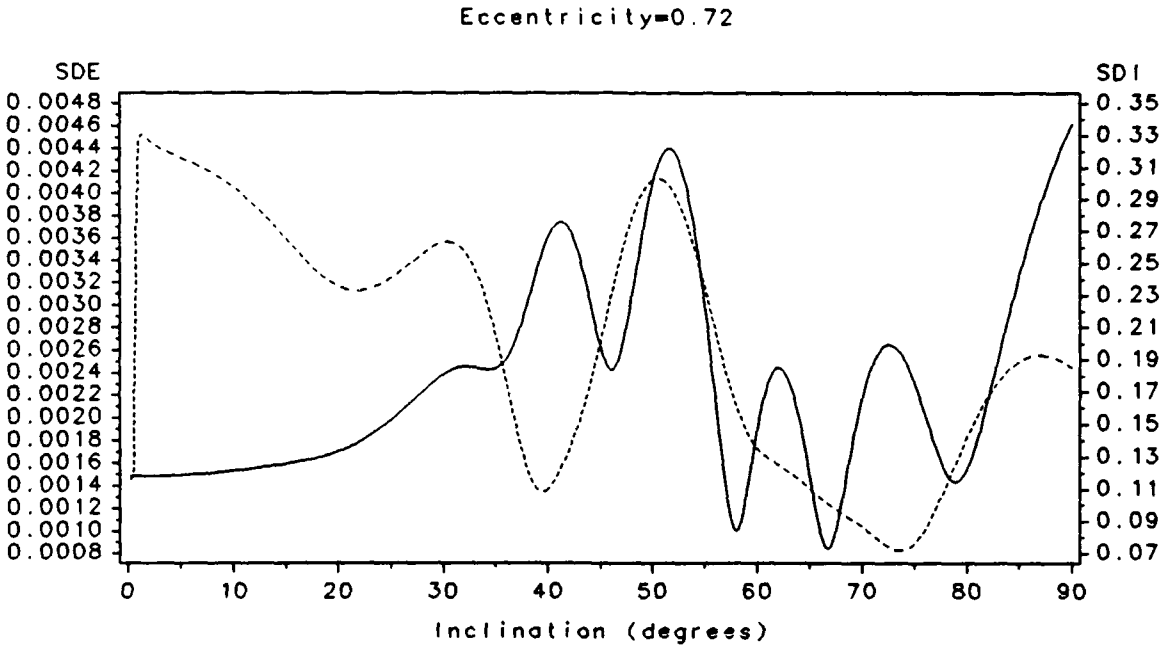

Figure 52. SDE and SDI (dashed) vs Inclination

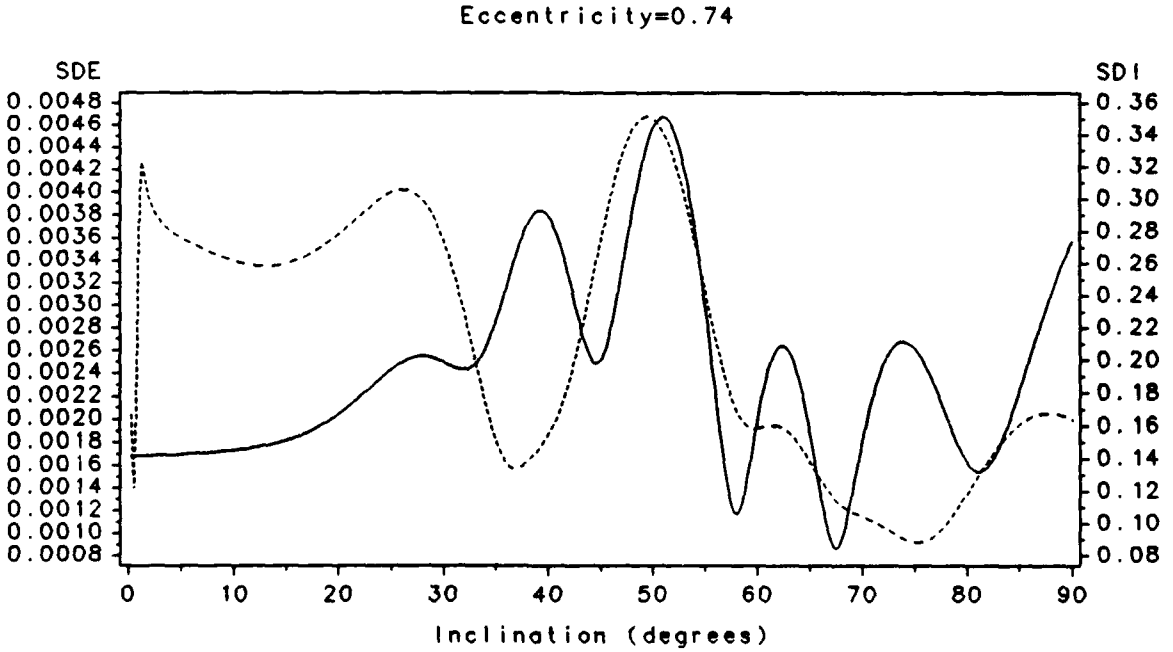

Figure 53. SDE and SDI (dashed) vs Inclination

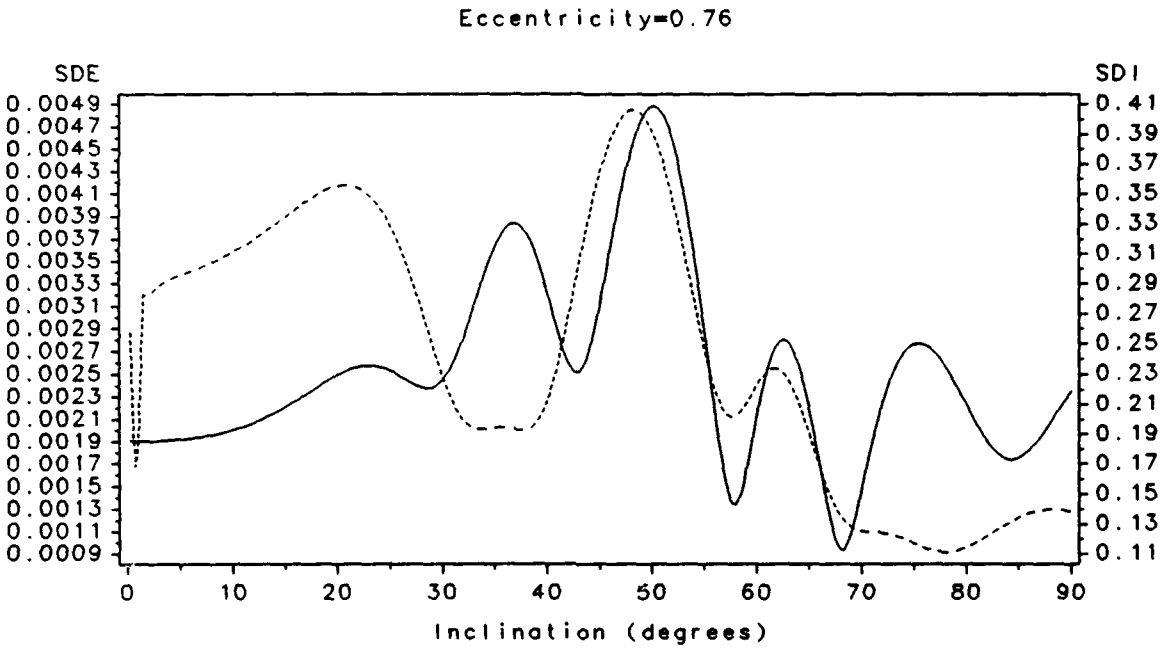

Figure 54. SDE and SDI (dashed) vs Inclination

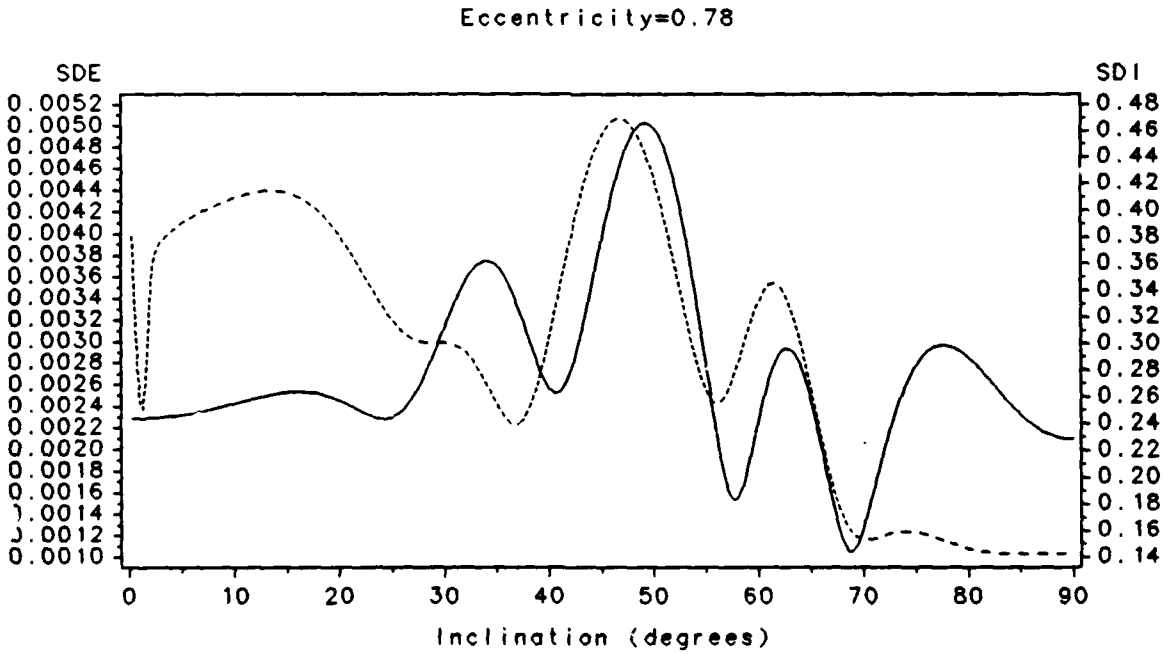

Figure 55. SDE and SDI (dashed) vs Inclination

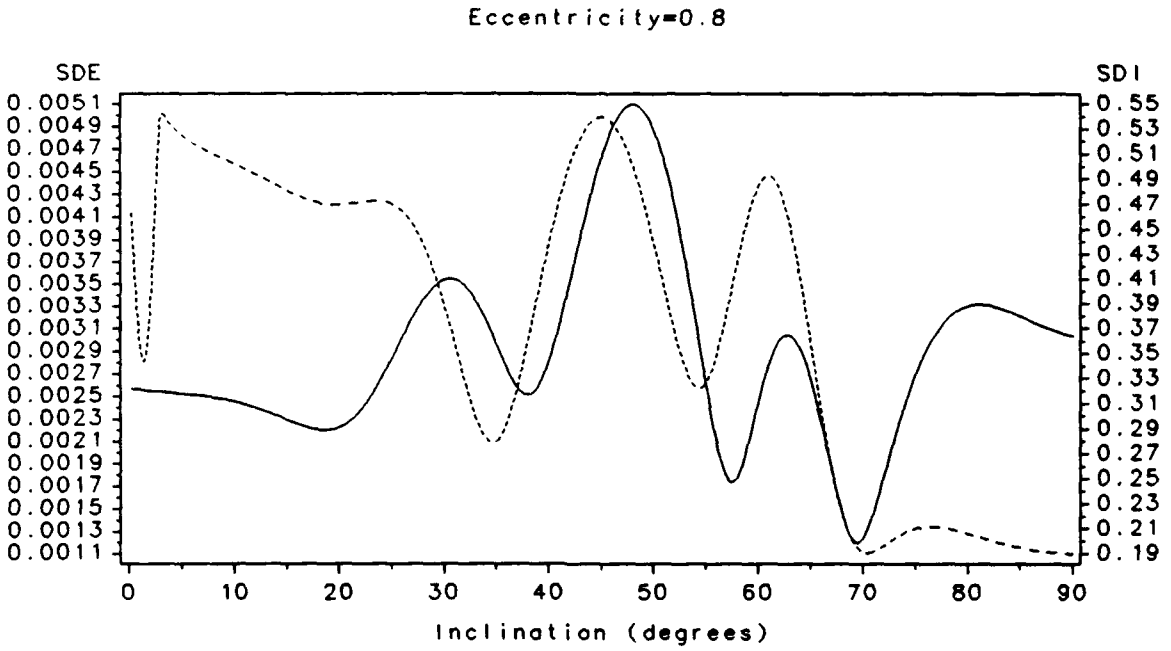

Figure 56. SDE and SDI (dashed) vs Inclination

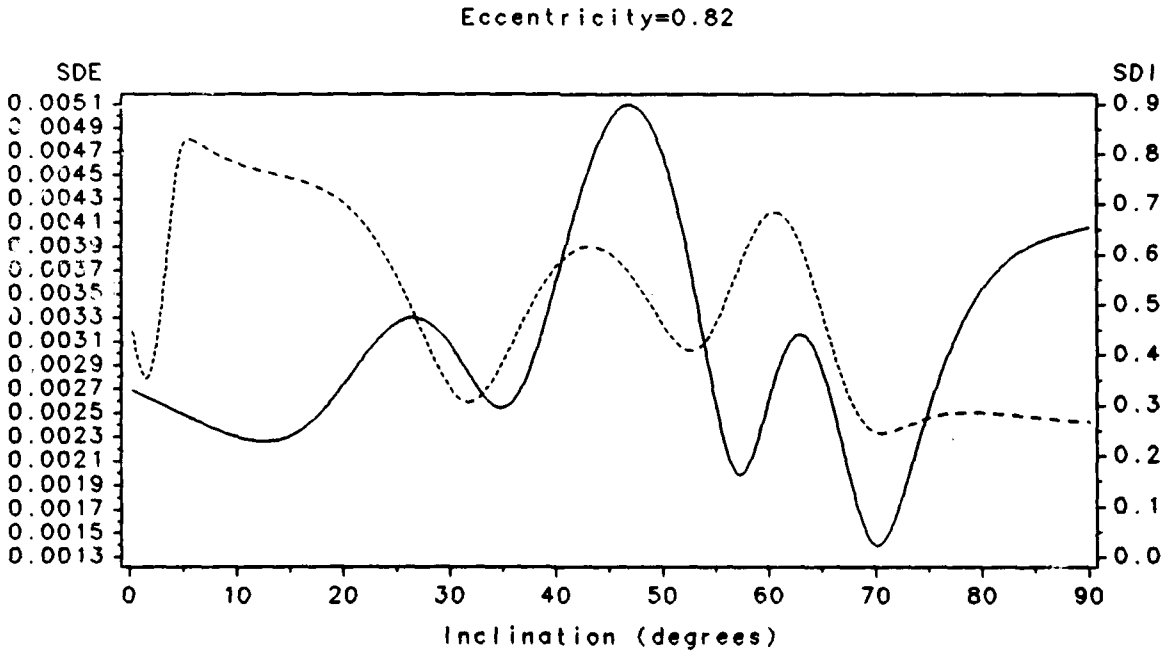

Figure 57. SDE and SDI (dashed) vs Inclination

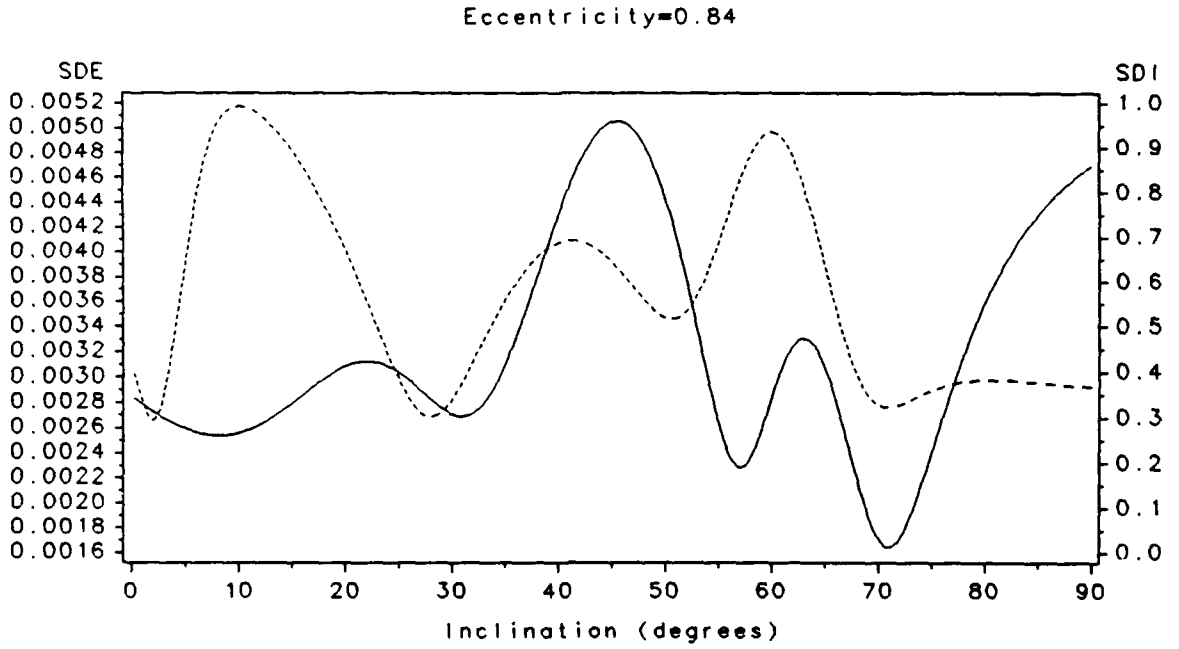

Figure 58. SDE and SDI (dashed) vs Inclination

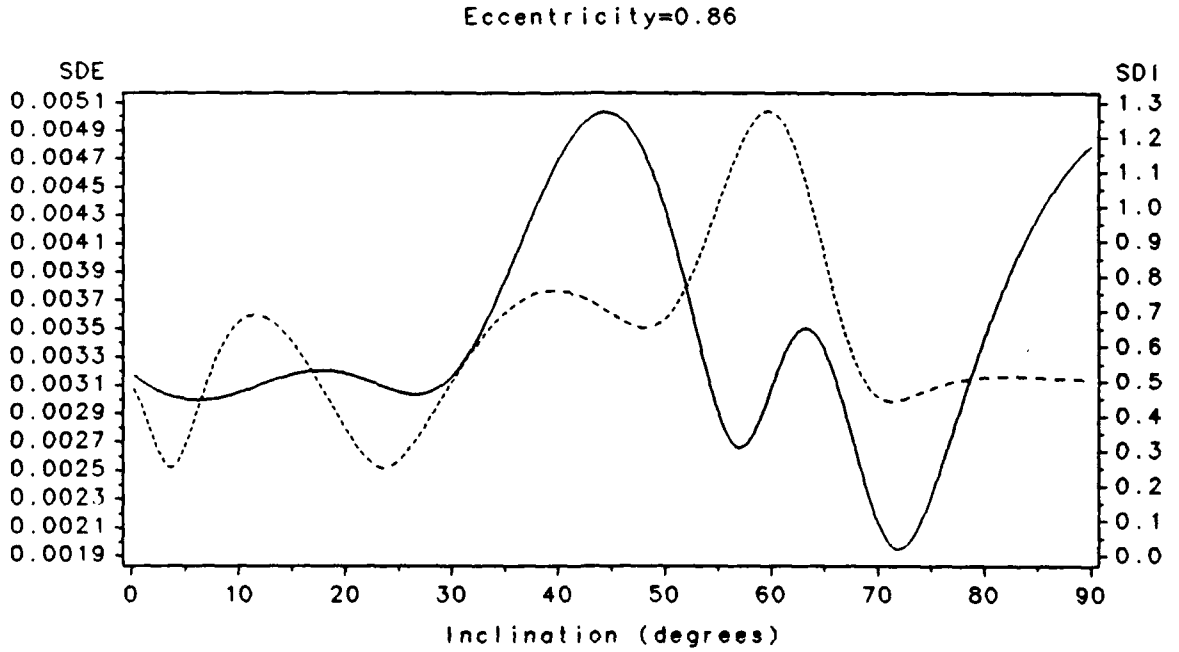

Figure 59. SDE and SDI (dashed) vs Inclination

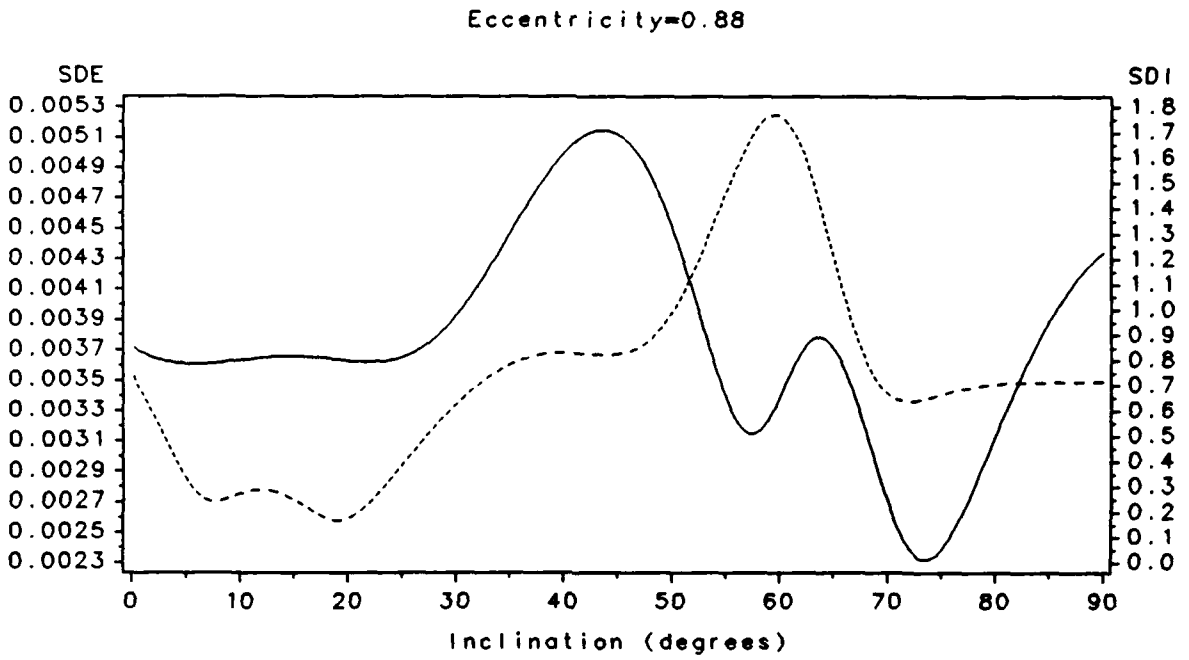

Figure 60. SDE and SDI (dashed) vs Inclination

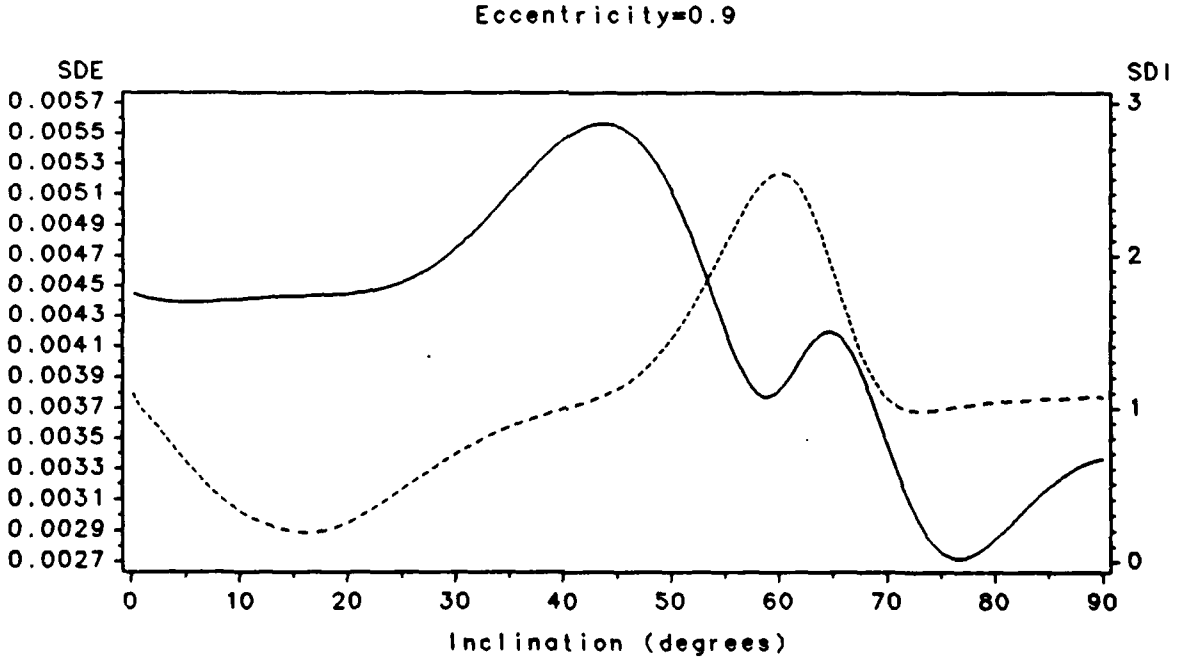

Figure 61. SDE and SDI (dashed) vs Inclination

Appendix E. *Tables for Critical Inclinations in Eccentricity*

Table 4. Critical Inclinations for Eccentricity: Curve a

	Radius of Periapse (km)					
	4500	5000	5500	6000	6500	7000
e	Critical Inclinations (degrees)					
0.40	-	-	-	67.75	68.00	68.25
0.42	-	-	67.50	68.00	68.00	68.50
0.44	-	-	67.50	67.75	68.25	68.75
0.46	-	-	67.75	67.75	68.25	69.25
0.48	-	-	67.75	68.00	68.50	70.00
0.50	-	67.50	67.75	68.25	68.75	71.75
0.52	-	67.50	67.75	68.25	69.25	74.00
0.54	-	67.75	68.00	68.50	70.25	75.75
0.56	-	68.00	68.25	68.75	72.00	77.50
0.58	67.50	67.75	68.25	69.25	74.25	79.50
0.60	67.50	67.75	68.50	70.25	76.25	81.75
0.62	67.75	68.00	68.75	72.50	78.25	85.25
0.64	68.00	68.25	69.25	75.00	80.50	-
0.66	67.75	68.50	70.50	77.00	83.75	-
0.68	68.00	68.75	73.25	79.50	-	-
0.70	68.25	69.50	75.75	82.50	-	-
0.72	68.50	71.25	78.25	-	-	-
0.74	68.75	74.50	81.50	-	-	-
0.76	69.75	77.25	87.50	-	-	-
0.78	73.00	80.75	-	-	-	-
0.80	76.50	87.75	-	-	-	-
0.82	80.50	-	-	-	-	-

Table 5. Critical Inclinations for Eccentricity: Curve b

	Radius of Periapse (km)					
	4500	5000	5500	6000	6500	7000
e	Critical Inclinations (degrees)					
0.40	-	-	-	-	65.00	64.75
0.42	-	-	-	-	65.00	64.75
0.44	-	-	-	-	64.75	64.50
0.46	-	-	-	-	64.75	64.50
0.48	-	-	-	65.00	64.75	64.75
0.50	-	-	-	65.00	64.50	64.75
0.52	-	-	64.75	64.75	64.50	65.00
0.54	-	-	65.00	64.75	64.75	65.75
0.56	-	-	65.00	64.75	64.75	66.50
0.58	-	-	64.75	64.75	65.25	67.50
0.60	-	-	64.75	64.75	65.75	68.75
0.62	-	65.00	64.75	65.00	66.75	69.75
0.64	-	65.00	64.75	65.50	68.00	70.75
0.66	64.50	64.75	64.75	66.25	69.50	71.75
0.68	65.00	64.75	65.00	67.50	70.50	73.00
0.70	65.00	64.75	65.75	69.00	71.75	74.00
0.72	64.75	65.00	66.75	70.25	72.75	75.50
0.74	64.75	65.25	68.50	71.50	74.00	77.25
0.76	64.75	66.25	70.00	72.75	75.75	79.50
0.78	65.25	68.00	71.50	74.25	77.75	84.25
0.80	66.00	70.00	73.00	76.25	81.50	-
0.82	67.75	71.50	74.75	79.25	-	-
0.84	70.00	73.50	77.75	-	-	-
0.86	72.00	76.25	84.50	-	-	-
0.88	74.75	82.50	-	-	-	-

Table 6. Critical Inclinations for Eccentricity: Curve c

	Radius of Periapse (km)					
	Critical Inclinations (degrees)					
e	4500	5000	5500	6000	6500	7000
0.52	-	-	-	-	-	60.25
0.54	-	-	-	-	-	60.25
0.56	-	-	-	-	-	60.50
0.58	-	-	-	-	-	60.50
0.60	-	-	-	-	-	60.75
0.62	-	-	-	-	60.50	61.25
0.64	-	-	-	-	60.75	61.50
0.66	-	-	-	60.50	61.25	62.00
0.68	-	-	-	60.75	61.50	62.25
0.70	-	-	-	61.00	62.00	62.50
0.72	-	-	60.75	61.50	62.25	62.50
0.74	-	-	61.25	62.00	62.50	62.50
0.76	-	-	61.75	62.50	62.75	62.75
0.78	-	61.25	62.25	63.00	63.00	62.75
0.80	-	62.00	63.00	63.25	63.00	62.75
0.82	62.00	62.75	63.50	63.50	63.25	62.75
0.84	63.00	64.00	63.75	63.75	63.25	62.75
0.86	64.00	64.75	64.25	64.00	63.50	63.00
0.88	65.00	65.00	65.00	64.50	64.00	63.50
0.90	-	-	-	65.25	65.00	64.75

Table 7. Critical Inclinations for Eccentricity: Curve d

	Radius of Periapse (km)					
	4500	5000	5500	6000	6500	7000
e	Critical Inclinations (degrees)					
0.52	-	-	-	-	-	55.00
0.54	-	-	-	-	-	54.75
0.56	-	-	-	-	-	54.50
0.58	-	-	-	-	55.00	54.00
0.60	-	-	-	-	54.75	53.50
0.62	-	-	-	-	54.25	53.00
0.64	-	-	-	55.00	53.75	52.75
0.66	-	-	-	54.75	53.50	52.25
0.68	-	-	-	54.25	53.00	51.50
0.70	-	-	55.00	53.75	52.50	51.00
0.72	-	-	54.50	53.25	51.75	50.25
0.74	-	55.25	54.00	52.75	51.25	49.25
0.76	-	55.00	53.50	52.25	50.50	48.25
0.78	-	54.50	53.25	51.50	49.50	47.00
0.80	55.25	54.00	52.50	50.75	48.25	45.50
0.82	55.00	53.50	52.00	49.75	47.00	44.25
0.84	54.50	53.25	51.25	48.75	45.75	42.75
0.86	54.25	52.75	50.50	47.75	44.75	41.50
0.88	54.25	52.50	49.75	46.75	43.75	40.75
0.90	-	-	-	46.75	44.00	41.00

Table 8. Critical Inclinations for Eccentricity: Curve e

	Radius of Periapse (km)					
	4500	5000	5500	6000	6500	7000
e	Critical Inclinations (degrees)					
0.40	-	54.75	-	53.75	52.25	52.00
0.42	-	54.75	-	53.50	52.25	51.50
0.44	-	54.50	-	53.00	52.25	51.25
0.46	-	54.50	54.00	52.50	52.00	50.75
0.48	-	54.25	53.75	52.25	51.75	50.25
0.50	54.75	-	53.25	52.25	51.25	49.50
0.52	54.50	-	52.75	52.00	50.75	49.25
0.54	54.50	54.00	52.25	51.75	50.00	49.25
0.56	54.25	53.75	52.25	51.25	49.50	48.75
0.58	-	53.25	52.25	50.75	49.25	47.75
0.60	-	52.50	51.75	50.00	49.25	46.75
0.62	53.75	52.25	51.25	49.50	48.50	45.50
0.64	53.50	52.25	50.75	49.50	47.25	44.25
0.66	52.75	52.00	50.00	49.00	46.00	42.75
0.68	52.25	51.25	49.50	48.00	44.75	41.25
0.70	52.25	50.75	49.75	46.75	43.25	39.25
0.72	52.00	50.00	48.50	45.25	41.50	37.25
0.74	51.25	49.75	47.25	43.50	39.50	34.75
0.76	50.50	49.25	45.75	41.75	37.25	31.75
0.78	49.75	47.75	44.00	39.50	34.25	28.25
0.80	49.75	46.00	41.75	36.75	30.75	24.50
0.82	48.25	44.00	39.25	33.50	26.75	20.50
0.84	46.25	41.50	36.00	29.25	22.25	16.75
0.86	43.75	38.25	31.75	24.50	18.00	14.25
0.88	40.75	34.25	26.50	19.50	15.00	-
0.90	-	-	-	16.00	-	-

Table 9. Critical Inclinations for Eccentricity: Curve f

	Radius of Periapse (km)					
	4500	5000	5500	6000	6500	7000
e	Critical Inclinations (degrees)					
0.40	-	60.25	60.25	60.25	60.25	60.25
0.42	-	60.25	60.25	60.50	60.25	60.00
0.44	-	60.25	60.25	60.25	60.25	59.75
0.46	-	60.25	60.25	60.25	60.25	59.25
0.48	-	60.25	60.25	60.25	60.25	58.75
0.50	60.25	60.25	60.50	60.25	60.00	-
0.52	60.25	60.25	60.25	60.25	59.50	-
0.54	60.25	60.25	60.25	60.25	58.75	-
0.56	60.25	60.50	60.25	60.00	-	-
0.58	60.25	60.50	60.50	59.50	-	-
0.60	60.25	60.50	60.25	59.00	-	-
0.62	60.50	60.50	60.25	-	-	-
0.64	60.50	60.50	59.75	-	-	-
0.66	60.50	60.50	59.00	-	-	-
0.68	60.50	60.25	-	-	-	-
0.70	60.50	60.00	-	-	-	-
0.72	60.50	59.25	-	-	-	-
0.74	60.50	-	-	-	-	-
0.76	60.00	-	-	-	-	-
0.78	59.25	-	-	-	-	-

Bibliography

1. Andrews, Larry C., *Special Functions for Engineers and Applied Mathematicians.* New York: Macmillan Publishing Company, 1985.
2. Bain, Rodney D., Lecture material from Advanced Astrodynamics II, School of Engineering, Air Force Institute of Technology (AU), Wright-Patterson AFB OH, July 1988.
3. Bate, Mueller, and White, *Fundamentals of Astrodynamics.* New York: Dover Publications, Inc., 1971.
4. Battin, Richard H., *An Introduction to the Mathematics and Methods of Astrodynamics.* AIAA Education Series, 1987.
5. Breakwell, J. V. and R. D. Hensley, "An Investigation of High Eccentricity Orbits About Mars," *Trajectory Analysis and Guidance Theory.* NASA Cambridge: Electronics Research Center, 1966.
6. Brouwer, Dirk, "Solution of the Problem of Artificial Satellite Theory Without Drag," *The Astronomical Journal, 64:* 378-397, 1959.
7. Garfinkel, Boris, "Formal Solution in the Problem of Small Divisors," *The Astronomical Journal, 71:* 657-786.
8. ——, "On the Motion of a Satellite in the Vicinity of the Critical Inclination," *The Astronomical Journal, 65:* 624-627, 1960.
9. Gedeon, G. S., "Tesseral Resonance Effects on Satellite Orbits," *Celestial Mechanics, 1:* 167-189, 1969.
10. Goldstein, Herbert, *Classical Mechanics.* Addison-Wesley, 1965.
11. Kaufman, Bernard, "Variation of Parameters and the Long-term Behavior of Planetary Orbiters," AIAA Paper No. 70-1055, AAS/AIAA Astrodynamics Conference, Santa Barbara, CA, August 19-21, 1970.
12. Kwok, J. H., "The Long Term Orbit Predictor," Jet Propulsion Laboratory, Technical Report No. 86-151, June 1986.
13. Neter, John and others, *Applied Linear Statistical Models* (Second Edition). Homewood, Illinois: Irwin, 1985.
14. *SAS User's Guide* (1979 Edition). Raleigh, N.C.: SAS Institute, 1979.
15. Shampine, L. F., and M. K. Gordon, *Computer Solution of Ordinary Differential Equations*, W. H. Freeman and Company, 1975.

Vita

Captain Denis F. Durand [redacted]

He [redacted] Rensselaer Polytechnic Institute. He left college after the first year and enlisted in the United Sates Air Force in June 1977. In the same year he married Margaret F. Brophy. Their son, Devon, was born on 7 September 1979 at RAF Lakenheath, England. While serving at RAF Lakenheath, Denis was accepted into the Airman Education and Commissioning Program (AECP), and in 1981 he attended the University of Arizona. In May 1984 he received the degree of Bachelor of Science in Aerospace Engineering, and went on to recieve a commission at Officers Training School. Beginning in September 1984 he served as a guidance system analyst at the Foreign Technology Division, Wright-Patterson AFB, OH, until entering the School of Engineering, Air Force Institute of Technology, in June 1988.

[redacted]

UNCLASSIFIED
SECURITY CLASSIFICATION OF THIS PAGE

REPORT DOCUMENTATION PAGE

Form Approved
OMB No. 0704-0188

1a. REPORT SECURITY CLASSIFICATION UNCLASSIFIED	1b. RESTRICTIVE MARKINGS
2a. SECURITY CLASSIFICATION AUTHORITY	3. DISTRIBUTION / AVAILABILITY OF REPORT Approved for public release; distribution unlimited
2b. DECLASSIFICATION / DOWNGRADING SCHEDULE	
4. PERFORMING ORGANIZATION REPORT NUMBER(S) AFIT/GA/ENY/89J-2	5. MONITORING ORGANIZATION REPORT NUMBER(S)
6a. NAME OF PERFORMING ORGANIZATION School of Engineering 6b. OFFICE SYMBOL (If applicable) AFIT/ENY	7a. NAME OF MONITORING ORGANIZATION
6c. ADDRESS (City, State, and ZIP Code) Air Force Institute of Technology (AU) Wright-Patterson AFB, Ohio 45433-6583	7b. ADDRESS (City, State, and ZIP Code)
8a. NAME OF FUNDING / SPONSORING ORGANIZATION 8b. OFFICE SYMBOL (If applicable)	9. PROCUREMENT INSTRUMENT IDENTIFICATION NUMBER
8c. ADDRESS (City, State, and ZIP Code)	10. SOURCE OF FUNDING NUMBERS PROGRAM ELEMENT NO. / PROJECT NO. / TASK NO / WORK UNIT ACCESSION NO.

11. TITLE (Include Security Classification)
NUMERICAL DETERMINATION OF THE LOCATION OF CRITICAL INCLINATIONS FOR LONG TERM HIGH ECCENTRICITY ORBITS ABOUT MARS

12. PERSONAL AUTHOR(S)
Denis F. Durand, B. S., Capt, USAF

13a. TYPE OF REPORT	13b. TIME COVERED	14. DATE OF REPORT (Year, Month, Day)	15. PAGE COUNT
MS Thesis	FROM _____ TO _____	1989 June	107

16. SUPPLEMENTARY NOTATION

17. COSATI CODES			18. SUBJECT TERMS (Continue on reverse if necessary and identify by block number)
FIELD	GROUP	SUB-GROUP	Orbits High Orbit Trajectories
22	01		

19. ABSTRACT (Continue on reverse if necessary and identify by block number)

Thesis Advisor: Capt R. D. Bain
Assistant Professor of Astronautics
Department of Aeronautics and Astronautics

20. DISTRIBUTION / AVAILABILITY OF ABSTRACT ☒ UNCLASSIFIED/UNLIMITED ☐ SAME AS RPT. ☐ DTIC USERS	21. ABSTRACT SECURITY CLASSIFICATION UNCLASSIFIED
22a. NAME OF RESPONSIBLE INDIVIDUAL R. D. Bain, Assistant Professor	22b. TELEPHONE (Include Area Code) (513)255-3633 22c. OFFICE SYMBOL ENY

DD Form 1473, JUN 86 *Previous editions are obsolete.*

SECURITY CLASSIFICATION OF THIS PAGE
UNCLASSIFIED

The purpose of this study is to locate critical inclinations in long term high eccentricity orbits about Mars using numerical methods. A critical inclination is defined as the inclination at orbit insertion which produces a local maximum in the amplitude of the variation of eccentricity or inclination. The perturbation model consists of the first non-zero zonal harmonic of the Mars gravity potential and the Sun as a point mass third body. The search range consists of inclinations from 0.25 to 90.0 degrees, eccentricities from 0.40 to 0.90, periapse radii from 4000 km to 7000 km, and orbit lifetimes of 10 Earth years.

The numerical search comprises the following procedure: (1) A time history of eccentricity and inclination is produced for each combination of orbit insertion initial conditions by numerically propagating Lagrange's Planetary Equations. (2) Each time history is fit, in the least squares sense, to a linear function. The standard deviation of the residuals for each fit is employed as the search parameter. (3) A three-dimensional surface plot of the standard deviation in eccentricity and the standard deviation in inclination versus eccentricity and inclination is produced for each value of periapse radius considered. The local maximums in these surfaces identifies the locations of the critical inclinations. (4) The three-dimensional surfaces are then reduced to two dimensions by plotting inclination versus eccentricity for the local maximums in standard deviation.

Six critical inclination curves for eccentricity are identified, three of which are curve fit and found to be linear in periapse radius and quadratic in eccentricity. The surface plots for inclination indicate the presence of large variations but the surface topography does not allow for the identification of distinct local maximum curves.